UNIVERSIDAD DE CHILE
FACULTAD DE CIENCIAS FÍSICAS Y MATEMÁTICAS
DEPARTAMENTO DE INGENIERIA ÉLECTRICA

DESIGN AND IMPLEMENTATION OF A FREQUENCY DIVISION MULTIPLEXER (FDM) CIRCUIT BOARD FOR THE CANADIAN-CHILEAN ARRAY FOR RADIO TRANSIENT STUDIES (CHARTS) PROJECT

TESIS PARA OPTAR AL GRADO DE
MAGÍSTER EN CIENCIAS DE LA INGENIERÍA, MENCIÓN ELÉCTRICA
MEMORIA PARA OPTAR AL TÍTULO DE INGENIERO CIVIL ELÉCTRICO

SEBASTIÁN ANTONIO MANOSALVA ESCOBAR

PROFESOR GUÍA:
TOMÁS CASSANELLI ESPEJO

MIEMBROS DE LA COMISIÓN:
JUAN MENA PARRA
RICARDO FINGER CAMUS

Este trabajo ha sido parcialmente financiado por QUIMAL de ANID, ANID BASAL FB210003, University of Toronto y MITACS

SANTIAGO DE CHILE
2025

RESUMEN DE LA TESIS PARA OPTAR
AL GRADO DE MAGÍSTER EN CIENCIAS
DE LA INGENIERÍA, MENCIÓN ELÉCTRICA
Y MEMORIA PARA OPTAR AL TÍTULO DE
INGENIERO CIVIL ELÉCTRICO
POR: SEBASTIÁN ANTONIO MANOSALVA ESCOBAR
FECHA: 2025
PROF. GUÍA: TOMÁS CASSANELLI ESPEJO

DISEÑO E IMPLEMENTACIÓN DE UNA PLACA DE MULTIPLEXIÓN POR DIVISIÓN DE FRECUENCIAS (FDM) PARA EL PROYECTO CANADIAN-CHILEAN ARRAY FOR RADIO TRANSIENT STUDIES (CHARTS)

La multiplexión por división de frecuencias (FDM) es una técnica clásica de telecomunicaciones, que puede aplicarse en radioastronomía para aprovechar el ancho de banda de digitalizadores modernos. En este trabajo, se utiliza FDM para combinar señales de ocho antenas independientes en el rango de 300–500 MHz, generando una salida entre 300–2366 MHz. Esta será digitalizada por tecnologías Xilinx RFSoC, con hasta 2.5 GHz de ancho de banda.

El objetivo de este trabajo es diseñar y fabricar una placa FDM para el proyecto Canadian-Chilean array for radio transient studies (CHARTS), que busca detectar ráfagas rápidas de radio (FRBs) con un arreglo de 256 antenas. La placa FDM reduce el número de digitalizadores requeridos, minimiza perdidas y mantiene la calidad de la señal, para detectar FRBs.

Se desarrollaron prototipos y simulaciones de la placa FDM, según el tipo de antena usado en CHARTS. El diseño final cuenta con tecnología diferencial para la multiplexión. Se midieron la respuesta en frecuencia y el acople entre señales, mostrando que la placa FDM es capaz de separar correctamente las señales en los rangos de frecuencia establecidos. Finalmente, se discuten mejoras una nueva versión de la FDM.

RESUMEN DE LA TESIS PARA OPTAR
AL GRADO DE MAGÍSTER EN CIENCIAS
DE LA INGENIERÍA, MENCIÓN ELÉCTRICA
Y MEMORIA PARA OPTAR AL TÍTULO DE
INGENIERO CIVIL ELÉCTRICO
POR: SEBASTIÁN ANTONIO MANOSALVA ESCOBAR
FECHA: 2025
PROF. GUÍA: TOMÁS CASSANELLI ESPEJO

DESIGN AND IMPLEMENTATION OF A FREQUENCY DIVISION MULTIPLEXER (FDM) CIRCUIT BOARD FOR THE CANADIAN-CHILEAN ARRAY FOR RADIO TRANSIENT STUDIES (CHARTS) PROJECT

Frequency division multiplexing (FDM) is a telecommunications technique utilized in this work to take advantage of the bandwidth of modern digitizers in radio astronomy receivers. It is employed to receive signals from eight independent antennas, each with a bandwidth of 200 MHz and operating between 300–500 MHz. These signals are frequency multiplexed and combined into a single output spanning from 300 to 2366 MHz, ready for digitization using Xilinx's RFSoC technology, which offers a bandwidth of 2.5 GHz.

This project focuses on the design and manufacture of an FDM board for the Canadian-Chilean Array for Radio Transient Studies (CHARTS), aimed at detecting fast radio bursts (FRBs) with a 256-antenna array. The FDM board significantly reduces the number of required digitizers while minimizing noise temperature and preserving signal quality for FRB detection.

Various prototypes and simulations were conducted based on the proposed antennas for CHARTS. The final FDM board design employs differential technology for signal multiplexing. Measurements indicated successful separation of signals from the eight antennas. Recommendations for design improvements for the next version of the FDM board were also discussed in this work.

A quien este leyendo esto, que tenga un buen día.

Acknowledgments

I want to thank my family first, who supported me every single day throughout this long process. To my parents, Gisela and René, thank you for teaching me the foundations of who I am and giving me the opportunity to study what I am passionate about. To my brother Alonso for always being on the same wavelength with our crazy ideas and, more than anything, for having fun together. And, of course, to my cat, simply for being there and helping me destress.

Thank you to my friends from the University of Chile, who made the academic years enjoyable and entertaining, especially during the lunch breaks. I hope we keep meeting up, whether it's for online games, a good barbecue, or just to reminisce about the old days.

To my friends from AstroLab and the millimeter wave lab, I am very grateful to have met so many amazing people who share my interests for the serious discussions where I learned so much and grew as a professional and, of course, for the not-so-serious moments too. There is never a boring time with you all.

To my colleagues at the University of Toronto, thank you for welcoming me during my short stay on campus. The environment was fantastic and allowed me to meet many brilliant people and broaden my horizons. I learned a lot from you, and I am truly grateful.

Thank you to my supervisor, Tomás Cassanelli, for always dreaming big, something that finally materialized into this project. As a fresh electrical engineer interested in astronomical instrumentation, building a telescope is one of my dreams, and thanks to this thesis, I had the incredible opportunity to do just that.

The CHARTS project is supported by the Dunlap Seed Funding program and the ANID QUIMAL fund. T.C. and S.M. gratefully acknowledge support by the ANID BASAL FB210003 and fondo de astronomía: ANID / Fondo 2023 QUIMAL / QUIMAL230001. The Dunlap Institute is funded through an endowment established by the David Dunlap family and the University of Toronto.

Table of Content

List of Tables

List of Figures

Acronyms

1dB 1dB compression point.

ADC analog-to-digital converter.

CASPER collaboration for astronomy signal processing and electronics research.
CHARTS Canadian-Chilean Array for Radio Transient Studies.
CHIME Canadian Hydrogen Intensity Mapping Experiment.
CPW coplanar waveguides.

DAC digital-to-analog converter.
DC direct current.
DM dispersion measure.

FAST Five-hundred-meter Aperture Spherical Telescope.
FDM frequency division multiplexing.
FFT fast Fourier transform.
FPGA field programmable gate array.
FRB fast radio burst.

GCPW grounded coplanar waveguide.

IF intermediate frequency.
IGM intergalactic medium.
ISI inter-symbol-interference.
ISM interstellar medium.

LNA low-noise amplifier.
LO local oscillator.
LSB lower side band.
LWLab Long Wavelength Laboratory.

MOST Molonglo Observatory Synthesis Telescope.
MWL Millimeter Wave Lab Laboratory.

NF noise figure.

OFDM Orthogonal Frequency Division Multiplexing.

PCB printed circuit board.

RF radio frequency.

RFI radio frequency interference.
RFSoC radio frequency system-on-chip.
rms root mean square.

SMA SubMiniature version A.
SMT surface mounted technology.
SNR signal-to-noise ratio.

TEM transverse electromagnetic.
TOIP third-order intercept point.

UofT University of Toronto.
USB upper side band.
UTRAINLab University of Toronto Radio Astronomy and InstrumentatioN Lab.

VNA vector network analyzer.
VSS Visual System Simulator.

Chapter 1

Introduction

1.1 Motivation

The discovery of radio pulsars in 1967 was a groundbreaking moment in astronomy, confirming the existence of neutron stars and providing a powerful tool to study them. Radio pulsar studies have allowed us to explore and probe the nature of strong gravity, dense matter, and the interstellar medium (Lorimer & Kramer 2005). Until 2007, all detected radio pulsars had Galactic origins. However, during a pulsar survey that year, the first fast radio burst (FRB) was observed by Lorimer et al. (Petroff et al. 2019).

FRBs are extragalactic transients characterized by short-duration pulses ranging from 1 µs to 100 ms, similar to individual pulses from pulsars but ten orders of magnitude more energetic ($\sim 10^{40}$ erg). The other differences to Galactic pulsars are their large dispersion measures (DMs) that suggests an extragalactic origin and all-sky rates of approximately 10^3 per day. This indicates that these phenomena are observable from any location on Earth at all times.

Since their initial discovery, around 600 FRBs have been detected (CHIME/FRB Collaboration et al. 2021). Despite the large number of observations, their astrophysical mechanisms (one or multiple) remain unknown. One of the main challenges toward understanding FRBs lies in the difficulty of determining their precise on-sky positions, which is critical to localizing their host galaxies (Cassanelli et al. 2022). Multiple telescopes have detected FRBs, like the Canadian Hydrogen Intensity Mapping Experiment (CHIME) (Collaboration 2023a), Five-hundred-meter Aperture Spherical Telescope (FAST) in China (Collaboration 2023c), Molonglo Observatory Synthesis Telescope (MOST) in Australia (Collaboration 2023d), etc. However, none can localize FRBs at detection (although CHIME/FRB outriggers will be on sky soon: Lanman et al. (2024)), and few are observing at southern declinations, so we are losing a portion of the detections, see fig. 1.1. For this reason, building radio telescopes dedicated to transients in the southern hemisphere is essential to cover a more significant portion of the sky and provide complete exposure of transient phenomena.

CHARTS will open a new window to study FRBs as one of the few radio telescopes fully dedicated to FRB detection in the southern hemisphere. CHARTS innovative design

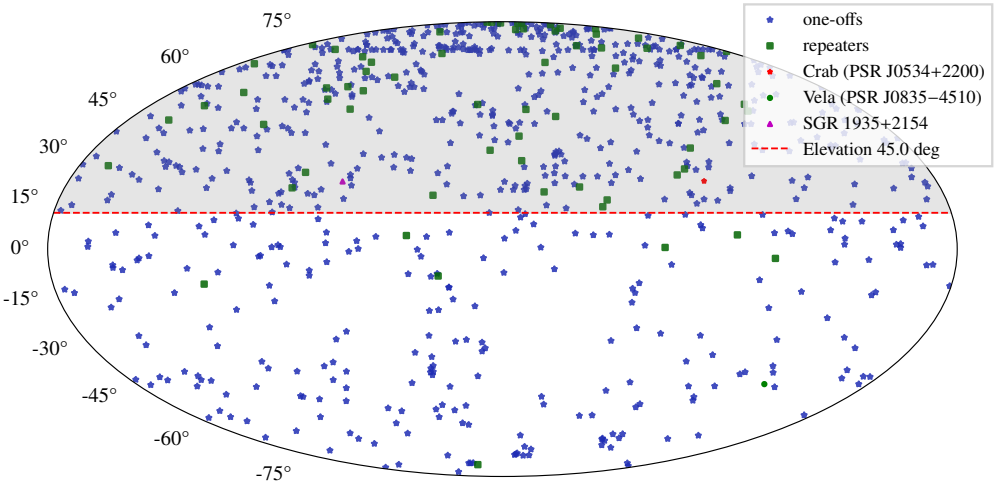

Figure 1.1: Distribution of detected FRBs towards the globe (one-off and repeaters), including detections of the Crab pulsar, the Vela pulsar, and the magnetar SGR 1935+2154. Most of the FRBs have been detected above 0 deg by CHIME. CHARTS visibility will cover the sky below the red line limit, increasing the number of detections in the southern hemisphere.

is based on a frequency division multiplexing (FDM) board. This component will allow CHARTS to reduce the number of digitizers and use their full sampling rates. Decreasing the number of digitizers will lower the project's overall cost, and the modular design of the FDM will help CHARTS scalability. In this thesis, I will center the discussion on the design and characterization of the FDM board, more specifically, two FDM designs: the single-ended prototype made for 50 Ω antennas and the differential input FDM made for differential antennas. Both boards were fabricated, with developments culminating in the differential design. Nevertheless, these two FDMs could be used within CHARTS or future radio arrays, depending on the antenna type and configuration.

1.2 Hypothesis

The FDM board will be able to multiplex the signals of eight CHARTS antennas, reducing both the losses in the printed circuit board and the coupling among signals within it. Properly separating the eight antennas in frequency reduces the number of digitizers required in the postprocessing stages (FX-engine), thus minimizing the number of field programmable gate arrays (FPGAs) used in the radio telescope, and making more efficient use of the digitized bandwidth.

1.3 Objectives

1.3.1 General objective

The main objective of this study was to design, simulate, build, and characterize the frequency division multiplexing board for the CHARTS array.

1.3.2 Specific objectives

Multiple commercial and in-house components were used and tested in different FDM designs, and all of those components were also characterized. The specific objectives are related to the study of the different FDM components and options used during this thesis. These objectives are:

- Design testing boards of all commercial components and compare them with their specs and simulations.
- Characterize all the commercial and in-house components of the FDM board.
- Design custom filters for the FDM board.
- Design, fabricate, and test different FDM prototypes.
- Test the FDM board with a laboratory setup.
- Design and compare two FDM designs: single input and differential input, based on different antennas.

The final FDM should follow restrictions and conditions to be used in the CHARTS array. These conditions were also part of the thesis objectives, and they are:

- Coupling between chains $< -20\,\mathrm{dB}$.
- Maximum losses $< 31.12\,\mathrm{dB}$.
- Isolation between RF,IF, and LO ports $> 20\,\mathrm{dB}$.
- Having a flat response in the desired frequency range of the chain.

1.4 Thesis outline

This thesis began with a general view of the FRBs radio transient astronomical events, followed by an introduction to CHARTS, the relevance of the FDM, and the objectives of this thesis. The following chapters are:

1. Chapter 2: **Theoretical Framework** This chapter summarizes the theoretical concepts used in the thesis. It includes the theory of FRBs, the theory of the FDM, and relevant concepts of RF circuits and components used in the FDM. There is also an explanation of CHARTS specifications and structure.

2. Chapter 3: **Design and characterization of FDM components** The description of the overall FDM structure is explained in this chapter. It explains the FDM restrictions, selection of components, methodology to test the components, and their results compared with the expected values.

3. Chapter 4: **Single input FDM design and validation** This chapter describes the simulations, testing methodology, and results of the single-ended FDM and the differential FDM board. An analysis of the behaviour of the board and possible upgrades is also explored.

4. Chapter 5: **Conclusions** This chapter summarizes the results of the thesis, and the future work that can be done with the FDM board.

Chapter 2

Theoretical Framework

In this chapter, the theoretical background necessary to understand the various sections of this thesis is given. First, I introduce the principal concepts of the thesis motivation, FRBs. Then, I provide information about the fundamental concepts of radio frequency circuits and receivers, like scattering matrix, impedance matching, transmission line theory, radio noise, radio receivers, and their components. Finally, a review of CHARTS, the FDM and the RFSoC technologies.

2.1 Fast radio burst

FRBs are bright pulses of short duration of a few milliseconds. They have a broad frequency range that has been observed from 110 MHz (Pleunis et al. 2021) up to 8 GHz (Bethapudi et al. 2023). Similarly to known Galactic pulsars, FRBs exhibit frequency-dependent arrival time delays caused by dispersion in the intervening medium ($\propto \nu^{-2}$). However, unlike pulsar emission, FRB pulses show much more significant dispersive delays, consistent with an extragalactic origin (Petroff et al. 2022). Another difference from pulsars is that FRB pulses have higher flux densities than Galactic pulsars, ranging from 50 mJy to 100 Jy.

Despite the large number of FRBs detected, their origin remains unknown. Observations have revealed two main categories: repeating and non-repeating FRBs (see fig. 1.1). Repeating sources produce multiple bursts over time, while non-repeaters (one-offs) have only been observed as single events, suggesting potential differences in their underlying astrophysical mechanisms.

In 2020, a bright radio burst was detected from the Galactic magnetar SGR 1935+2154 (Andersen et al. 2020). This detection supports the hypothesis that (at least a population of) FRBs are emitted by magnetars. Nevertheless, the magnetar emission was several orders of magnitude less energetic than that of a typical FRB (10^{34} erg compared with $\sim 10^{40}$ erg). Proposed explanations for the origin and mechanisms of FRBs include highly magnetized neutron stars (magnetars), synchrotron maser emission, and a potential link to dark matter (lensing effects). While none of these explanations has been fully confirmed, recent detections

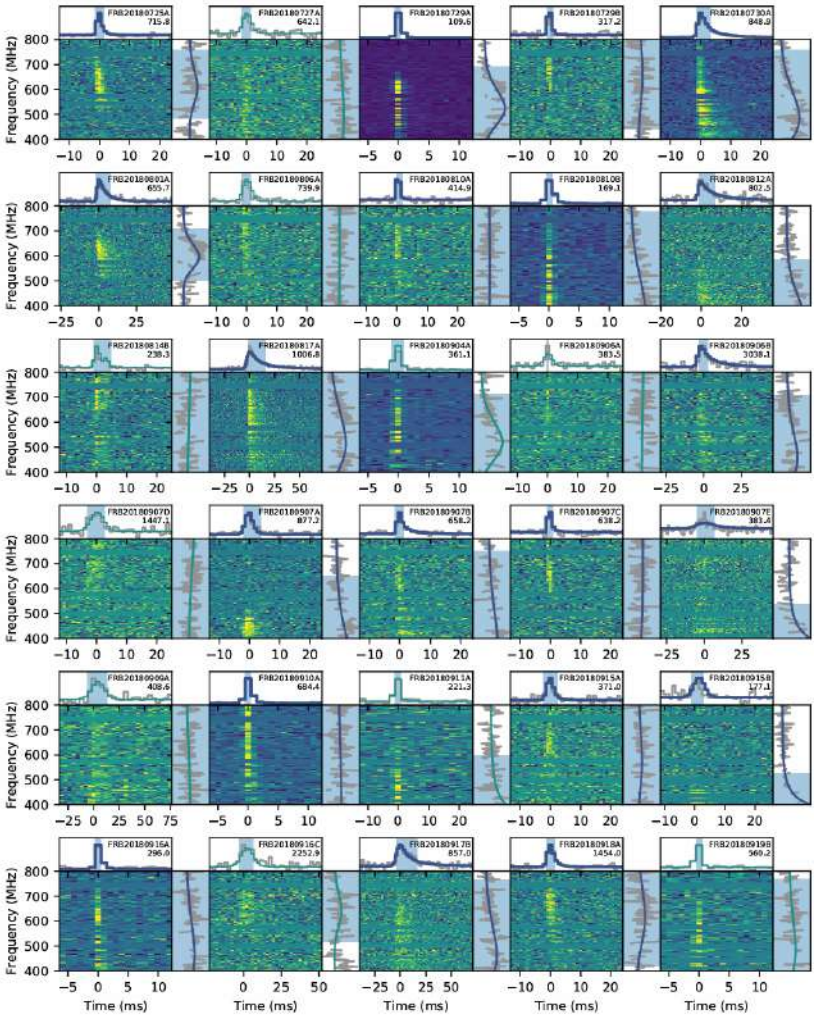

Figure 2.1: Intensity or "waterfall plots" of non-repeater (one-off) FRBs in CHIME/FRB catalog. The name of the FRB and the best fit DM in units of $\mathrm{pc\,cm^{-3}}$ are in the top right corner of each panel. The blue shaded regions in the time series and spectra indicate the burst durations and emission bandwidths, respectively. Figure extracted from (CHIME/FRB Collaboration et al. 2021)

of repeating and non-repeating FRBs suggest multiple mechanisms might be at play due to their distinct structures. In fig. 2.1, we can see some examples of one-off FRBs.

2.1.1 Propagation effects of FRBs

As signals from pulsars and FRBs propagates through the interstellar medium (ISM) or, in the case of FRBs, also the intergalactic medium (IGM). All of them undergo three distinct propagation effects: dispersion, scintillation, and scattering. While the pulse propagates in the IGM, it passes through ionized components in the medium. These media produce a delay in pulse arrival time that is inversely proportional to the observing frequency. The constant of proportionality is known as the DM. This effect can be observed in fig. 2.2, where lower frequencies experience a greater dispersion delay than higher frequencies. This dispersion

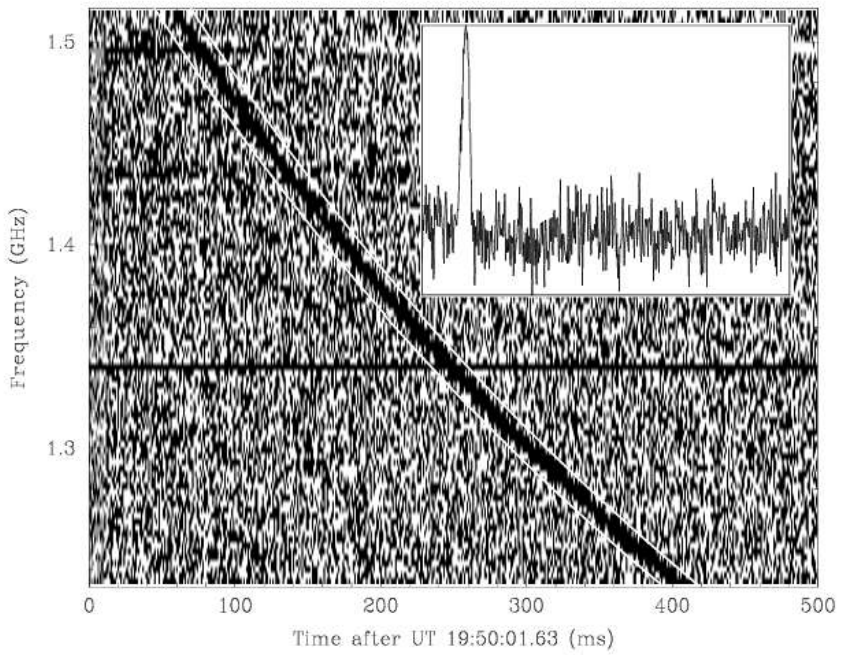

Figure 2.2: First FRB detected by Lorimer et al. The typical frequency dependence of the dispersion delay can be observed as the FRB arrives first in the higher frequencies. Image extracted from (Lorimer et al. 2007).

delay is given by eq. (2.1),

$$\Delta t = \frac{e^2}{2\pi m_e c} \times (\nu_{\rm lo}^{-2} - \nu_{\rm hi}^{-2})\mathrm{DM} \approx (4.15\,\mathrm{ms}) \times (\nu_{\rm lo}^{-2} - \nu_{\rm hi}^{-2})\mathrm{DM}. \tag{2.1}$$

where Δt is the time difference between the arrival of the pulse at two different frequencies, $\nu_{\rm lo}$ and $\nu_{\rm hi}$ are the lower and higher frequencies, respectively, m_e is the mass of the electron, c is the speed of light, and DM is the dispersion measure. The DM is defined as the integrated column density of free electrons (n_e) along the line of sight ($\mathrm{d}l$), as shown in eq. (2.2),

$$\mathrm{DM} = \int_0^d n_e \,\mathrm{d}l. \tag{2.2}$$

The dispersion measure of FRBs is determined using recursive DM searches to find the optimal DM value. Each frequency channel is then shifted in time (and phase) to correct for dispersion; this process is known as dedispersion, and it is critical to observe signals hidden in the noise.

Scintillation is caused by the IGM and ISM, which is a highly turbulent and inhomogeneous medium. These irregularities produce variations in phase, causing the observed intensity to fluctuate (a similar effect when visible planets blink at night). Meanwhile, the scattering effect is observed as the exponential tails in the pulse profile ($\propto \nu^{-4}$); this can be seen in some FRBs, as shown in fig. 2.1. This effect is related to the variable path lengths and, hence, arrival times of the rays as they are scattered by irregularities in the IGM (Lorimer & Kramer 2005). dispersion measure, scintillation, and scattering, along with values like pulse

width (ms-µs structure), polarization (Stokes parameters), and their localization (galactic host and redshift z), provide additional tools to classify FRBs and understand their origins.

2.2 Scattering matrix

Radio frequency and microwave circuits can be interpreted as n-port networks. An example of a 4-port network is shown in fig. 2.3, where a port can be treated as the networks input or output. At a specific point on the i-th port (with with $i \in [1, n]$), we can define a terminal plane, t_i, along with incident (V_i^+ , I_i^+) and reflected waves (V_i^-, I_i^-). This n-port network can be fully described by the scattering matrix. The scattering matrix is defined as the relation between the incident V_i^+ and reflected V_i^- voltage waves as shown in eq. (2.3),

$$\begin{bmatrix} V_1^- \\ V_2^- \\ \vdots \\ V_n^- \end{bmatrix} = \begin{bmatrix} S_{11} & S_{12} & \cdots & S_{1n} \\ S_{21} & S_{22} & \cdots & S_{2n} \\ \vdots & \vdots & \ddots & \vdots \\ S_{n1} & S_{n2} & \cdots & S_{nn} \end{bmatrix} \begin{bmatrix} V_1^+ \\ V_2^+ \\ \vdots \\ V_n^+ \end{bmatrix}, \tag{2.3}$$

or a condensed form of the S matrix,

$$[V^-] = [S][V^+]. \tag{2.4}$$

The elements of the scattering matrix are called scattering parameters S_{ij}. They are determined as:

$$S_{ij} = \left. \frac{V_i^-}{V_j^+} \right|_{V_k^+ = 0 \text{ for } k \neq j}. \tag{2.5}$$

Scattering parameters S_{ij} describe the portion of the power that enters port j and comes out of port i. In other words, they describe the transmission from one port to the other (transmission coefficient). Another case of importance is the S_{ii}, this value is equal to the reflection coefficient in port i. These definitions are only valid when all ports except the j-th port are set to zero. In real measurements, this can be done by terminating the unused port with a $50\,\Omega$ load. The scattering parameters can be obtained using network analysis techniques, but they are generally measured with a vector network analyzer (VNA; Pozar (2012)).

2.3 Transmission lines

Transmission lines are distributed-parameter networks where the phase and amplitude of a signal vary along their length. They become particularly relevant when the physical dimensions of a circuit are a significant fraction of the signal's wavelength (λ). At low frequencies and in compact PCB designs, these variations are often negligible. This could be the case of the FDM, where the nominal band corresponds to wavelengths ranging from approximately

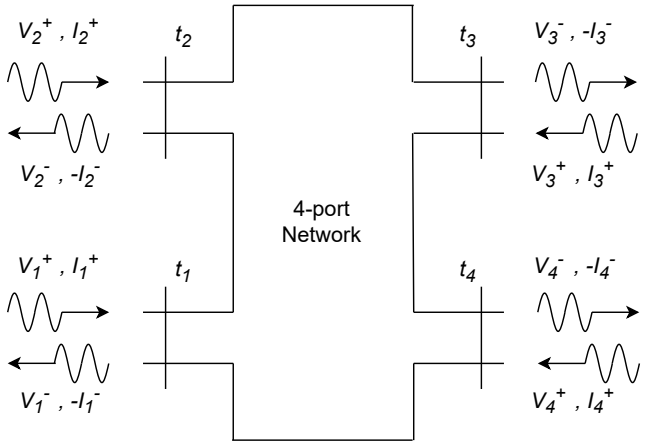

Figure 2.3: RF or microwave 4-port network. In the terminal planes t_i (with $i \in [1, 4]$), the incident (V_i^+ , I_i^+) and reflected waves (V_i^-, I_i^-) can be defined. Figure adapted from (Pozar 2012).

0.6–1 m. However the FDM upconverts the frequency up to 2366 MHz. At these higher frequencies, careful design of the transmission paths is essential to minimize losses and control phase variations.

The FDM was designed with two transmission lines: microstrip lines and coplanar waveguides (CPW). Both transmission lines had to be designed to have a characteristic impedance of 50 Ω. Most of the circuits are adapted to work at that impedance; if lines were not adapted, reflections inside the circuit will increase, and with that, the complexity of the FDM. The characteristic impedance Z_0 of the transmission line changes with frequency, the transmission line's structure, and the material's properties.

Printed circuit board (PCB) are usually made with a combination of conductor and substrate. Microstrip lines and coplanar waveguides are two transmission lines that can be easily incorporated into PCB designs. In these materials, the electromagnetic wave travels in two mediums: the air with a relative permittivity of $\varepsilon_{r_{\text{air}}} = 1$ and the substrate, which is a dielectric material with relative permittivity of $\varepsilon_r = \varepsilon/\varepsilon_0$, where ε is the frequency-dependent permittivity of the material and ε_0 is the vacuum permittivity. This change in medium produces different phase velocities of the waves, different from the speed of light in vacuum c, as shown in eq. (2.6),

$$v_p = \frac{c}{\sqrt{\varepsilon_r}}. \tag{2.6}$$

The propagated waves are not pure transverse electromagnetic (TEM), but the dielectric substrate is very thin ($d \ll \lambda$). Using the previous consideration, we can talk of quasi-TEM modes on microstrip and CPW.

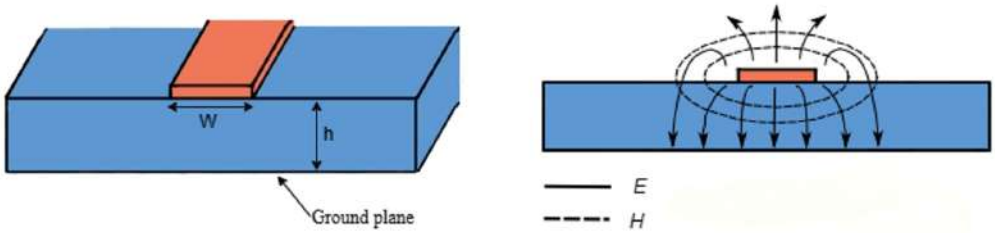

Figure 2.4: Microstrip transmission line structure on the left. Electric (E) and magnetic field (M) lines in a microstrip structure on the right. The orange line corresponds to the microstrip line; this structure is a conductor, generally copper, with a thickness $d = 35\,\mu\text{m}$ and width W. The substrate marked in blue is a dielectric material of relative permittivity ε_r and thickness h. Below the substrate, there is a ground plane made of a conductor of the same thickness d as the microstrip line. Normally $h \gg d$, but the dimensions were exaggerated in the figure for clarity. The E and M fields traverse in a quasi-TEM mode on the line, with the electric and magnetic fields marked as the continuous and dotted lines respectively. These figures were adapted from (Pozar 2012).

2.3.1 Microstrip lines

Microstrip lines are among the most popular planar transmission lines due to their easy incorporation into PCB designs and miniaturization. The structure of a microstrip line is shown on the left side of fig. 2.4. Where the line is made of a conductor of width W, this line is printed on a dielectric substrate of thickness h, and finally, a ground plane below is also made of a conductor (generally copper).

The behavior of the electromagnetic wave is observed on the right of fig. 2.4. As previously mentioned, the field lines propagate through the dielectric region and the air. This medium change means we cannot talk about the relative dielectric constant for all the microstrip structures. The concept of effective dielectric constant ε_{eff} appears to englobe those two mediums. This value will depend on the material, substrate thickness, conductor width, and frequency. An approximation of this value is given by eq. (2.7):

$$\varepsilon_{\text{eff}} = \frac{\varepsilon_r + 1}{2} + \frac{\varepsilon_r - 1}{2} \frac{1}{\sqrt{1 + 12d/W}}. \tag{2.7}$$

The effective dielectric constant can be used as the dielectric constant of a homogeneous medium. The characteristic impedance Z_0 of the transmission line is calculated relative to the line's dimensions (Pozar 2012),

$$Z_0 = \begin{cases} \dfrac{60}{\sqrt{\varepsilon_{\text{eff}}}} \ln\left(\dfrac{8h}{W} + \dfrac{W}{4h}\right), & \text{for } W/h \leq 1 \\ 120\pi \times \left\{ \sqrt{\varepsilon_{\text{eff}}} \left[\dfrac{W}{h} + 1.393 + 0.667 \ln\left(\dfrac{W}{h} + 1.444\right) \right] \right\}^{-1}, & \text{for } W/h \geq 1 \end{cases} \tag{2.8}$$

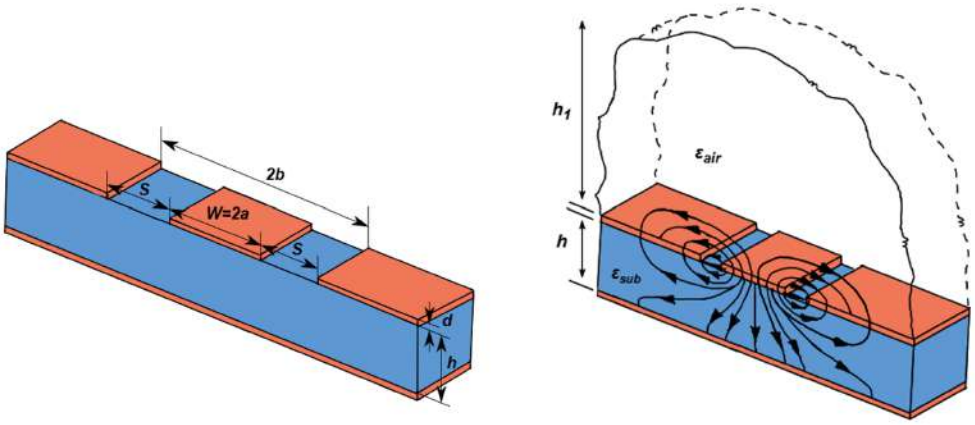

Figure 2.5: grounded coplanar waveguide (GCPW) structure on the left, the orange area corresponds to the conductor (typically copper) with thickness d and the blue area is the substrate with a thickness h. The line is defined by its width W and the separation to the ground plane S; these values can be written in terms of a and b to calculate the effective permittivity and characteristic impedance of the CPW. The field distribution is shown on the right, where the fields propagate in two media (ε_{air} and ε_{sub}) in a quasi-TEM mode. The length h_1 represents the end of the air medium; this value is only relevant when the line is closely covered in a conductor material. This figure was adapted from (Simons 2001).

2.3.2 Coplanar waveguides

Coplanar waveguides are transmission lines fabricated on a dielectric substrate, like the microstrip lines. Its structure consists of a center strip conductor with semi-infinite ground planes on either side, as shown on the left side of fig. 2.5. Where S is the separation between the line and the ground plane, W is the line's width, and h is the substrate's thickness. This structure also supports quasi-TEM mode of propagation as shown on the right of fig. 2.5. The main differences between CPW and microstrip lines are their fabrication advantages.

- It facilitates easy shunt and series surface mounting devices.
- It eliminates the need for wraparound and via holes.
- It reduces radiation loss.
- Ground plane exists between two adjacent lines, which decreases the crosstalk effects between adjacent lines.
- It gives more room to change the line size compared to microstrip lines because it has more parameters to adjust.

The main problem with CPW lines is that the losses are higher compared with microstrip lines. The specific type of CPW used in this work was the GCPW, also known as conductor-backed coplanar waveguides (CBCPW). The structure of this type of line is shown in fig. 2.5, and its only change is that they have a lower ground plane that provides mechanical strength to the PCB.

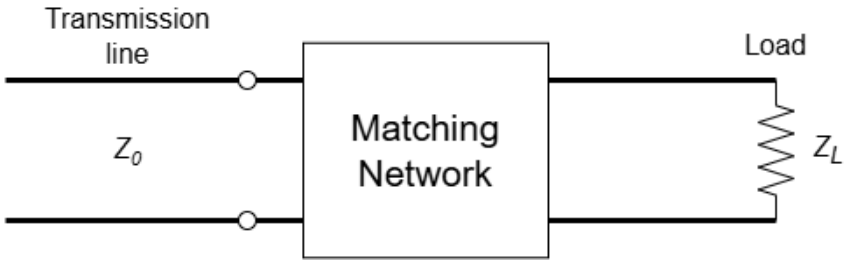

Figure 2.6: Lossless network matching a load impedance Z_L to a transmission line. Figure adapted from (Pozar 2012).

The GCPW effective permittivity and characteristic impedance are obtained as:

$$\varepsilon_{\text{eff}} = \frac{1 + \varepsilon_r \frac{K(k')}{K(k)} \frac{K(k_3)}{K_3'}}{1 + \frac{K(k')}{K(k)} \frac{K(k_3)}{K_3'}}, \tag{2.9}$$

and

$$Z_0 = \frac{60\pi}{\sqrt{\varepsilon_{\text{eff}}}} \frac{1}{\frac{K(k)}{K(k')} + \frac{K(k_3)}{K_3'}}. \tag{2.10}$$

Where

$$k = \frac{a}{b}, \quad k_3 = \frac{\tanh(\pi a/2h)}{\tanh(\pi b/2h)}, \quad k' = \sqrt{1-k^2}, \quad k_3' = \sqrt{1-k_3^2}. \tag{2.11}$$

And $K(k)$ is an elliptic integral of the first kind. These values can be calculated using existing tools in simulation programs like Cadence AWR (Systems 2023) or characteristics impedance calculators available online. They use the same principles mentioned in eq. (2.9) and eq. (2.10).

2.4 Impedance matching

Impedance matching is a fundamental practice in RF circuit design. Figure 2.6 shows an example of a matching network. The load Z_L represents the element that needs to be connected to the transmission line. In some cases, a component in the circuit may have a load impedance different from the characteristic impedance Z_0 of the transmission line. A considerable portion of the signal will be reflected if the impedance-matching network is not placed before the load. In other words, impedance-matching networks are used to maximize the power delivered to the load.

There are different types of impedance-matching structures. One simple matching technique uses open-circuited or short-circuited sections of a transmission line (a stub) connected in parallel or series. These techniques are easy to add in microstrip lines or coplanar waveguides, but they might not fit compact PCB designs. The same problem happens with quarter-wave transformers; this technique requires using a portion of length $\lambda/4$ in the transmission lines, which is not always possible in long wavelength circuits or more compact PCB structures. Other matching networks, like multisection transformers, can be used for more

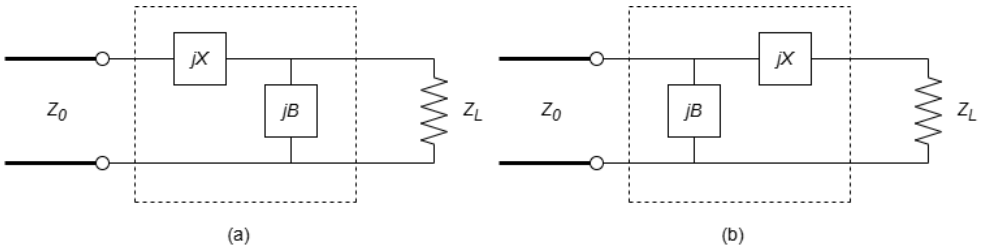

Figure 2.7: L section impedance matching network marked with the dotted line. Two configurations (a) and (b) of reactive X and B components can be used to match the load Z_L. Figure adapted from (Pozar 2012).

bandwidth applications, but they were not studied because CHARTS bandwidth does not require those features.

2.4.1 L-networks

An L-section impedance matching network (L-network) uses two reactive elements, such as capacitors (C) and inductors (L). There are two possible configurations of this type of network, as shown in fig. 2.7. The elements X and B are reactive, and their values depend on the configuration ((a) or (b)), the characteristic impedance Z_0, and the load impedance Z_L. The load impedance can be expressed as a complex number: $Z_L = R_L + jX_L$, where R_L is the real part and X_L is the imaginary part.

The configuration used depends on the position of the normalized load impedance $z_L = Z_L/Z_0$ relative to the circle $1+jx$ on the Smith chart (Smith 1939), where x is the normalized reactance of the element X. In case (a), the normalized load lies inside the $1 + jx$ circle, which implies that $R_L > Z_0$. In this case, B and X are used as standard series and parallel reactive components. The impedance seen when looking into the matching network (toward the load) must equal Z_0, as shown in eq. (2.12):

$$Z_0 = jX + \frac{1}{jB + 1/(R_L + jX_L)}. \tag{2.12}$$

Separating the real and imaginary part of eq. (2.12) and solving for B we get the next solution:

$$B = \frac{X_L \pm \sqrt{R_L/Z_0}\sqrt{R_L^2 + X_L^2 - Z_0 R_L}}{R_L^2 + X_L^2}. \tag{2.13}$$

As $R_L > Z_0$ the argument of the second square root is always positive. Then the series reactance is:

$$X = \frac{1}{B} + \frac{X_L Z_0}{R_L} - \frac{Z_0}{B R_L}. \tag{2.14}$$

There are two possible solutions for B and X. Positive values for X indicate that we have to use an inductor and a negative capacitor. For B is the other way around. The same can

be done using circuit (b), where the solutions for X and B are:

$$B = \pm\sqrt{R_L(Z_0 - R_L)} - X_L \quad \text{, and} \quad X = \pm\frac{\sqrt{(Z_0 - R_L)/R_L}}{Z_0}. \tag{2.15}$$

L-networks are usually designed with a Smith chart (Smith 1939). There are also other digital tools and simulation software used to design L networks, like AWR Systems (2023) and its Smith chart analysis capabilities.

L-networks usage stops being useful once the L, C components of length ℓ become relatively big compared with the wavelength. Theoretically, lumped components can be used up to 60 GHz or higher if the $\ell < \lambda/10$ condition is satisfied. However, LC components are far from ideal, and they can add undesirable effects such as parasitic capacitance or inductance, spurious resonances, more losses, fringing fields, and perturbations caused by ground planes. This and the physical limits of the capacitors and inductors are the limitations of the L-section (Pozar 2012).

2.5 Thermal noise

Most of the noise in radio systems is generated through thermal emission in any component at temperatures above absolute zero. This thermal noise can come from external sources or be generated internally by the system. It sets the fundamental sensitivity limit, defining the weakest signal the system can detect. A key challenge in radio astronomy is that the astronomical signal is also characterized as a thermal noise source. This means that the system must be able to distinguish the desired signal from all the external and undesired noise.

Any component with temperature T will have its electrons in a random motion, proportional to the temperature. These motions produce small random fluctuations at the component terminals. This is read in the system as a change in the voltage amplitude of the signal. The average of this voltage (V_n) can be described by Planck's blackbody radiation law shown in eq. (2.16), where h is Planck's constant, k_B is Boltzmann's constant, T is the temperature in Kelvin, B is the bandwidth of the system, ν is the center frequency of the bandwidth, and R is the resistance in Ω,

$$V_n = \sqrt{\frac{4h\nu\ BR}{e^{\frac{h\nu}{k_B T}} - 1}}. \tag{2.16}$$

In radio frequencies, we can use the Rayleigh-Jeans approximation $h\nu \ll k_B T$. This simplifies Planck's law to:

$$V_n = \sqrt{4k_B TBR}. \tag{2.17}$$

Using this value to obtain the power delivered to a load in a bandwidth B we get 2.18,

$$P_n = \left(\frac{V_n}{2R}\right)^2 R = k_B TB. \tag{2.18}$$

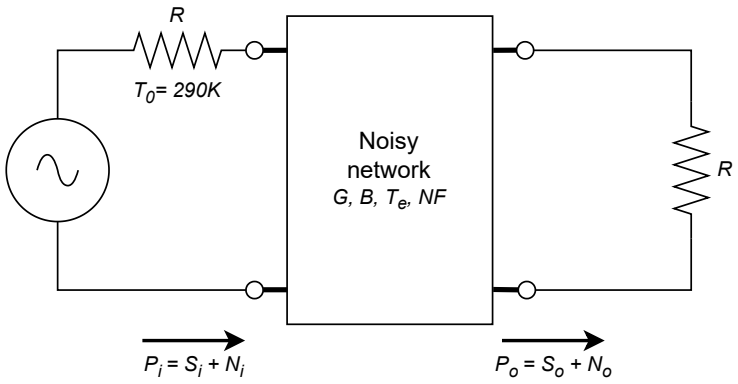

Figure 2.8: Noisy network characterized by a gain G, a bandwidth B, noise temperature T_e, and noise figure NF. Figure adapted from (Pozar 2012).

2.5.1 Noise figure

The noise figure is an alternative characterization of the noise of a network, similar to the noise temperature previously defined. Manufacturers commonly use it as one of the amplifier parameters. The noise figure of a component is a measure of degradation in the signal-to-noise ratio (SNR) between the input and the output. The noise figure NF is defined in eq. (2.19), where S_i and N_i are the input signal and noise powers, and S_o and N_o are the output signal and noise powers. The input is assumed to be the noise power from a matched resistor at $T_0 = 290\,\mathrm{K}$. As shown in fig. 2.8, the network is characterized by its temperature T_e, gain G, and bandwidth B. Considering the noise power defined in eq. (2.18), the noise figure results in:

$$\mathrm{NF} = \frac{S_i/N_i}{S_o/N_o} = 1 + \frac{T_e}{T_0} \geq 1. \tag{2.19}$$

The definition of noise figure is only valid under specific conditions: the input source must be impedance-matched, and the noise source must be at room temperature, $T_0 = 290\,\mathrm{K}$. Another important case involves passive components; here, there is not an associated gain G but a loss factor defined as $L = 1/G > 1$. For networks with only losses, the noise power and noise figure are given by:

$$T_e = \frac{1-G}{G}T = (L-1)T \quad \text{and} \quad \mathrm{NF} = 1 + (L-1)\frac{T}{T_0}. \tag{2.20}$$

As observed in eq. (2.20), if the network is at room temperature, then NF $= L$. This relation will be most of the time correct, specifically for passive components.

Noise figure and noise power are usually written in terms of decibels (dB). The values in dB can easily characterize a radio frequency network. For example if there are two lossy components in series with loss factor in dB of L_1 and L_2 then the final loss of the system is $L = L_1 + L_2$.

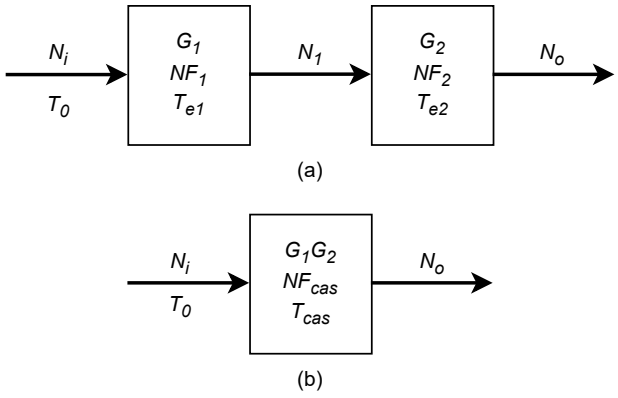

Figure 2.9: Cascaded system, (a) shows the original two networks, and (b) shows the equivalent network. The intrinsic noise on the output N_o is affected by the parameters: G_1 and G_2 which are the gains, NF_1 and NF_2 are the noise figures, and T_{e1} and T_{e2} are the equivalent temperatures of network one and two. The cascaded system can be merged into an equivalent network with parameters $G_{\mathrm{cas}} = G_1G_2$, NF_{cas}, and T_{cas}. Figure adapted from (Pozar 2012).

Cascaded systems

The noise temperature and noise figure definitions can be used for cascaded systems. Each component is defined to have its respective gains, noise figures, and temperatures, as shown in fig. 2.9. The noise characteristics of a cascaded system are dominated by the characteristics of the first elements. This means that selecting the first element with a high gain and low noise figure will improve the overall noise performance of the system. In RF circuits, this is implemented with the addition of low-noise amplifiers (LNAs) as the first element of the RF chain.

In fig. 2.9 (a), the noise power at the end of network one is given by the addition of the initial power amplified by G_1 and the intrinsic noise of network one:

$$N_1 = G_1kT_0B + G_1kT_{e1}B. \tag{2.21}$$

The same happens in the cascaded systems output:

$$N_o = G_2N_1 + G_2kT_{e2}B = G_1G_2kB\left(T_0 + T_{e1} + \frac{1}{G_1}T_{e2}\right). \tag{2.22}$$

For the equivalent cascade system we can write $N_0 = G_1G_2kB(T_{cas} + T_0)$. In terms of noise temperature and noise figure, the expression can be written as:

$$T_{cas} = T_{e1} + \frac{1}{G_1}T_{e2} \quad \text{and} \quad \mathrm{NF}_{cas} = \mathrm{NF}_1 + \frac{1}{G_1}(\mathrm{NF}_2 - 1) \tag{2.23}$$

The last expressions can be expanded for N cascaded elements, which give 2.24 and 2.25, also known as the Friis noise formula (Fouquet 2020). If a passive component is in the jth

position of the cascade system, the gain G_j should be replaced by the loss factor $L_j = 1/G_j$. None of the previous values are in dB, so the data should be converted before applying these formulae:

$$T_{cas} = T_{e1} + \frac{T_{e2}}{G1} + \frac{T_{e3}}{G1G2} + \cdots + \frac{T_{eN}}{G_1 G_2 \cdots G_{N-1}}, \tag{2.24}$$

and

$$\mathrm{NF}_{cas} = \mathrm{NF}_1 + \frac{\mathrm{NF}_2 - 1}{G1} + \frac{\mathrm{NF}_3 - 1}{G1G2} + \cdots + \frac{\mathrm{NF}_N - 1}{G_1 G_2 \cdots G_{N-1}}. \tag{2.25}$$

2.6 Radio receivers and radio components

A radio receiver is a principal component in communication systems and in radio astronomy. Its principal function is to distinguish signals from noise. In radio astronomy, the signal is also a form of noise; therefore, we want to separate the wanted noise from the noise we do not want (Carr 2002). This is possible by improving the SNR. The SNR tells us the chance of detecting the signal from the noise. As defined previously, having low noise figure components as the first elements in the RF chain can reduce the overall noise figure of the system. The simplest form of the SNR equation is given by:

$$\mathrm{SNR} = \frac{P_{\mathrm{signal}}}{P_{\mathrm{noise}}}. \tag{2.26}$$

One of the most used receivers is the superheterodyne receiver. The purpose of a superheterodyne receiver is to convert the incoming RF frequency to a single intermediate frequency (IF), where most of the signal processing takes place. The IF can be either higher or lower than the RF frequency. The process of converting the RF to the IF is called up-conversion or down-conversion, depending on whether the IF frequency is higher or lower than the RF frequency. This process uses nonlinear components called mixers that combine the RF frequency with an external local oscillator.

The general structure of a radio receiver is shown in fig. 2.10. Its first component is the LNA, followed by the mixer, and a bandpass filter. The bandpass filter separates the desired IF signal from all the other signals generated in the nonlinear transformation of the mixer. Then it can be amplified again to improve the signal analysis.

2.6.1 Frequency mixers

A mixer is a device that performs the frequency conversion in radio receivers. In principle, any circuit element with a nonlinear relation between input voltage and output current can be used as a mixer; an example is semiconductor devices like diodes. To work as intended, mixers need the RF input signal and an LO. The nonlinear behavior of the mixer produces various frequency elements that are the products of the combination of RF and LO signals. However, derivations of mixer properties are simpler for a device with a purely quadratic characteristic (Wilson et al. 2009). The relation between current and voltage in a quadratic

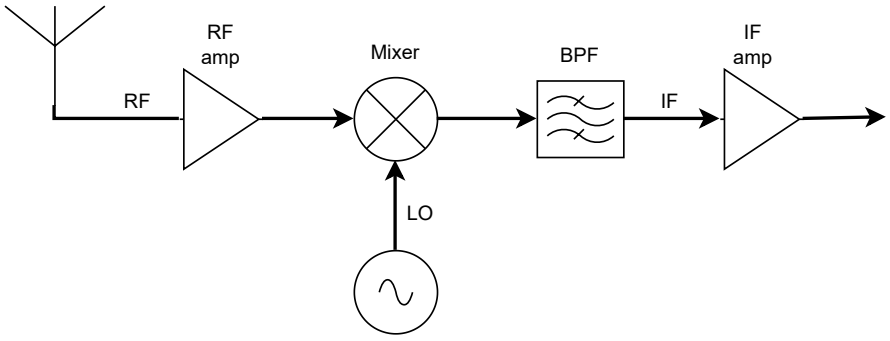

Figure 2.10: Block diagram of a single-conversion superheterodyne receiver. Its structure is composed of an RF amplifier, a mixer fed with an LO signal, a bandpass filter noted as BPF, and a final IF amplifier. The figure was adapted from (Pozar 2012).

nonlinear element is given by:

$$I = \alpha U^2, \tag{2.27}$$

where U is the sum of the input signal $E\sin(2\pi\nu_{RF}t+\delta_{RF})$ and the local oscillator $V\sin(2\pi\nu_{LO}t+\delta_{LO})$. Then the output gives a combination of different frequencies,

$$\begin{aligned} I &= \alpha[E\sin(2\pi\nu_{RF}t+\delta_{RF}) + V\sin(2\pi\nu_{LO}t+\delta_{LO})]^2 \\ &= \alpha E^2\sin^2(2\pi\nu_{RF}t+\delta_{RF}) + \alpha V^2\sin^2(2\pi\nu_{LO}t+\delta_{LO}) \\ &\quad + 2\alpha EV\sin(2\pi\nu_{RF}t+\delta_{RF})\sin(2\pi\nu_{LO}t+\delta_{LO}). \end{aligned} \tag{2.28}$$

Using trigonometric addition formulae in the previous equation, we obtain:

$$\begin{aligned} I = {} & \frac{1}{2}\alpha(E^2+V^2) && \text{(DC component)} \\ & - \frac{1}{2}\alpha E^2\sin(4\pi\nu_{RF}t+2\delta_{RF}+\pi/2) && \text{(Second harmonic of signal)} \\ & - \frac{1}{2}\alpha V^2\sin(4\pi\nu_{LO}t+2\delta_{LO}+\pi/2) && \text{(Second harmonic of LO)} \\ & + \alpha VE\sin[2\pi(\nu_{RF}-\nu_{LO})t+(\delta_{RF}-\delta_{LO}+\pi/2)] && \text{(Difference frequency)} \\ & + \alpha VE\sin[2\pi(\nu_{RF}+\nu_{LO})t+(\delta_{RF}+\delta_{LO}+\pi/2)] && \text{(Sum frequency)} \end{aligned} \tag{2.29}$$

Using only the mixer's quadratic component, we obtain two elements that change the signal's frequency: the frequency sum and difference. Those two components are part of the IF signal, but generally, only one is needed in the receiver. The other components are also unwanted, so we use bandpass filters to select the correct IF frequency.

The complete function of the current can be expressed as a Taylor series expansion. So, the current has different components raised at various frequencies; as seen before, the quadratic term produces the desired IF frequencies. Meanwhile, the higher-order elements produce unwanted harmonics, intermodulation products, and other spurious signals. In the frequency domain, all the output frequencies are given by eq. (2.30),

$$\pm\nu_{\text{out}} = m\nu_{RF} \pm n\nu_{LO}. \tag{2.30}$$

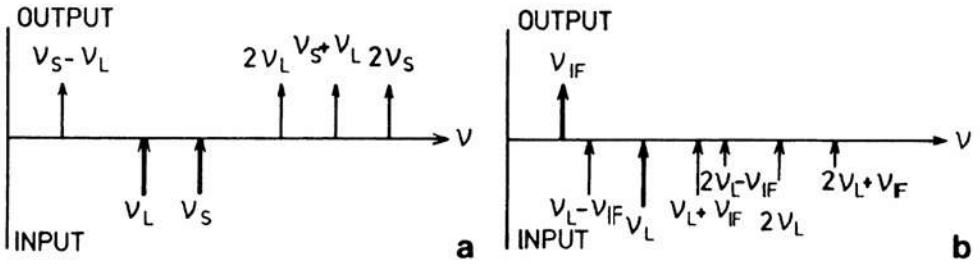

Figure 2.11: Input and output frequencies of a mixer. The thick arrows are the given values. Figure extracted from (Wilson et al. 2009)

Where ν_0 is the output frequency produced for a specific n and m pair, these values are integers or zero, and ν_{RF} and ν_{LO} are the input frequencies. Most of these products are undesired harmonics and spurious signals. We call them intermodulation products.

As seen in fig. 2.11 and the previous equations, the mixer output consists of the superposition of several components at different frequencies:

- The direct current (DC) signal
- Harmonics of the RF signal and the LO
- The difference and the sum of RF and LO frequencies
- Spurious signals produced by the different m,n combinations

While the amplitudes of all other components depend on the second power of the signal or local oscillator amplitude, the sum and difference frequency signals depend on the first power. Thus, their amplitudes are accurate reproductions of the input signal's amplitude.

Another important point in the output is how we specify the system; for example, in fig. 2.11, the given values are the LO and RF signals, leaving the IF unspecified. However, in some cases, the system is limited by the sampling rate of the analog-to-digital converters (ADCs), which means that selecting the IF and LO signal (see fig. 2.11b) can be a better solution. In this case, both sidebands $\nu_{LO} - \nu_{IF}$ and $\nu_{LO} + \nu_{IF}$ contribute to the IF signal, but only one of them is wanted. This can be solved by using an appropriate bandpass filter. However, in most cases, adding a filter before the mixer can increase the receiver's losses and the system's temperature.

Mixer parameters

Mixers can be treated like a three-network RF circuit. However, its nonlinear response and multiple outputs give multiple parameters to characterize a mixer. The most important parameters in the mixer are:

- Conversion loss or gain

- Noise figure
- Third-order intercept point
- LO-IF isolation
- RF-IF isolation
- LO-RF isolation
- Minimum LO power
- Reflections from ports

Conversion losses are calculated as the input RF power vs the output IF power. The noise figure (NF) is usually specified in active mixers or mixers with amplifiers included; if those elements are absent, the NF will equal conversion losses. If the RF input power increases to a certain degree, the mixer will stop working in its linear region. When this happens, the third-order (and higher) intermodulation products exceed the receiver noise floor, increasing the number of spurious signals. As seen in fig. 2.12, for every 1 dB increase in the fundamental signal, there is an increase of 3 dB in the third-order response. Although the output response of the third-order line saturates similarly to that of the fundamental signal, the gain line can be continued to a point where it intersects the gain line of the fundamental signal. This point is the third-order intercept point (TOIP). The decrease in power of the output signal is due to the nonlinear region of the mixer. When this slope decreases by 1 dB, it's called the 1dB compression point. The idea is to not saturate the mixer beyond the TOIP and the 1dB compression point (1dB) compression point.

The first-order elements, like the RF and LO signals, have higher amplitude compared with the rest of the signals. This can lead to difficulties in suppressing them. The portion of the RF and LO signals present in the mixer's IF port are called LO-IF and RF-IF isolations. Meanwhile, part of the LO and IF that can be transmitted back towards the RF input are called IF-RF isolation and LO-RF isolation.

Double balance mixers

The type of mixer that suppresses the ν_{LO} and ν_{RF} in the output is called double balance mixer, its structure is shown in fig. 2.13. These devices can also suppress even order of LO and RF harmonics.

The structure of a double balanced mixer is composed of four diodes in a ring or star configuration, along with two baluns (one each for the RF and LO). This type of mixer provides rejection of both the LO and RF content at the IF output. This isolation between mixers prevents the system from using external filters for the RF and LO frequencies. Double-balanced mixers are known for their linearity and broader bandwidths. However, this mixer requires higher LO powers, and the ports are sensitive to reactive terminations.

The diode ring works as an ON-OFF switch controlled by the local oscillator. When the LO is positive, one half of the ring will be ON and the other half OFF, the same as when the

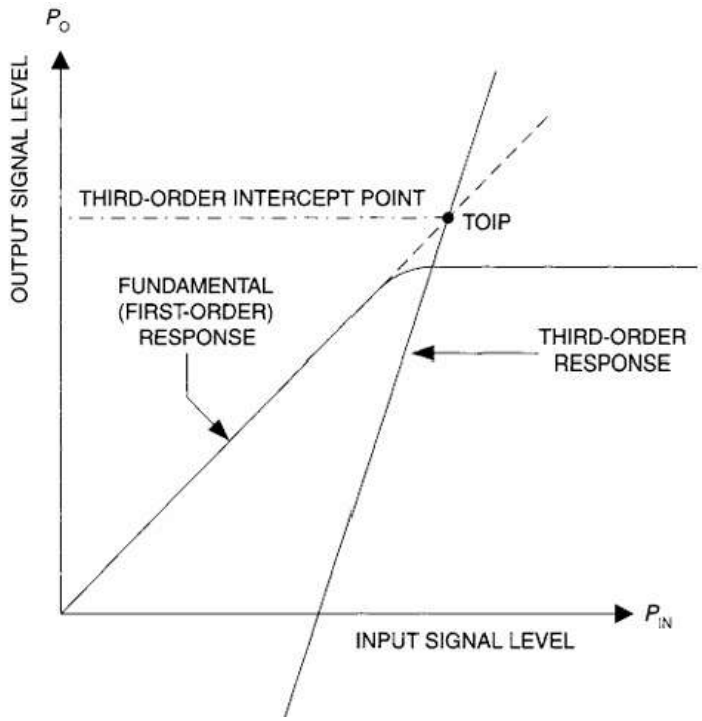

Figure 2.12: Third-order intercept point and saturation of the fundamental response. The vertical and horizontal axes are the output power P_O and input power P_{IN}. If the input power increases to a certain degree, the mixer will saturate. Therefore, the first-order response will not be linear. The third-order response (generally unwanted harmonics) starts being higher than the fundamental response after the TOIP; this point usually occurs after the saturation. Figure extracted from (Carr 2002).

LO signal is negative. This generates the IF frequency. Meanwhile, this symmetric structure provides better LO-IF and RF-IF isolations. In some cases, the IF output can be differential, so that it will need external baluns in the output.

2.6.2 Filters

Filters are passive components used to allow certain frequencies to pass while blocking others. They are essential in selecting the desired signal and rejecting unwanted signals and noise. The frequency band over which the filter passes is called the passband, and the frequency band it rejects is called the stopband. The filter frequency response is classified according to its passband and stopband boundaries. The most common ones are:

- Low-pass filter: it passes frequencies below a cutoff frequency (f_c) while the rest is attenuated.
- High-pass filter: it passes frequencies above f_c while attenuating frequencies below it.
- Band-pass filter: it passes frequencies between an upper and lower cutoff frequencies.
- Band-stop filter: Attenuates frequencies between a lower and upper cutoff frequencies.

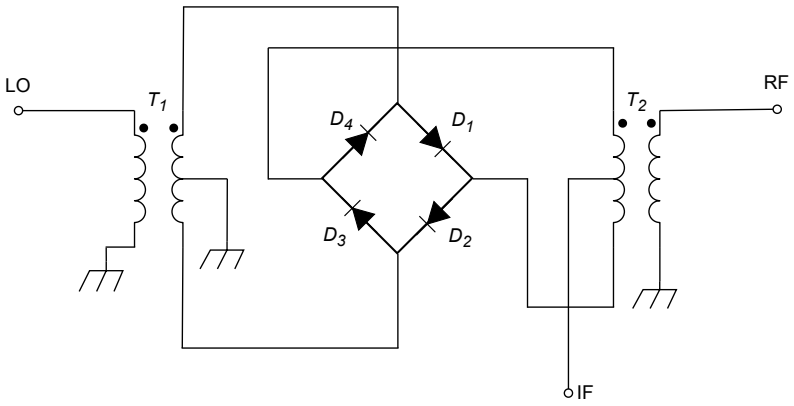

Figure 2.13: Typical structure of a double-balanced mixer. The diode ring composed of D_1, D_2, D_3, and D_4 works as an ON-OFF switch controlled by the LO, finally generating the IF signal and all the mixer products. The baluns or transformers T_1 and T_2 enhance the port isolations of this type of mixer. Figure adapted from (Carr 2002).

They can be described as two-port networks. These networks are reciprocal, meaning that $S_{12} = S_{21}$ and only three parameters are needed to describe their response, S_{11},S_{21}, and S_{22}. The common parameters are obtained from these S values:

- Insertion loss (dB) $= -20\log_{10}(|S_{21}|)$
- Input return loss (dB) $= -20\log_{10}(|S_{11}|)$
- Output return loss (dB) $= -20\log_{10}(|S_{22}|)$
- Phase (rad): $\phi = arg(S_{21})$
- Group delay (sec): $\tau_d = -\frac{1}{2\pi}\frac{d\phi}{df}$

Filters can be designed with lumped elements like resistors, capacitors, and inductors, as observed in fig. 2.14(a). These types of designs can be implemented as periodic structures to increase the order of the filter and thus the sharpness of it.

The cut-off frequency is defined as the frequency where the output power decreases to half the passband power. In terms of decibels, this means that the f_c is found -3 dB below the central passband frequency.

2.6.3 Equalizers

Most transmitter and receiver systems experience decreasing gain and increasing losses at progressively higher frequencies. The equalizer is a component designed specifically to compensate for this natural tendency toward roll-off exhibited by these systems. An equalizer is essentially an attenuator placed in a circuit or system that exhibits maximum insertion loss at lower frequencies; examples of equalizer insertion losses are shown in fig. 2.15. Equalizers

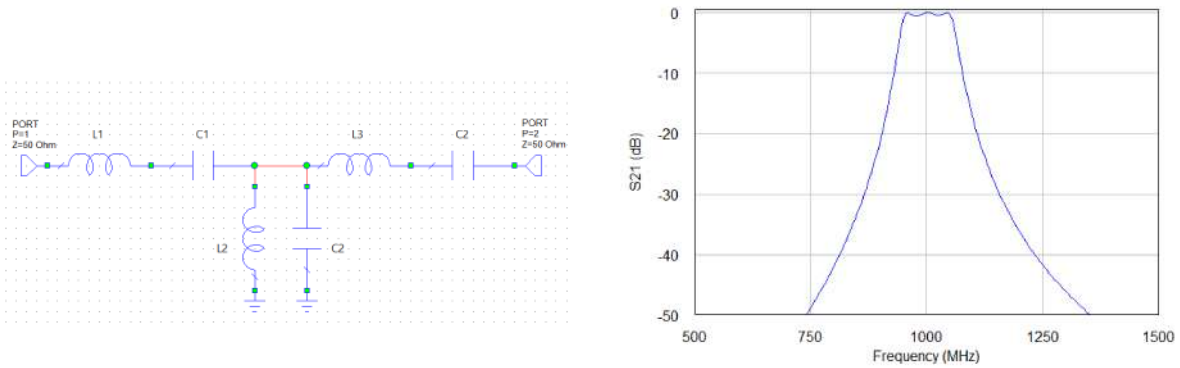

(a) (b)

Figure 2.14: Bandpass filter constructed with lumped elements, the components L_1, L_2, and L_3 are inductances. Meanwhile the components C_1, C_2, and C_3 are capacitances. The response of the filter shown in (b) has the insertion losses on the vertical axis, and the frequency on the horizontal axis. The schematic and the filter response were obtained from the simulation software Cadence AWR (Systems 2023).

Table 2.1: Power combiner theoretical insertion losses.

Number of Output Ports	Theoretical Insertion Loss (dB)
2	3.0
3	4.8
4	6.0
5	7.0
6	7.8
8	9.0
10	10.0

are added in cascade RF circuits to tilt the gain response positively. The magnitude by which the equalizer tilts the system gain response from minimum to maximum operating frequency is called its equalization value or "slope".

2.6.4 Power combiners

Power combiners or power splitters (the same circuit) are passive devices that accept multiple input signals and combine them into one. The circuit operates as a splitter when power is applied to the common port and delivered to the independent ports. When power is applied to the independent ports, the combination of individual signals is added linearly at the common port and acts as a combiner. Combiners and splitters act the same way, independent of where the input signal is. The minimum insertion losses of these devices are dependent on the number of independent ports N, as Insertion loss (dB) $= 10\log_{10}(N)$. The common number of independent ports is shown in table 2.1.

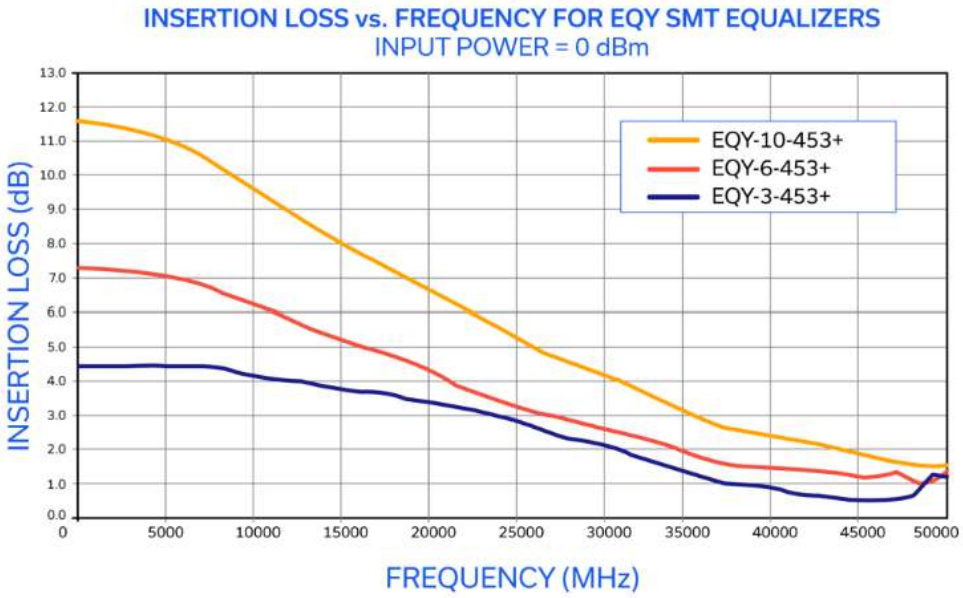

Figure 2.15: Typical response of three commercial equalizers from Minicircuits. These three different equalizers EQY-10-453+, EQY-6-453+, and EQY-3-453+ attenuate the signal more at lower frequencies, and they have slopes of 10 dB, 6 dB, and 3 dB, respectively. Figure extracted from (Mini-Circuits 2023a).

To understand the parameters in a power combiner, we can use a 3-port power combiner as an example. If port 1 is the sum of ports 2 and 3, then the S parameters are:

$$[S] = \begin{bmatrix} S_{11} & S_{12} & S_{13} \\ S_{21} & S_{22} & S_{23} \\ S_{31} & S_{32} & S_{33}, \end{bmatrix} \tag{2.31}$$

The device is passive, so the S matrix is symmetrical, meaning $S_{ij} = S_{ji}$. The values S_{12} and S_{13} are the insertion losses of the combiner. The values S_{ii} correspond to the input return losses of the device. Finally, the transmission between the input ports S_{32} is the isolation between ports. Ideally, power combiners should have high isolations between ports, but this will depend on the architecture. For applications like the FDM, the isolation is a crucial parameter to consider in power combiners. Another important point is that the phase shift between ports is usually 0°.

T-junctions

The most basic type of power combiners is the T-junction. The structure is symmetrical as shown in fig. 2.16. The signal applied in one port will be divided into two signals with equal amplitude and phase.

This kind of combiner has the limitations of poor isolation and impedance mismatch. The problem with isolation is observed when one of the ports is terminated in a load, short, or open circuit. For example, if the output is terminated by a matched impedance, the isolation

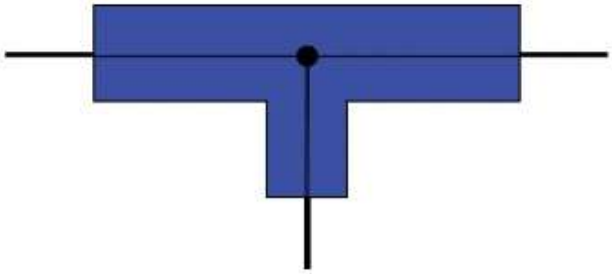

Figure 2.16: Two-way combiner, T structure. Figure extracted from (Mini-Circuits 2023b).

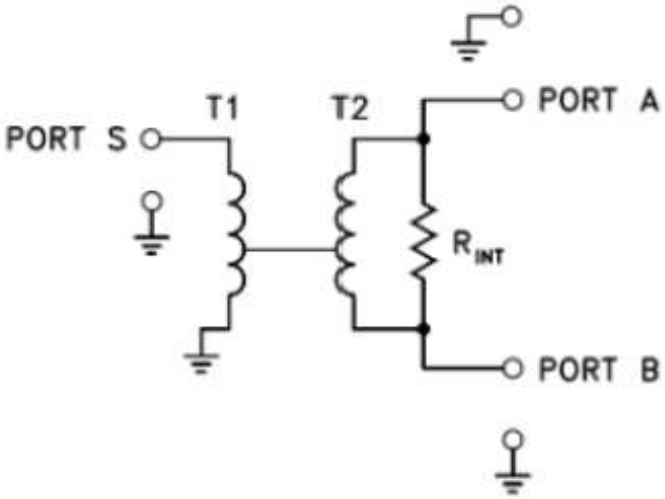

Figure 2.17: Core and wire combiner general structure. A and B are the input ports, and port S is the output port where the signals are combined. $T1$ is a 2:1 impedance matching transformer. The resistor R_{INT} and transformer $T2$ help the combiner to increase the isolation between ports A and B. Figure extracted from (Mini-Circuits 2023b).

would be 3 dB because part of the signal will travel to the matched impedance and the other half to the second port. Meanwhile, if the output port is open, then the input ports would have zero isolation between them.

Core and wire combiners

The core and wire combiner seen in figure 2.17 solves the problem of the isolation and impedance mismatch. In case of the isolation, if an input signal is applied to port A, a current will flow through the transformer and experience a 180° phase shift by the time it arrives at port B. At the same time, the current will flow through the resistor R_{INT} without experiencing a phase shift. If R_{INT} equals the impedance value across the transformer ends, then the signal from port A will cancel at port B. The impedance mismatch is solved by adding a second transformer T1 to match the impedance in port S.

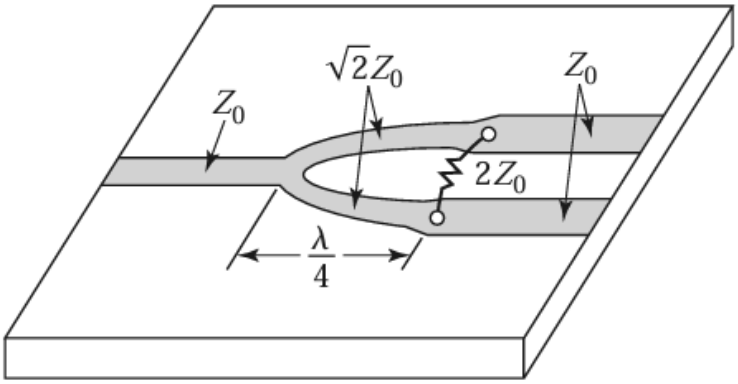

Figure 2.18: Two-way Wilkinson power combiner in a microstrip structure. The initial characteristic impedance Z_0 is adapted by the impedance matching line of $\sqrt{s}Z_0$ and length $\lambda/4$. A resistor is added between two ports to increase their isolation; this resistor is usually a 100 Ω. Figure extracted from (Pozar 2012).

Wilkinson combiners

The Wilkinson power divider is a network usually made with microstrip transmission lines. Its structure is shown in fig. 2.18. Z_0 is the characteristic impedance of the transmission line, usually 50 Ω. Then the separation is made in the microstrip structure, the new transmission lines should be designed to have an impedance of:

$$Z_0' = Z_0\sqrt{N} \tag{2.32}$$

Where N is the number of input ports of the combiner and Z_0' is the new characteristic impedance of the line. These microstrip lines have a length of $\lambda/4$, which reduces the reflected power from the input to the output port. The load $2Z_0$ between the output ports can dissipate incoming reflected signals, increasing the isolation between ports.

2.7 CHARTS

Canadian-Chilean Array for Radio Transient Studies will be an aperture array interferometer of $n_a = 256$ single-polarized antennas, designed primarly for the detection of FRBs. Operating within a passband of $\Delta\nu = 300$–500 MHz, CHARTS targets a frequency range where FRB detections suggest these phenomena are brighter at lower frequencies (CHIME/FRB Collaboration et al. 2021). Additionally, the passband will also overlap with that of CHIME/FRB, allowing for a comparison between detections on both radio telescopes. CHARTS specifications were selected to optimize the detection rate of FRBs, which scales as $\propto n_a\Delta\nu^{0.75}$, therefore it is best to increase the number of antennas n_a rather than having a wide bandwidth.

CHARTS dedicated survey will be mostly focused on the nearest and brightest FRBs (i.e. DM excess $< 100\,\mathrm{pc\,cm^{-3}}$). With some assumptions, we can estimate that CHARTS will

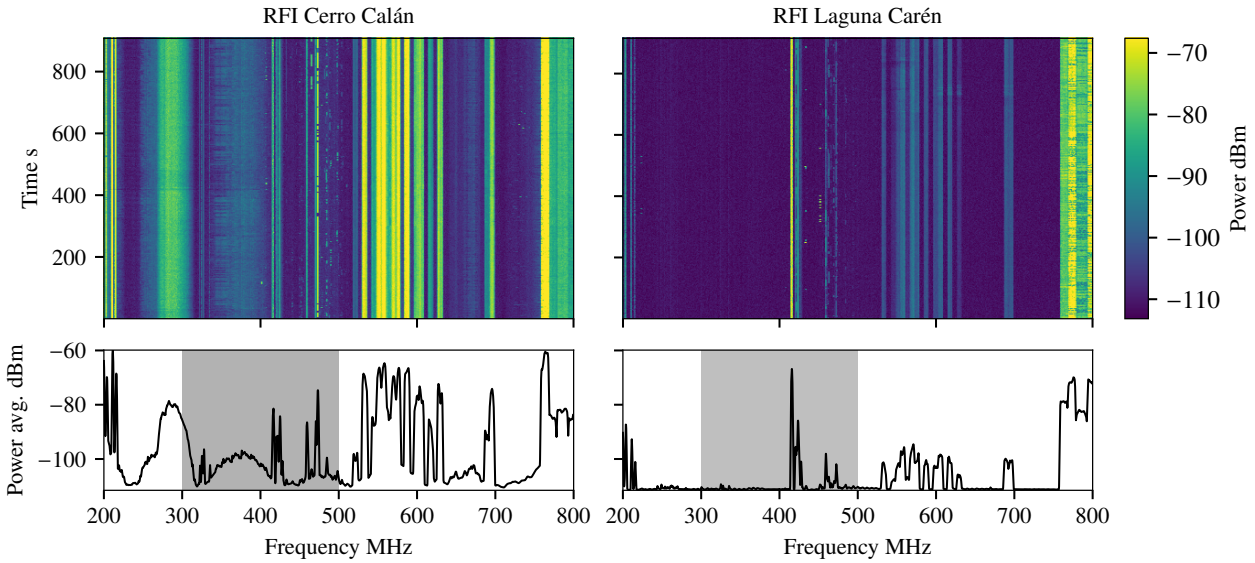

Figure 2.19: Preliminary measurements of RFI in cerro Calán and Laguna Carén made with Siglent spectrum analyzer. The measurements were made over 15 minutes, covering frequencies from 200–800 MHz. The gray area corresponds to CHARTS bandwidth. Meanwhile, the rest of the bright signals correspond to RFI.

detect ∼100 FRBs per year.

CHARTS will be built in the Laguna Carén, Región Metropolitana, Chile (latitude −33°). The site belongs to Universidad de Chile, and it is equipped with minimal electric infrastructure to build the radio array, and other necessary facilities for CHARTS to deploy components and process FRB data. After preliminary observations, we measured low RFI levels in Laguna Carén, see fig. 2.19, showing that in CHARTS range the observation will be mostly clean of external noise. In addition, there's a plan to set up an eight-antenna prototype for the first CHARTS version, called CHARTS-8. This first radio array will be built in cerro Calán, Santiago, Chile. Similar RFI measurements have been made within the city, indicating the preference for Laguna Carén.

One of the essential components of CHARTS is its digitizers. The digitizer is the component that converts the analog information from the antennas into digital data. They are usually part of a FPGA; one of the most modern boards that can be used is the RFSoC. The RFSoC has four available 5 GSPS ADCs, so the board can accept up to four antenna signals. This ADCs can measure signals up to 2.5 GHz, comparing that with CHARTS bandwidth of 200 MHz, it is clear that the sampling frequency of the ADCs is not used efficiently. To solve this problem, the FDM board will be used. This board combines eight antennas into a single output, fully utilizing the ADCs sampling frequency. Adding the FDM will also reduce the number of digitizers to 32, making the FDM board a key component in the CHARTS project.

The structure of CHARTS is separated into "tiles". Each tile is composed of 32 antennas and one RFSoC. The signal of the 32 antennas will be amplified by LNAs. Eight of those antenna signals will enter the FDM board. The FDM board will filter the signal in the desired frequency range (300–500 MHz), then upconvert the antennas' signal, finally combining them

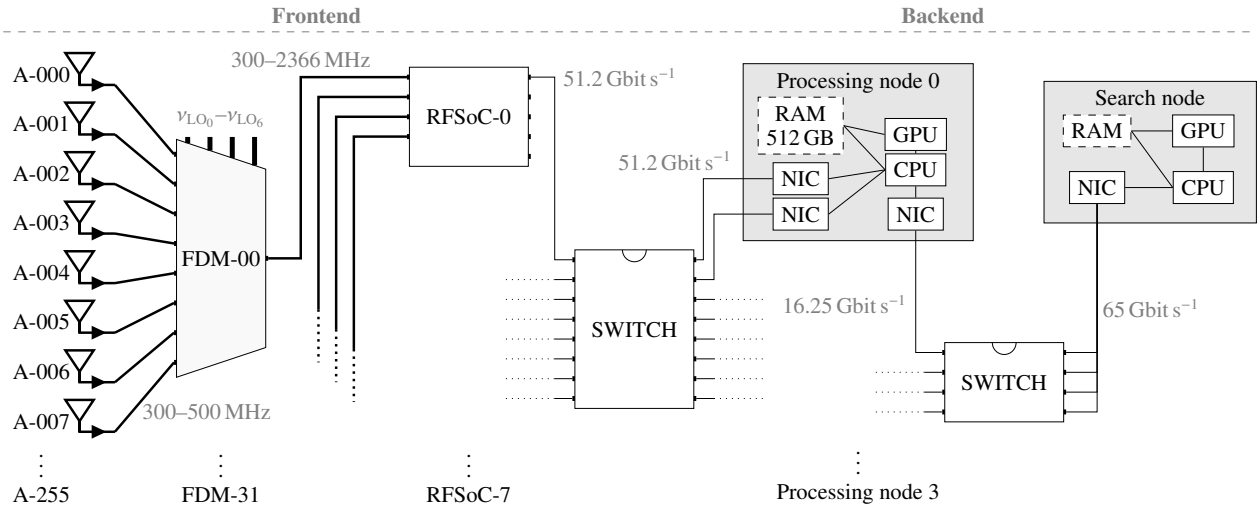

Figure 2.20: General structure of CHARTS, divided in its frontend and backend. The frontend is composed of 256 antennas, 32 FDM boards, 8 RFSoC boards, and a ethernet switch. The backend is separated into the X- and F-engine

in a single output. The signal will then enter the correlator, composed first of an F-engine and then an X-engine. The F-engine will digitize the signal, apply a polyphase filter bank, transform it to the frequency domain, and perform a demux routine. The X-engine will be composed of GPU and CPU nodes. Its primary task will be to receive the incoming flux of data, beamform ~ 1000 beams, multiply (squared), and efficiently downsample the high data rate. One of the nodes is the search node, which will then search for FRB candidates. The analysis node (CPU-based) will classify the detection, and the data will be saved in case of a positive candidate. The CHARTS structure can be observed in fig. 2.20.

2.8 Frequency division multiplexing

The frequency division multiplexing was born in the early 1900s as a multicarrier communication device. In FDM, multiple low-rate signals are transmitted using separate carrier frequencies for each signal. The various carrier frequencies are distributed over the entire channel bandwidth and have to be efficiently separated at the receiver using low-cost filters. The distribution of the frequency carriers can be observed at the top of fig. 2.21. In communication systems, the carriers are generally the users, and the bands between the carriers are called guard bands.

The spectral structure of the FDM leads to some advantages and disadvantages. The empty spectral regions between the carrier frequencies lead to very low spectral efficiency. Still, by breaking up the wide-band channel into several parallel narrower sub-channels, the effect of inter-symbol-interference (ISI) caused due to the frequency selective nature of the channel is greatly mitigated compared to the single channel wideband communication scheme. In the time domain, the same can be explained as a method of achieving high immunity against multipath dispersion since the symbol duration on each sub-channel will be much

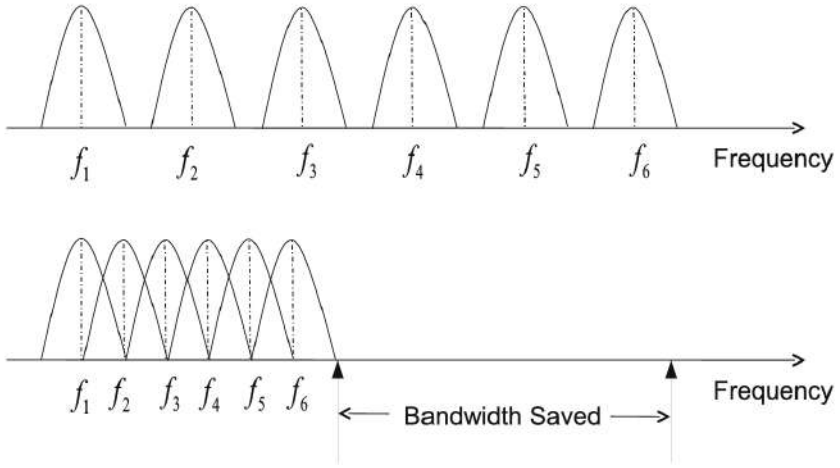

Figure 2.21: Comparison between FDM and OFDM techniques in the frequency domain. Figure extracted from (Narasimhamurthy & Sourour 2010)

larger than the channel time dispersion. Hence, the effects of ISI will be minimized. This gets rid of the need for expensive and complex equalization techniques. But to implement FDM, which yields the benefits mentioned above, a dedicated set of filters and oscillators is needed for each sub-channel, which makes the system expensive and complex to implement (Narasimhamurthy & Sourour 2010).

This FDM technique was replaced by the standard Orthogonal Frequency Division Multiplexing (OFDM) technique. The OFDM takes the incoming data stream and converts them from serial to N parallel data streams, and each parallel data stream is then modulated onto separate carriers using fast Fourier transform (FFT), ensuring orthogonality, as shown in the bottom half of fig. 2.21. The orthogonality property means that when a sub-channel or, in this case, signal, is at its maximum, the other signals are zero. Due to the advancement in digital circuitry, the hardware to implement FFT is fast and inexpensive, making this scheme very attractive. Other advantages of OFDM include high spectral efficiency, avoiding ISI, and equalizers.

Although OFDM offers various advantages compared to the FDM. The project CHARTS can only use FDM for the following reasons:

- The main objective of the FDM board was to properly use the sampling frequency of the RFSoCs 4x2 ADCs. and OFDM requires the signal to be digitized first.
- FDM and OFDM were thought of as communication devices, with low bandwidth signals as users. In CHARTS the signals are astronomical signals with a bandwidth of 200 MHz.
- In the past, techniques like FDM were expensive and complex to implement, but nowadays, the technology of low-frequency RF components has become more accessible and inexpensive.

The FDM board in CHARTS project separates eight signals from the antennas into different “chains”. Those chains have the following frequency ranges: 300–500 MHz, 566–766 MHz,

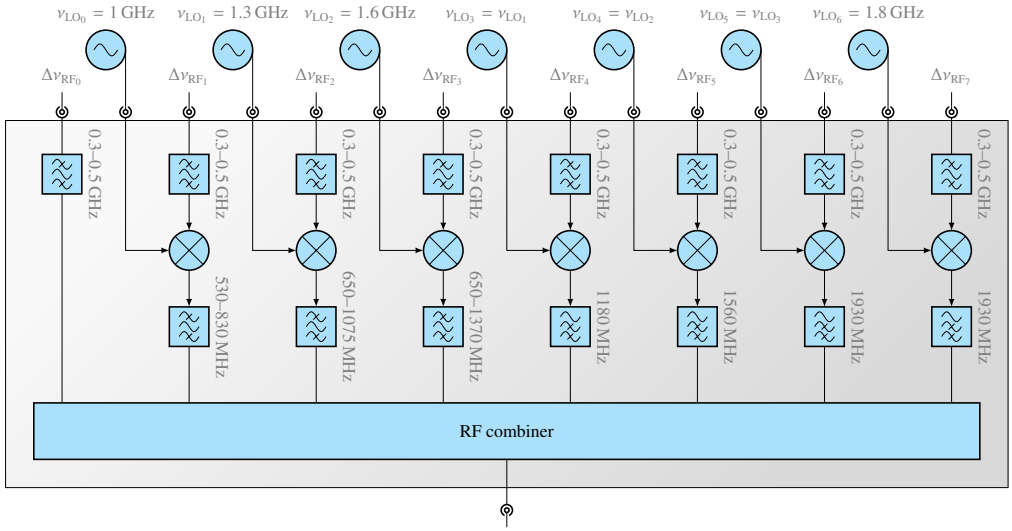

Figure 2.22: General structure of the FDM. The signal coming from each antenna with a passband $\Delta\nu_{\mathrm{RF_i}}$ enters the i chain. A chain is an array of filters and mixers used to select CHARTS frequencies and up-convert them. The mixers are fed with the local oscillators $\nu_{\mathrm{LO_i}}$. Commercial filters with specific ranges will filter the useful signals from the mixers. Finally, the output of each chain is combined in a power combiner.

833–1033 MHz, 1100–1300 MHz, 1366–1566 MHz, 1633–1833 MHz, 1900–2100 MHz, and 2166–2366 MHz. The board was designed to filter the initial signal from 300–500 MHz. After those filters, the signal is mixed with a local oscillator (LO) signal. Those LOs are generated from the RFSoC 4x2 digital-to-analog converters (DACs). The combination of the LOs and the original signal gives the intermediate frequency (IF) signal. This signal, different for all the chains, is filtered again and finally combined with a power combiner. The general structure of the FDM can be observed in fig. 2.22.

2.9 RFSoC 4x2

The RFSoCs 4x2 board is a high-performance computing system optimized for sampling signals at up to 5 GSPS and generating signals at up to 9.85 GSPS. The board was made by RealDigital Digital, but it is based on AMD-Xilinx ZYNQ UltraScale+ Gen3 radio frequency system-on-chip. The board features four 5 GSPS ADCs and two 14-bit, 9.85 GSPS DACs. The board also includes: (Real Digital 2023).

- QSFP28 port for 4x25, 2x50 or 1x100 Gbps Ethernet & 10/100/1000 Ethernet port
- 8 GBytes of 2400 MHz DDR4 (4Gbytes for PS and 4GBytes for PL)
- Ultra-stable, ZCU208 compatible clocking subsystem
- Extensive tutorials and overlays, including spectrum analyzer
- Supported by PYNQ open-source framework with Python & Jupyter notebooks

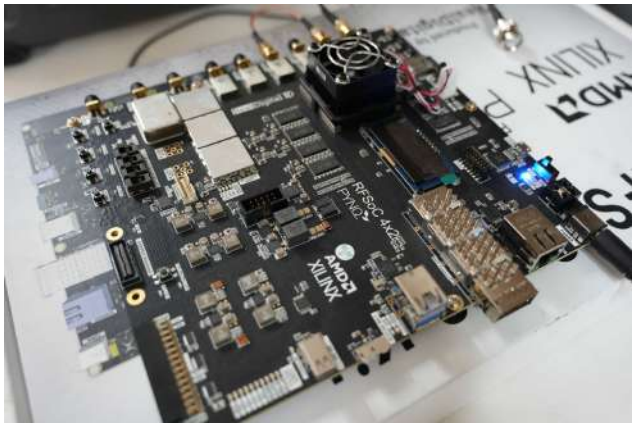

Figure 2.23: One of CHARTS RFSoCs 4x2. The board was used for testing and to generate the LOs.

The RFSoCs from AMD-Xilinx integrates the previously mentioned high-speed ADCs and DACs, a powerful multicore ARM processing system, and a large FPGA. This device is an integrated circuit that can be programmed, and it can also communicate with external elements present in the RFSoCs. FPGAs can be programmed with software like AMD-Xilinx Vitis/Vivado tools, the PYNQ open-source framework, and the graphical programming tool based on Simulink utilizing libraries from the collaboration for astronomy signal processing and electronics research (CASPER) (Collaboration 2023b). CASPER has become the standard in radio astronomy thanks to its powerful FFT and polyphase filter bank tools. However, in the context of the FDM, I used PYNQ. PYNQ is an open-source environment that makes it easier to use AMD-Xilinx platforms. This environment is based on Jupyter Notebook and provides a Python-based interface to load hardware overlays and control the FPGA. PYNQ has more powerful tools to generate simple tones, which are used as the local oscillators that feed the FDM. In the future, we are planning on generating the tones and the rest of the architecture using a compact model with CASPER.

2.9.1 Digital spectrometer noise floor

One relevant aspect in the FDM design is the theoretical SNR of an ADC. The performance of an ADC is determined by the number of bits per sample N. This SNR is calculated as the ratio of the rms signal to the root mean square (rms) quantization noise. The simplified formula for the SNR over the full Nyquist bandwidth (dc to half the sampling frequency) is given by,

$$\text{SNR} = 6.02N + 1.76 \text{ dB}. \tag{2.33}$$

In many applications, the actual signal of interest occupies a smaller bandwidth, BW, which is less than the Nyquist bandwidth. If digital filtering is used to filter out noise components outside the bandwidth BW, then a correction factor (called process gain) must be included in the equation to account for the resulting increase in SNR (Kester 2009),

$$\text{SNR} = 6.02N + 1.76 \text{ dB} + 10 \log_{10} \frac{f_s}{2\text{BW}}, \text{ over the bandwidth BW}. \tag{2.34}$$

The eq. (2.34) can be used to calculate the noise floor in a spectrometer. The spectrometer uses an FFT to convert the time-domain signal to the frequency domain. The FFT noise floor is not the SNR of the ADC, because the FFT acts like an analog spectrum analyzer with a bandwidth of f_s/M, where M is the number of points in the FFT. The theoretical FFT noise floor is therefore $10\log_{10}(M/2)$ dB below the quantization noise floor due to the processing gain of the FFT. The noise floor can be reduced even further by going to larger and larger FFTs; just as an analog spectrum analyzer's noise floor can be reduced by narrowing the bandwidth.

In the case of CHARTS spectrometer, the FFT should be made in the complex mode to properly use the whole 2.5 GHz bandwidth. In the complex mode, the FFT is made with the real and imaginary parts of the signal, so the number of points is not reduced by half. With this consideration eq. (2.34) can be expressed as:

$$\mathrm{SNR} = 6.02N + 1.76\ \mathrm{dB} + 10\log_{10}(M). \tag{2.35}$$

Chapter 3

Design and Characterization of FDM components

In this chapter, I present the overall FDM organization and design. Considering its selected components, design, and characterization. Parts of FDM and measurements were compared with data provided by the manufacturers and RF simulations. The description of simulation software, fabrication methods, and equipment are also provided here. The following chapters will use these methods to fabricate the FDM prototypes.

3.1 FDM architecture and design considerations

This section describes the structure of the FDM, the type of components used inside the board, and the constraints of the FDM board. The FDM design and structure were given by CHARTS specifications and the exposure to FRB sky properties. These constrains and specifications may change based on CHARTS backend design; however, the principal considerations that the FDM design was based on were:

- The selected digitizer is an RFSoC 4x2 board. This board has four ADCs with a sampling rate of five GHz. This means the FDM board has an available total bandwidth of 2.5 GHz per ADC, following the Nyquist–Shannon sampling theorem (Shannon 1949).
- CHARTS is an array of 256 antennas; each antenna was designed to work in a bandwidth of 200 MHz. This value plus the available bandwidth of 2.5 GHz can give us the maximum number of input signals in the FDM.
- The data of the FDM will be digitized and transformed to the frequency domain using FFT methods. The number of bits and frequency bins in the FFT will specify the noise floor of CHARTS. The losses inside the FDM board should be low enough to detect FRBs above that noise floor (sky and receiver chain).
- CHARTS receiver temperature is mainly influenced by the first-stage amplifier (Fouquet 2020). However, the FDM can also increase the temperature of the system. The

Table 3.1: FDM chains and LO frequencies

Chain	Range MHz	LO MHz	Band
0	300-500	None	Original
1	566-766	1066	LSB
2	833-1033	1333	LSB
3	1100-1300	1600	LSB
4	1366-1566	1066	USB
5	1633-1833	1333	USB
6	1900-2100	1600	USB
7	2166-2366	1866	USB

maximum temperature of the receiver should be $< 50\,\mathrm{K}$.

- The coupling of the antenna signals inside the FDM should be minimized. If one signal overlaps with the frequency of another antenna, it will contaminate the signal with unwanted RFI. Simulations of the current CHARTS antennas show a coupling level of -15–$-20\,\mathrm{dB}$ between two antennas, so the internal coupling of the FDM should not exceed $-20\,\mathrm{dB}$.
- The LOs and the RF should not affect the signals of the antennas once multiplexed. To achieve this, mixers with port isolations of at least $20\,\mathrm{dB}$ were selected.

3.1.1 FDM architecture

Following the previous considerations, the FDM was designed to admit eight input signals. Each signal will enter an RF channel called a "chain", which has a similar structure to a heterodyne radio frequency receiver. This means it follows the structure of a bandpass filter, a mixer, and an IF bandpass filter. The signal of every chain, except chain zero, will be frequency converted to one of eight chain passbands, listed in table 3.1. The new IF bands are filtered and combined in an eight-way power combiner, as shown in fig. 2.22.

The use of amplifiers within the FDM was discarded early on. Their inclusion would increase the complexity of the board, and a weighted analyses on the mixers and filters were preferred in earlier iterations. Instead of using amplifiers in the FDM architecture, the solution was to include a separate LNAs to amplify the signals of each antenna and, if necessary, a final amplifier after the FDM output.

The frequency separation of each chain was designed to be approximately equal among them. The LOs dictated the separation of the different frequency bands; they were selected, so the separation among each chain was approximately $66\,\mathrm{MHz}$. Also, the selected LOs were placed outside the bandwidths of the chains; this way, the signal of the LO does not contaminate the desired signals.

We can repeat some LOs with the configuration of table 3.1, saving the need for multiple signal generators. On the other hand, the constant separation among chains means that the designs of the initial bandpass filters can be reused among chains. Lower side band

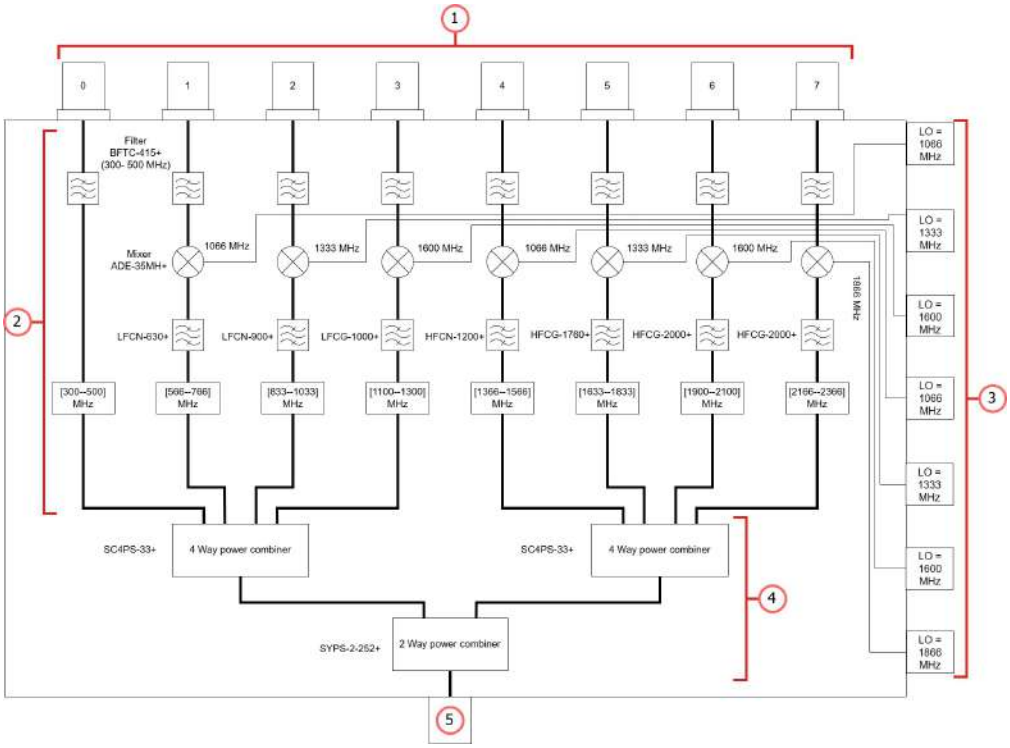

Figure 3.1: FDM diagram with commercial components. The numbers represent different parts of the FDM board. (1) are the eight inputs that come from the antennas, (2) is the structure of a chain it is here where the frequency shift is made, (3) are the local oscillators generated by the RFSoC4x2 DACs, (4) are the power combiners the ones responsible of combining the eight chain signals, and (5) is the single output of the FDM were all the signals were combined this combined signals goes to the digitizers ADC.

(LSB) means that the image with the lowest frequency is selected after the frequency is shifted. Typically, this lower sideband will be inverted, so the signal needs to be flipped once digitized. Upper side band (USB) represents the image with the highest frequency; this band will be identical to the original signal. Chains that use the same LO will select either the LSB or the USB, and the other band should be filtered appropriately because it can contaminate the other chain's signals.

The first FDM design was made with commercial components in mind. These elements were selected from radio frequency manufacturers and suppliers, such as Minicircuits (Mini-Circuits 2023c) and Mouser Electronics (Electronics 2023). The selection of each component was made based on CHARTS 300–500 MHz frequency range, the cut-off frequencies of each filter to select the correct IF band, and the working range of the combiners. As the commercial components were not made precisely according to the FDM specifications, the closest ones in parameters were selected. In the case of the IF bandpass filters, there were no exact options for each chain; therefore, low-pass and high-pass filters were selected depending on the chain. No eight-way combiners with a wide bandwidth working between 0–2.5 GHz were found, so two 4-way combiners and a 2-way combiner were chosen. All those components were added to the design of the FDM as shown in fig. 3.1.

In later FDM versions, it was decided to add new alternative parts and custom components

to the design. The main reason for this was to improve the response of each chain to reduce the coupling and to satisfy the new needs of CHARTS project with the addition of differential antennas. The main change in components was the inclusion of differential mixers, and custom bandpass filters from 300–500 MHz.

3.1.2 Design constraints

The principal constraints in the FDM design can be divided into two: the expected overall temperature of the receiver and the digitizer parameters. The receiver's temperature will dictate if the system is sensitive to FRBs. Meanwhile, the digitizer will dictate the noise floor of the system.

Digitizer restrictions

Equation (2.35) describes the noise floor in a digital spectrometer. This noise floor is dependent on the ADC number of bits per sample n_{bits} and the number of FFT channels N_{ch}. The value of n_{bits} is given by the manufacturer of the RFSoC 4x2 board, with a value of 14 bits. Meanwhile, the number of FFT channels is given by CHARTS spectrometer; this value was set at 8192 channels. Considering the previous specifications, the noise floor of the spectrometer is -128.18 dBm. Nevertheless, the digital design considers processes like decimation and internal filters that change the value of bits per sample. To have an upper bound restriction, the value of $n_{\text{bits}} = 8$ bit was used. With the previous value, it gives that the noise floor of the digitizer will be -89.05 dBm, or in other words, that is the minimum signal that the digitizer can detect.

The sampling rate and the number of FFT channels will also dictate the maximum delay that the FDM can have in each chain. This sampling rate corresponds to a sampling period of 0.2 ns. The samples are processed in groups of 16 384 (or 8192 frequency channels), wich means that one spectra is produced every $16384 * 0.2\,\text{ns} =\sim 3.3\,\mu\text{s}$. The delays of the FDM cannot be higher than 3.3 µs, because if one antenna signal arrives (relative to another antenna) after that value it will mean that the signal is not in the same spectra, making them incoherent.

Receiver restrictions

A pre-amplifier can be added in the analysis to obtain the maximum FDM losses that can be added in the receiver, so the noise power is higher than the noise floor of the digitizer. The simplified diagram of the receiver is shown in fig. 3.2, where an LNA with 50 dB gain was considered in the analysis. The input signal of the antenna can be approximated as a load of room temperature 290 K, and bandwidth of 200 MHz. Using eq. (2.18), we obtain,

$$\text{RF}_{\text{power}}\text{dBm} = 10\log_{10}(kTB \cdot 1000) = -91\,\text{dBm}. \tag{3.1}$$

Assuming the simplified receiver shown in fig. 3.2, and accounting for the cable losses

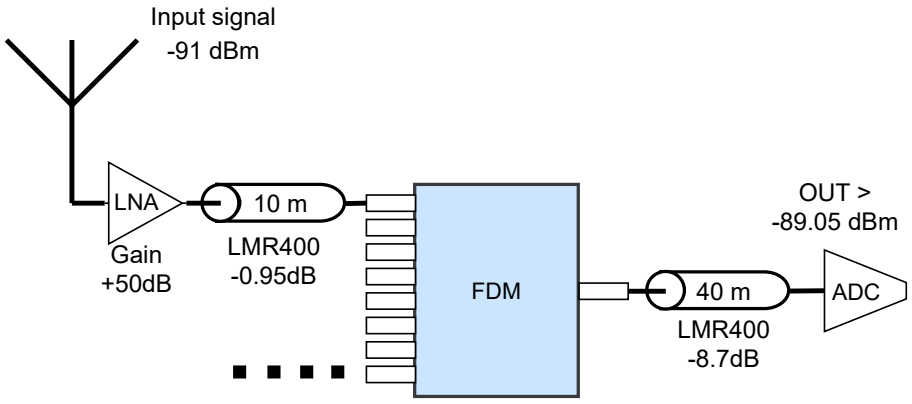

Figure 3.2: Simplified CHARTS receiver path. The power of the receiver's output signal should be higher than the noise floor of the internal RFSoC 4x2 spectrometer. The diagram considers the noise power received on the antenna, the gain of a generic LNA, the losses on the LMR400 cables, and the FDM with unknown losses or gain.

before and after the FDM, the maximum allowable loss of the FDM is 38.4 dB. Above this value, the amplification of the LNA will not be sufficient to detect a signal. This rough approximation takes into consideration the length and type of the cables, which have different losses depending on the frequency. In the case of the LMR400 cable, the loss at 500 MHz was -0.95 dB for 10 m, while the FDM output is separated by 40 m and has a loss of -8.7 dB at the highest frequency, 2366 MHz.

To calculate the maximum allowable FDM noise temperature such that the constraint $T_\mathrm{r} < 50\,\mathrm{K}$ is satisfied, with T_r the receiver noise temperature, we can use eq. (2.24). The cascade consists of the LNA, a 10 m cable, the FDM, and a 40 m cable. The LNA retains its previous characteristics: a gain of 50 dB and a noise temperature of 20 K. The cables also maintain their prior values, with loss factors of $L_{C1} = 0.95$ dB and $L_{C2} = 8.7$ dB for cable 1 and cable 2, respectively. The corresponding noise temperatures, T_{C1} and T_{C2}, are calculated using eq. (2.20).

The FDM is modeled as a black box with unknown loss factor L_FDM and noise temperature T_FDM. As both variables are unknown, we explore different values of FDM loss and, for each, get the maximum noise temperature that satisfies the system constraint. Based on the parameters above, we obtain the following inequality,

$$T_\mathrm{r} = T_\mathrm{LNA} + \frac{T_{C1}}{G_\mathrm{LNA}} + \frac{T_\mathrm{FDM} L_{C1}}{G_\mathrm{LNA}} + \frac{T_{C2} L_{C1} L_{FDM}}{G_\mathrm{LNA}} < 50\,\mathrm{K}, \tag{3.2}$$

By isolating T_FDM and using a range of FDM loss factors, we compute the maximum allowable FDM noise temperature that satisfies the condition $T_\mathrm{r} < 50$ K. Some combinations result in unphysical values (i.e., $T_\mathrm{FDM} < 0$ K), as shown in fig. 3.3. The case, where $T_\mathrm{FDM} = 0$ K, corresponds to the maximum permissible loss factor of $L_\mathrm{FDM} = 31.12$ dB. This sets the upper bound for the FDM loss to ensure the receiver temperature remains below 50 K.

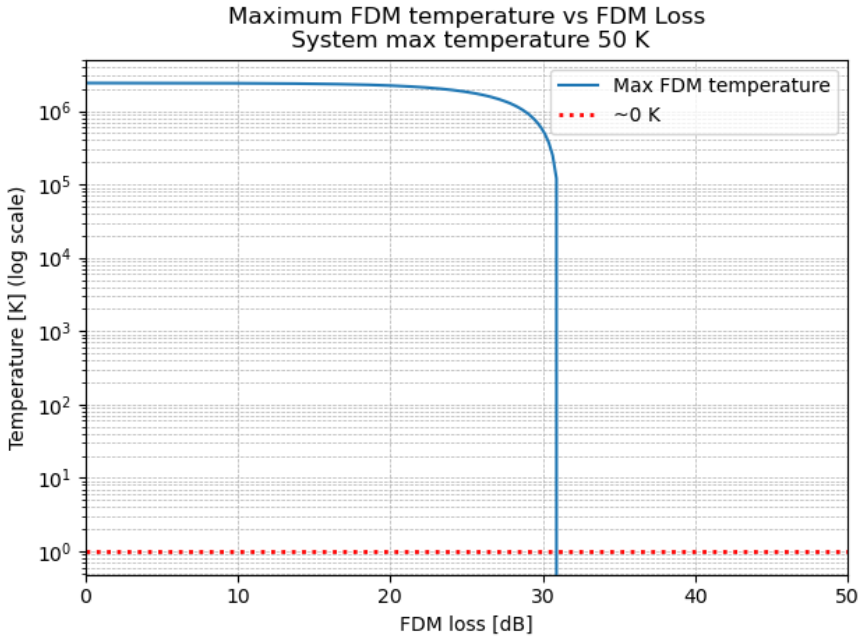

Figure 3.3: Maximum FDM temperature as a function of board losses required to have a receiver temperature of 50 K. The red line marks the 0 K temperature, which gives the restriction for the maximum loss of the FDM board at 31.12 dB.

3.2 Overview of Key Components

As previously mentioned, the FDM design was based on commercial components for its prototypes and a new commercial mixer and custom bandpass filter for the later differential design. This section will review the selected FDM components listed in table 3.2. The analysis will primarily focus on the bandpass filters (commercial and custom), the two mixers, the four-way combiner, and the two-way combiner.

3.2.1 Mixers

The first selected mixer is the ADE-35MH+. This model is a double-balance mixer, which means it has good RF-IF and LO-IF isolations. In this case, manufacturers do not provide mixer parameters for the specific RF and LO FDM signals because these parameters depend on specific RF and LO frequency combinations. Typical values were used while choosing this mixer; these specifications are listed on 3.3.

The input and output frequency range worked for CHARTS and the FDM range. The conversion losses, although high, were compensated by the good port isolation values. These isolation values helped the system become less dependent on precise IF bandpass filters. The input signals are expected to be below the 1dB compression and TOIP values, so the linear range of the mixer is maintained. Finally, the required LO power is too high to be generated by the RFSoC 4x2, but the LOs can be easily amplified before entering the mixer to achieve 10 dBm.

Table 3.2: List of commercial FDM components

Name	Description	Chain	Cite
BFTC-415+	Bandpass filter 300–500 MHz	0–7	(Mini-Circuits 2023d)
ADE-35MH	Mixer	1–7	(Mini-Circuits 2023e)
MAX2673	Differential mixer	1–7	(Devices 2023)
LFCN-630+	Low pass filter	1	(Mini-Circuits 2023f)
LFCN-900+	Low pass filter	2	(Mini-Circuits 2023g)
LFCG-1000+	Low pass filter	3	(Mini-Circuits 2023h)
HFCN-1200+	High pass filter	4	(Mini-Circuits 2023i)
HFCG-1760+	High pass filter	5	(Mini-Circuits 2023j)
HFCG-2000+	High pass filter	6–7	(Mini-Circuits 2023k)
NCS2-771+	1:2 balun	0	(Mini-Circuits 2023l)
SC4PS-33+	4 way power combiner	0–7	(Mini-Circuits 2023m)
SYPS-2-252+	2 way power combiner	0–7	(Mini-Circuits 2023n)

Table 3.3: Typical values of mixer parameters given by the manufacturers of ADE-35MH and MAX2673. Some specifications are not characterized for CHARTS range and LOs, so the final values may change.

Parameter	ADE-35MH+	MAX2673
RF frequecy range	3–3500 MHz	40–500 MHz
IF frequency range	5–2500 MHz	400–2500 MHz
Conversion Loss/gain	−6.9 dB	+8.6 dB
RF-IF isolation	25 dB	–
LO-IF isolation	28 dB	26.6 dB
1dB compresion	+8 dBm	−8.3 dBm
TOIP	+18 dBm	4.5 dBm
LO power	10–16 dBm	−10–5 dBm
Noise figure	6.9 dB	10.4 dB

The differential mixer MAX2673 was selected after the inclusion of differential antennas in the CHARTS project. This mixer is a miniature, low-cost, low-noise, and double-balanced upconverter mixer. The model was made for portable devices, and its structure is equipped with internal amplification on the RF input signal and the LO. This means that this mixer has conversion gain instead of conversion losses. The amplification on the LO will help the system to use a lower power LO signal compared with other mixers. The parameters specified by the manufacturer are shown in table 3.3.

The parameters satisfy CHARTS requirements in the frequency ranges. The conversion gain of the mixer helps the signal to be amplified above the spectrometer noise floor. The noise figure, on the other hand, could be problematic, but again, the FDM is one of the last elements on the RF chain of CHARTS, so the amount of noise that the mixer will add to the system may be neglected. The LO-IF isolation is not as good as the ADE-35MH+ model, but the LOs were designed not to interfere with the IF signals. On the other hand, the RF-IF isolation was not specified by the manufacturer and was tested before the implementation on the FDM. The TOIP and 1dB are slightly worse than ADE-35MH+, but as CHARTS does

not expect to surpass those values with low-power astronomical signals.

3.2.2 Bandpass filters

The bandpass filter BFTC-415 has a pass band of 330–500 MHz, with typical insertion losses of 4 dB on this pass band. The range does not align precisely with the frequency range of CHARTS. Moreover, its insertion losses in 300 MHz are 6.6 dB. This value is not optimal, but as the only commercial bandpass filter that worked near the CHARTS range, it was a good component for prototyping. Also, as the gain from amplifiers is higher in low frequencies, the insertion losses in the filter work similarly to an equalizer at 300 MHz.

After the prototyping phase of the FDM, it was decided to design a bandpass filter. This custom bandpass filter was made to address the problems of the BFTC-415 filter. The filter was initially developed using online filter design tools (Microwave 2023), and later simulated and improved in AWR schematic (Systems 2023). The simulations were made with real component parameters and adjusted based on the cut-off frequencies of the filter. The filter was designed with LC components; it is a sixth-order filter to reduce the coupling between chains, and it has a pass band of 300–500 MHz.

3.2.3 Combiners SC4PS-33+ and SYPS-2-252+

There were not many commercial power combiners that worked on the FDM range. The other commercial options were resistive combiners with high losses or poor port isolations. SC4PS-33+ and SYPS-2-252+ were the best available options; they are core and wire power combiners with typical port isolations of 17 and 18 dB, respectively.

3.3 Design and simulation of testing PCBs

The components are typically designed to operate under specific conditions related to the PCB configuration (e.g., number of layers, dielectric thickness, and material). If these conditions differ, the parameters of the component may deviate from the typical values provided by the manufacturers. This is of special interest in the case of mixers where the values provided by the manufacturer are not always accurate for the FDM frequencies specifications, and the case of the custom bandpass filter. For this reason, different testing PCBs were developed to test the components. The selected components are surface mounted technology (SMT), which means they are soldered on the surface of the PCB. Six testing boards were designed for each of the components described in the previous section to test these components and verify the data provided by the manufacturer.

This section will describe the design and assembly of the six testings PCBs. Three steps were accounted for in the construction process: The simulation of the testing PCBs, the design of the testing boards, and the fabrication and assembly of the components.

(a) LPKF laser machine.

(b) LPKF mechanical machine.

Figure 3.4: Two LPKF machines were used to print PCB boards to test the FDM components and prototypes. Figure 3.4(a) is the laser machine used to print the transmission lines and the overall structure of the FDM. Figure 3.4(b) is the mechanical machine used to drill vias and cut the PCB.

3.3.1 Transmission line design

The design and simulation should consider the material and the proportions of the substrate. These parameters dictate the structure of the transmission line that is connected to the component. The other important delimiter in the PCB design is the manufacturer of the PCB. In this thesis, there were two ways of printing FDM prototypes and testing circuits: Using the LPKF PCB printing machine of the MWL and sending the schematic to a PCB manufacturer. The LPKF machine shown in fig. 3.4 was used mainly for FDM prototypes and testing components. For more complex boards, they were sent to JLCPCB (2023a); this manufacturer has different PCB substrates and the number of layers that were key to building more complex designs.

The available PCB material on the MWL was the substrate FR4, with a tickness of 1.55 mm and conductor thickness of 35 µm. Two types of transmission lines were considered in the designs: microstrip lines and grounded coplanar waveguides. The parameters of the transmission lines were calculated using the AWR TXline tool shown in fig. 3.5. This tool uses the same equations 2.8 and 2.10 to calculate the characteristic impedance of the line; the same can be made by fixing the characteristic impedance in the standard value of 50 Ω and obtaining the transmission line values. These parameters are shown in table 3.4

All the parameters were calculated for a central frequency of 400 MHz, and the dielectric constant was assumed to be around 4.38. A CPW line was added to the list of parameters because the software AWR does not support GCPW simulations, so CPW lines were used instead. For the testing PCBs, it was finally decided to use GCPW instead of microstrip lines, mostly because the width of the microstrip line was too big compared with the connection of some commercial components. GCPW lines also help to ground components more easily.

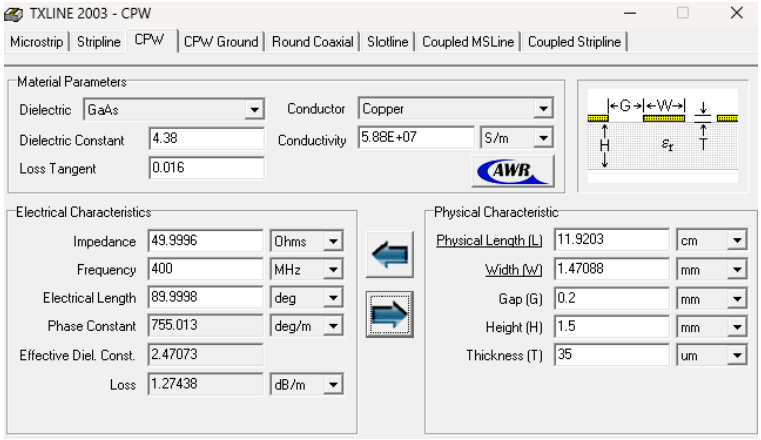

Figure 3.5: TXline tool from AWR. In this figure, the width of a CPW is calculated to obtain a characteristic impedance of 50 Ω. Parameters like the height, thickness, and dielectric constant depend on the PCB material available in the laboratory.

Table 3.4: Parameters for different types of transmission lines

Parameter	Microstrip line	GCPW	CPW
Dielectric Constant	4.38	4.38	4.38
Line width (mm)	2.93722	1.10594	1.46414
Gap (mm)	-	0.2	0.2
Height (mm)	1.55	1.55	1.55
Thickness (um)	35	35	35

3.3.2 Simulation of the testing PCBs

The simulation of the FDM components was made using the AWR software. Two types of simulations were made depending on the type of component. The first type of simulation was for passive components (i.e., filters and combiners); these simulations were made with the AWR schematic tool. Meanwhile, simulations for the mixers were made with the AWR VSS tool.

The AWR schematic simulations considered the CPW lines connected from the Sub-Miniature version A (SMA) connectors to the components. Parameters such as the width and properties of the CPW lines were taken from the previous calculations. The length of the lines was made in parallel with the PCB design to realistically locate the components on the board. The CPW lines were connected to the SMA connectors and the component using SMT pads, which are the pads used to solder the components to the PCB. Values such as the width and length of the pads were obtained from the manufacturer-recommended layout. Finally, the component was treated like an N-network, which means that the S parameters were imported from the manufacturer. An example of an AWR schematic is shown in fig. 3.6.

The VSS simulations were used mostly to simulate the mixers and FDM boards. The VSS simulations were used to obtain the frequency spectrum power of the output signal, like the data obtained from a spectrum analyzer. The input of this type of simulation was a tone sweep from 200–600 MHz. The characteristics of the input signal were modifiable, so values

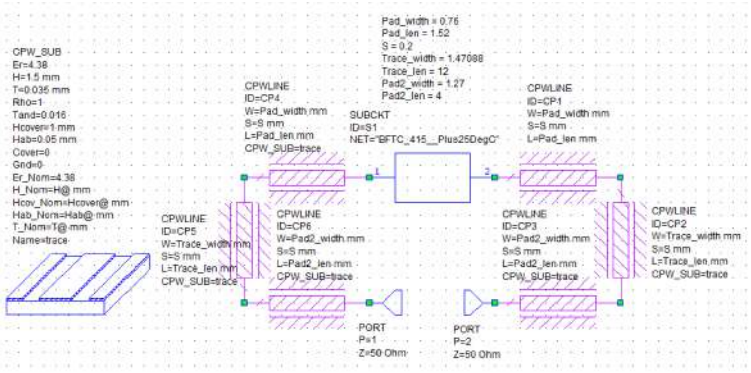

Figure 3.6: BFTC-415 bandpass filter simulation using a CPW as the transmission line. The simulations were made in the AWR schematic tool. The element marked as SUBCKT is a block containing the S parameters of BFTC-415. CPW_SUB is the element that gives the substrate values to all the CPWLINE elements of the simulation. The CPWLINE elements near the bandpass filter and the ports are the SMT pads that are used to solder the filter and connectors to the PCB. The other two CPWLINE elements are the transmission lines that connect the SMA connectors with the bandpass filter.

like the input power and the frequency range could be changed. The option to generate single tones was also possible; with this tool, the LOs of the FDM were generated. An example of the VSS simulation is shown in fig. 3.7.

The mixer model in VSS has the option of customizing different values such as port isolations, noise figure, TOIP, and conversion losses. All the previous parameters were extracted from the typical values provided by the manufacturer, except for the conversion losses. For conversion losses, a bandpass filter with equal losses per frequency as the mixer was added before the mixer model. The insertion losses in the GCPW were simulated as attenuators with an intermediate value of 0.05 dB losses. The LO was selected as 1066 MHz which is the first FDM LO with a power of 13 dBm. Finally, the input signal was set at power 0 dBm; this way, we can observe the actual conversion losses.

The case of the components used for the differential antenna, MAX2673, and custom filter was simulated on VSS and schematic, respectively. For the two components, it was decided to use a microstrip line instead of a GCPW line to easily implement the LC components into the design. The addition of LC components into the mixer structure was necessary because the impedance on the mixer output was not matched to 50 Ω. The impedance matching was done with a different L-network per chain using AWR optimizer, with the help of the University of Toronto (UofT) team. The rest of the components were selected from the typical impedance matching values of the manufacturer. On the other hand, the custom bandpass filter was designed with LC components. The parameters of these components were obtained from commercial components from Murata Manufacturing (Manufacturing 2023), so the simulations better resemble the real parameters of the filter. The AWR simulation of the custom bandpass filter is shown in fig. 3.8.

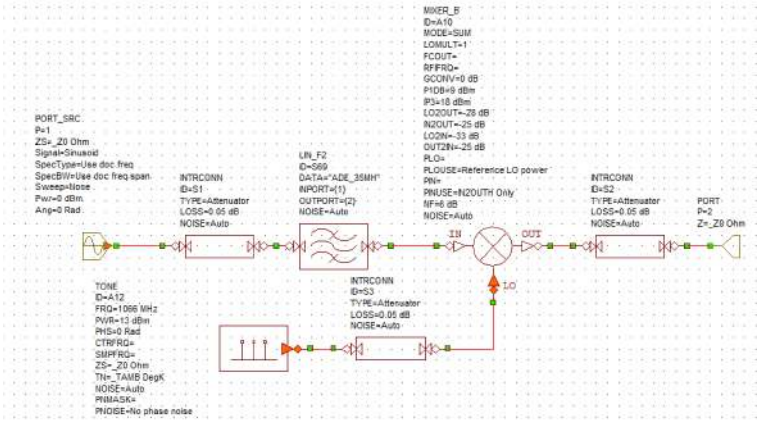

Figure 3.7: ADE-35MH mixer testing PCB simulation in AWR VSS. The simulation represents chain 1 of the FDM, with an LO frequency of 1066 MHz. The input signal is a tone sweep from 200 MHz to 600 MHz. The parameters of the mixer were obtained from the manufacturer, and its conversion losses were interpreted as a bandpass filter with the same losses.

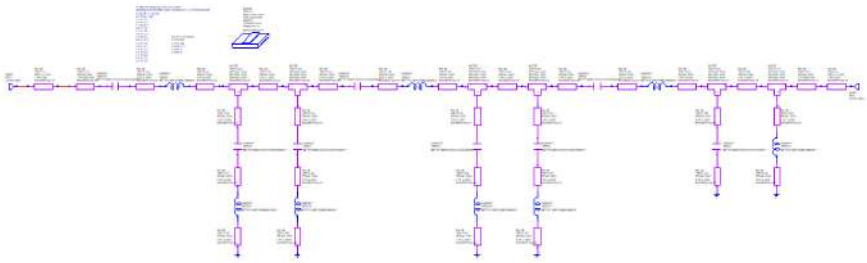

Figure 3.8: Custom bandpass filter simulation in AWR. The bandpass filter was designed with LC components whose parameters were obtained from Murata Manufacturing (Manufacturing 2023) to better resemble the real behavior of the filter.

3.3.3 PCB design and fabrication

All the testing boards were designed using KiCad software and were based on the manufacturer's recommended layouts. Different variations were made in case the used transmission line did not match the conditions assumed in those reference designs. The first PCBs were designed with the LPKF restrictions in mind. With these parameters, it was decided to use the CPW line values of table 3.4 and a diameter of the vias of 0.6 mm. The vias were used to connect the ground of the top and bottom layers. The PCB designed and manufactured with the LPKF machine were the bandpass filter BFTC-415 and the mixer ADE-35MH. The components and vias were soldered on the MWL mechanical laboratory, and the final testing PCBs are shown in fig. 3.9.

The combiner testing PCBs were designed after the components were added and tested into the first FDM prototypes. The losses of the board were higher than expected, leading to the suspicion that the combiners were not working as expected. The main problem was detected in the type of PCB material used for the prototype and the suggested combiners material. The suggested PCB mounting of the two-way and four-way combiners was a configuration of a substrate of Rogers RO4350B and a thickness of 0.762 mm. Meanwhile, the

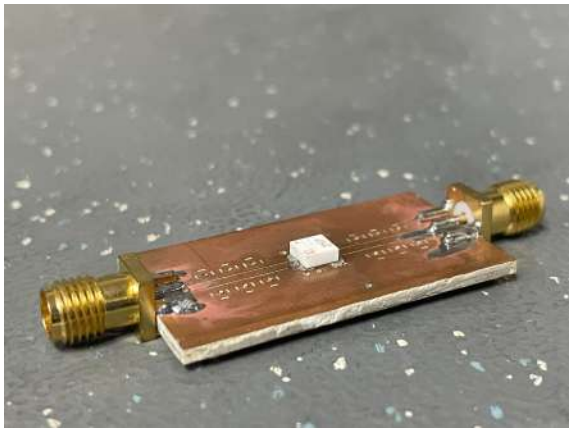

(a) Fabricated BFTC-415 testing board.

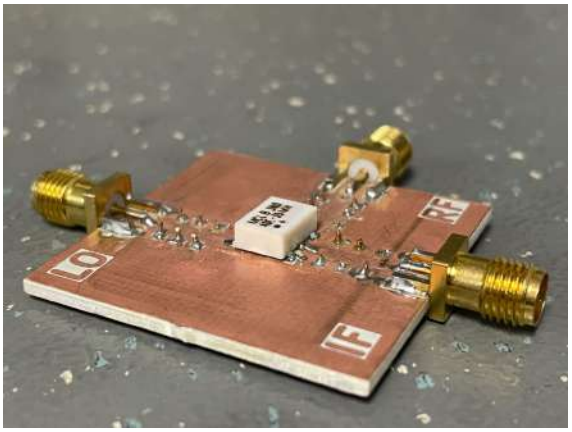

(b) Fabricated ADE-35MH testing board.

Figure 3.9: Testing PCBs fabricated with the LPKF machine. The PCB of the bandpass filter is shown in 3.9(a), and the PCB of the mixer is shown in 3.9(b). Both PCBs were fabricated in the MWL laboratory.

combiners were tested on a PCB of FR4 with a thickness of 0.21 mm. This difference led to an impedance mismatch that caused the losses of the combiners. To solve the problem, four testing PCBs were designed: a two-way combiner PCB with two layers, a two-way combiner PCB with four layers, a four-way combiner PCB with two layers, and a four-way combiner PCB with four layers. The difference in layers changes the thickness of the substrate, changing the behavior of the combiners. The designs were made in KiCad and sent to JLCPCB for fabrication. The final testing PCBs are shown in fig. 3.10.

The PCBs of the MAX2673 and the custom bandpass filter were also fabricated with JLCPCB. Two PCB designs were made in KiCad for the filter: one for a single bandpass filter, and two parallel bandpass filters. This bandpass filter was primarily developed for the differential FDM, so in the FDM, two parallel bandpass filters will be located before the differential mixer. To characterize the coupling among filters, the parallel filter PCB was fabricated.

3.4 Testing methodology for components

The instruments used to measure the testing board of the mixer, the filters, and the combiners were different. In the case of the bandpass filter and combiners, a vector network analyzer (VNA) was used to measure the S parameters of the network. This VNA generates a signal, and it measures the reflections and transmission depending on what is being measured, S_{11} or S_{21}. The testing measurement of the mixer can not be made with a VNA. This is because the VNA reads the response of the same frequency that is generating the input signal, and then it makes a sweep for all the frequencies selected previously. Instead of a VNA, we can use a spectrum analyzer to read its response of different RF and LO combinations. To generate the LO, signal generators were used. The setup is shown in fig. 3.11.

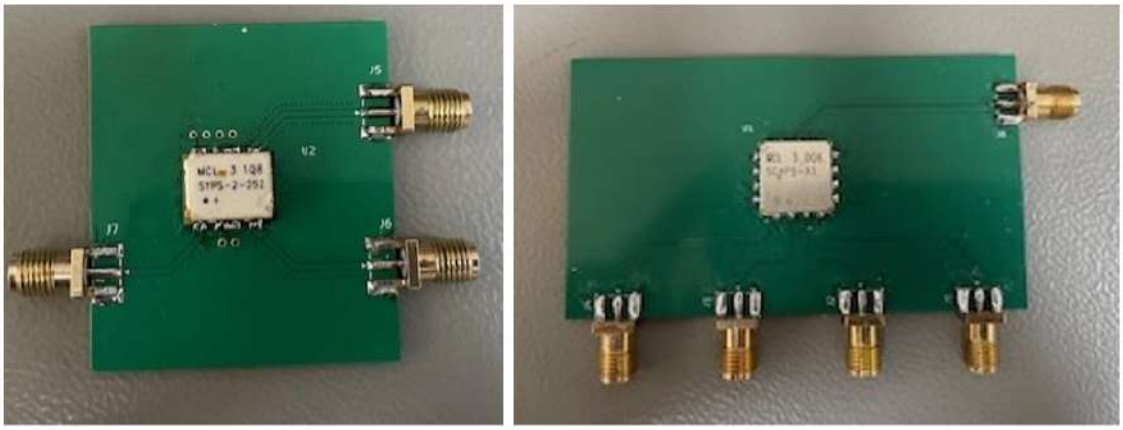

Figure 3.10: Testing PCBs of the combiners fabricated by JLCPCB. The PCB of the two-way combiner is shown on the left, and the PCB of the four-way combiner is on the right. Two similar designs were made with a four-layer board to test the behavior of the combiners once included in the FDM design.

The testing of the mixer ADE-35MH uses two signal generators, one for the local oscillator and the other for the input RF signal. A spectrum analyzer reads the IF signal and the rest of the spurious signals. With the previously described setup, two tests were run for the mixer: an input frequency sweep and a variation in LO power. The input frequency sweep was made with a LO of 10 dBm and the frequency changed depending on the chain that was going to be measured. The input power was generated with one of the RFSoC 4x2 DACs with a maximum power at 400 MHz of −1.92 dBm. The input was shifted from 300 MHz to 500 MHz. The spectrum analyzer was set in the max hold option to read all the data of the sweep simultaneously.

The tests on MAX2673 were similar to the ADE-35MH, but the parameters of the LO and RF powers were maintained low to not saturate the internal amplifiers of the mixer. The LO was set to −10 dBm and the RF was set to −17.4 dBm at 400 MHz. Another measurement was made for this mixer; it was a test of the minimum voltage at which the mixer works.

3.5 Comparison of simulations and experimental results

In this section, the results of the measurements and simulations of the testing PCBs are shown and compared. An analysis of the behavior of the components was also made to decide if the components are adequate for the FDM. The results were separated into the filters, mixers, and combiners.

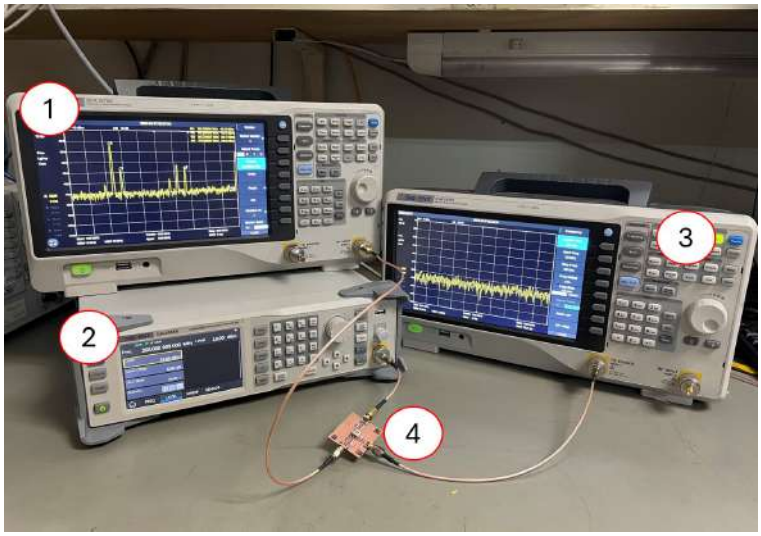

Figure 3.11: Testing setup of the mixer. Two signal generators are used to generate the LO and RF signals. In this picture, the Siglent spectrum analyzer that reads the IF signal is marked as (1). (2) is the signal generator that gives the LO signal. (3) is the other signal generator, which in this case is also a Siglent spectrum analyzer. Finally (4) is the mixer testing board.

3.5.1 Bandpass filter results

The comparisons of the bandpass filter are shown in fig. 3.12. The plot shows the comparison between the real PCB and the simulations. The results are similar in both cases of the BFTC-415 and the custom bandpass filter. The main difference is the sharpness of the filter. It is observed in the gray rectangles that represent chain zero and one of the FDM that the custom bandpass filter has a better rejection on chain one. This means that the coupling among chains is lower compared with BFTC-415, where the losses are only 20 dB on chain one. The sharpness of the filter also helps in the reduction of coupling of all the other chains, improving the response of the FDM.

The custom filter results were highly dependent on the soldering of the components. Multiple iterations of the filter were made on the LPKF machine; if the soldering was not optimal, the results varied considerably. It is of great importance to have the components soldered by a professional manufacturer. If that is not the case, the behaviour between filters inside the FDM may vary, making the system less reliable when characterizing the complete CHARTS receiver.

3.5.2 Mixers results

As explained before, three types of ADE-35MH measurements were made. The first measurement was the RF frequency sweep; these measurements are shown in fig. 3.13. The response shows the comparison between simulations and measurements of the mixer of the chains that share their respective LOs of table 3.1. It is observed that in all measurements, the isolation of the RF port to the IF port is lower than expected, meaning that the RF

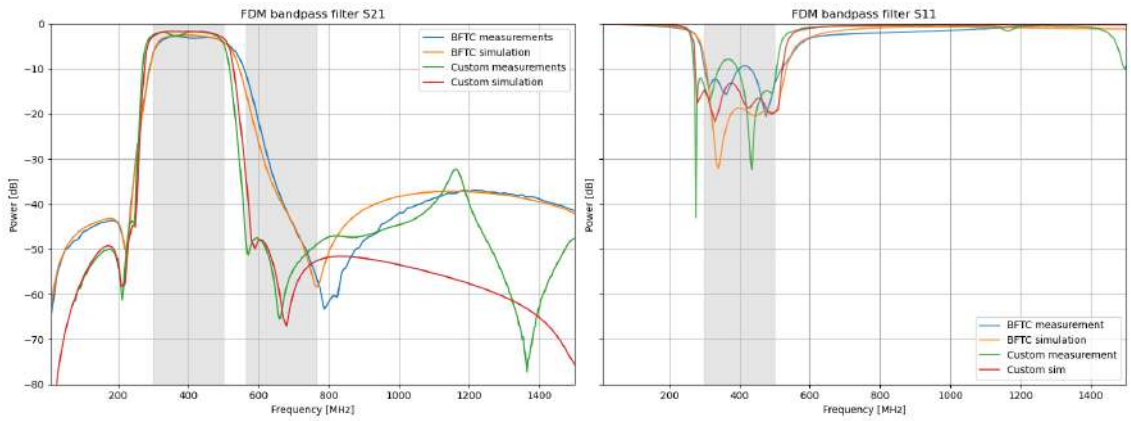

Figure 3.12: BFTC-415 and custom bandpass filter measurements vs simulations. In the figure on the left, the insertion losses are shown for the BFTC415, its simulation, the custom filter measurement, and its simulation. On the right, the return losses are shown for the same measurements and simulations. The bands of chain zero and chain one are marked with gray rectangles to visualize how the filter affects the coupling among chains.

Table 3.5: LO Power, conversion loss, LO-IF isolation, and RF-IF isolation for the ADE-35MH mixer. The input RF signal was a tone in 400 MHz with a power of −1.9 dBm. The LO frequency was 1066 MHz.

LO Power (dBm)	**Conv. Loss (dB)**	**LO-IF Isol. (dB)**	**RF-IF Isol. (dB)**
1	12.62	39.5	25.2
3	10.6	35.7	25.4
5	9.47	31.7	25.4
7	8.72	29.16	25.6
9	8.22	27.3	26.0
11	7.88	25.8	26.6
13	7.66	24.7	27.1
15	7.5	23.9	27.5

signal can contaminate the IF signal. This is a problem that can be addressed by adding more filters in the FDM. The conversion losses are slightly higher than the datasheet. The losses became higher in chains with higher frequencies; this can be attributed to the loss in the cables, bad impedance matching, or the soldering of the components. Finally, the LO-IF isolation is similar to the datasheet.

The second type of measurement was a power variation on the LO power to detect its optimal value. The results are shown in table 3.5. The conversion losses and RF-IF isolation were calculated reading the spectrum analyzer output power in 666 MHz and 400 MHz respectively, then the values were subtracted by the power of the RF signal. The LO-IF isolation was calculated by reading the power in 1066 MHz and subtracting the current LO power.

As seen in table 3.5, the mixer works even at LO powers of 1 dBm. Nevertheless, this is only viable because the input signal has a high power. The conversion losses start resembling the datasheet parameters at 9 dBm, the same happens with LO-IF isolations. The RF-IF

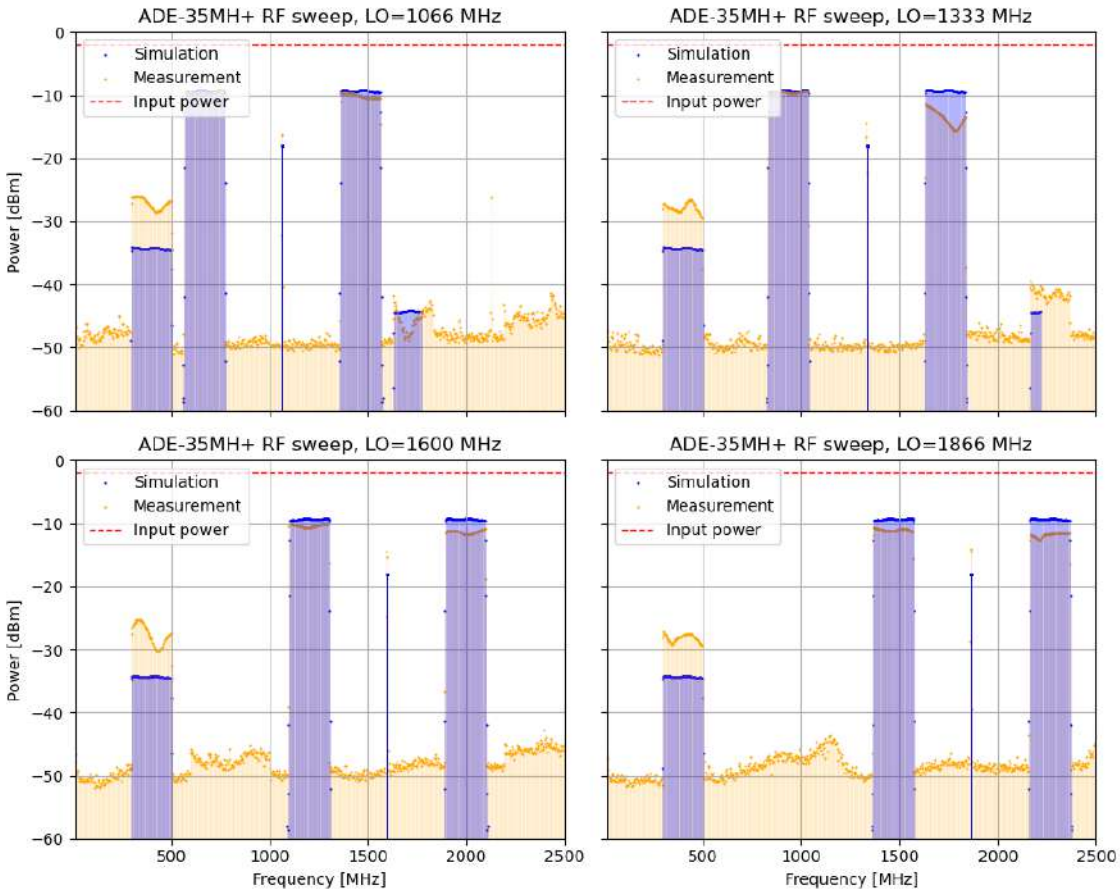

Figure 3.13: Comparisons of measurements and simulations of the response of the ADE-35MH mixer. The measurements were made for the four FDM LOs to obtain the response of chains 1 to 7. The response between 300–500 MHz, where the orange line is above the blue one, means that the RF-IF isolation was less than expected. The response where the orange line is below the blue one means that the conversion losses were higher than expected; this is the case for chains 3, 4, 5, 6, and 7. In most cases, the losses are slightly higher. However, chain 5 shows a considerable difference, as shown in the top right plot.

isolations are slightly lower than the datasheet, as was observed in the first mixer tests. However, the values seem to improve at higher LO powers. This LO power will depend on the signal generator that will be used in CHARTS, but achieving an LO power higher than 9 dBm will be necessary for the success of the project.

The same type of measurements were made for the differential mixer. The results of the RF frequency sweep are observed in fig. 3.14. The mixer's response on the IF band differs for each chain, compared with the ADE-35MH mixer, is less plane. This difference is because of the non-regular amplification of the internal mixer and the L-matching network of the IF port. On the other hand, the L-matching network helped attenuate the mirrored IF band; this characteristic will improve the response of the FDM by reducing the coupling among chains. The mixer also has conversion gain, as previously explained. This gain can be obtained by subtracting the input RF signal marked as the red line versus the output power of the IF signal, and it decreases on the last FDM chains.

Table 3.6: LO Power, Conversion Gain, LO-IF Isolation, and RF-IF Isolation for the MAX2673 mixer. The input RF signal was a tone in 400 MHz with a power of −17.4 dBm. The LO frequency was 1066 MHz.

LO Power (dBm)	**Conv. Gain (dB)**	**LO-IF Isol. (dB)**	**RF-IF Isol. (dB)**
−30	+5.9	+11	−1.3
−25	+10.7	+11.2	−0.5
−20	+14.36	+15.3	+3
−15	+15.8	+22.2	+7.3
−10	+16.16	+24.1	+8.8
−5	+16.28	+25.4	+8.8

The LO variation of the mixer is shown in table 3.6. The LO power was varied from −30 dBm to −5 dBm. The conversion gain, LO-IF isolation, and RF-IF isolation were calculated in the same way as the ADE-35MH mixer. The results show that the mixer starts working correctly at an LO of −15 dBm. However, it is recommended to stay at −10 dBm because the behavior improves at higher LO powers. The conversion gain at CHARTS frequencies is higher than the manufacturer specifications of table 3.3, at least on chain 1. The same happens with the LO -IF isolation, which is higher than the datasheet. The RF-IF isolation is lower than expected, and in some cases where the LO power is too low, there is a slight amplification of the RF signal. For the previous reason, attenuating the RF signal in later FDM designs is of great importance.

Finally, it was measured that if the mixer power supply drops below 2 V, the conversion gain and the other parameters start to drop. This means that a stable power supply is needed to maintain the correct functionality of the mixer. The power supply was set to 3.3 V for the measurements, and it is recommended to keep it at this value.

3.5.3 Combiners results

The results of the two-way combiner testing boards are shown in fig. 3.15. The ports one and two are the input ports, and port three is the output where the signals are combined. It is observed that the two-layer PCB behaves similarly to the datasheet, maintaining similar insertion losses and reflections. In the case of the four-layer PCB, the insertion losses are worse than expected; the same happens with the reflections. These high reflections could be the reason why this component was not working as expected in the first FDM prototypes.

The four-way combiner results are shown in fig. 3.16. Ports one to four are the input ports, and five is the output port. The reflections on port five were not added because they should not affect the FDM functionality. The results show the same problem as the two-way combiner; the insertion losses are worse in the four-layer PCB compared to the two-layer PCB. The same happens with the reflections, where, in both cases, the reflections increment near 2 GHz.

In both PCBs, the results are better in a two-layer composition. These first FDM prototypes can be designed as two-layer boards. However, later FDM boards will need to add a

5 V power supply layer to power the mixers of the antennas. The four-layer PCB is a better option to implement all those and more added features. The high reflection in the two-way combiner may have caused undesired behaviors inside the FDM, which could have created standing waves and higher losses than the ones shown in the combiners by themselves. For this reason, it is recommended to find new combiners or to design a custom combiner that fits the FDM requirements.

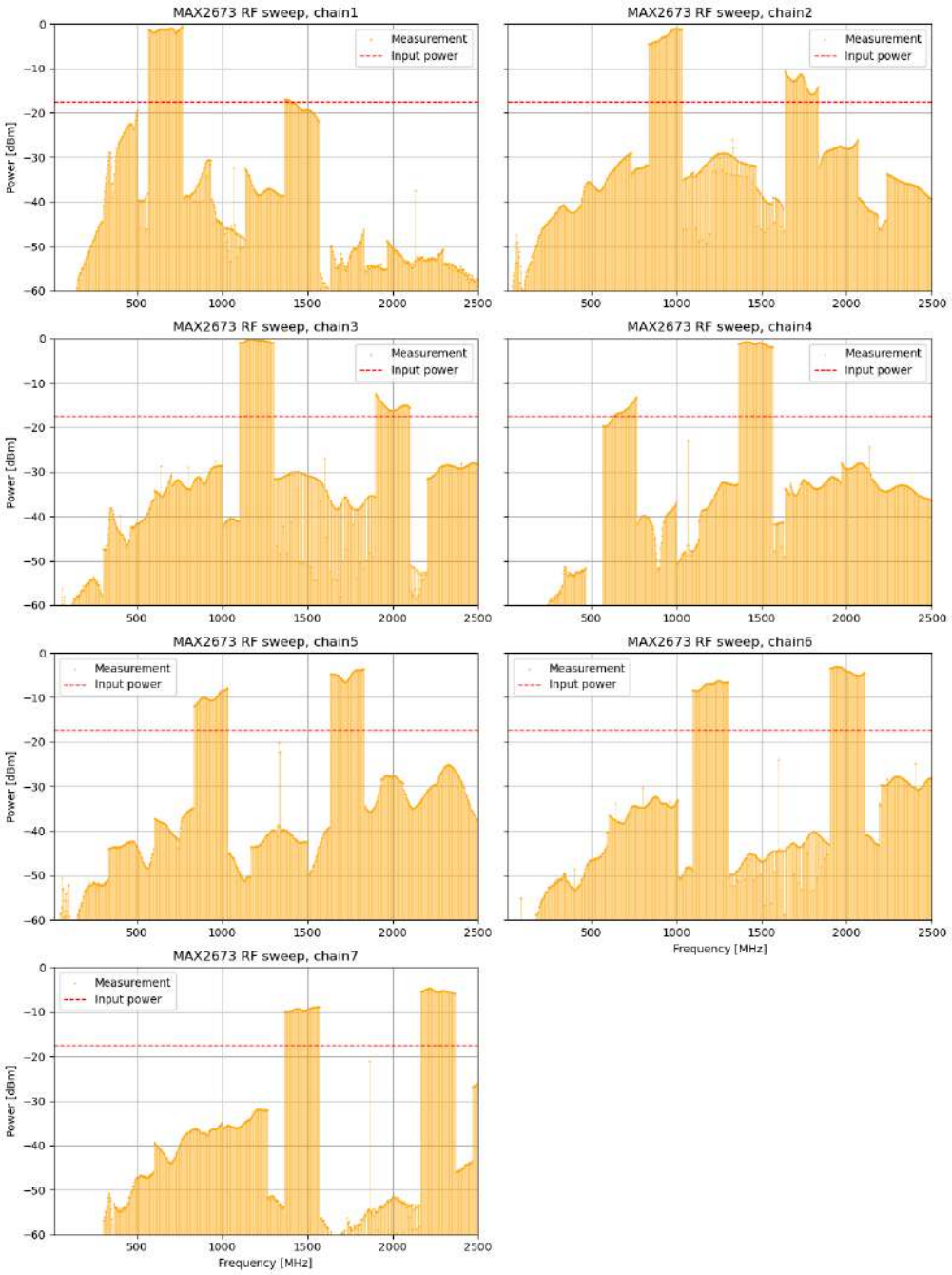

Figure 3.14: Comparisons of measurements and simulations of the response of the MAX2673 mixer. The measurements were made for the chains 1 to 7 of the FDM. The power of each chain compared to the input power, shown in the red line, shows the internal amplification of the mixers. This amplification is not regular on the band. The undesired LSB or USB was partially filtered by the L-matching network of each chain.

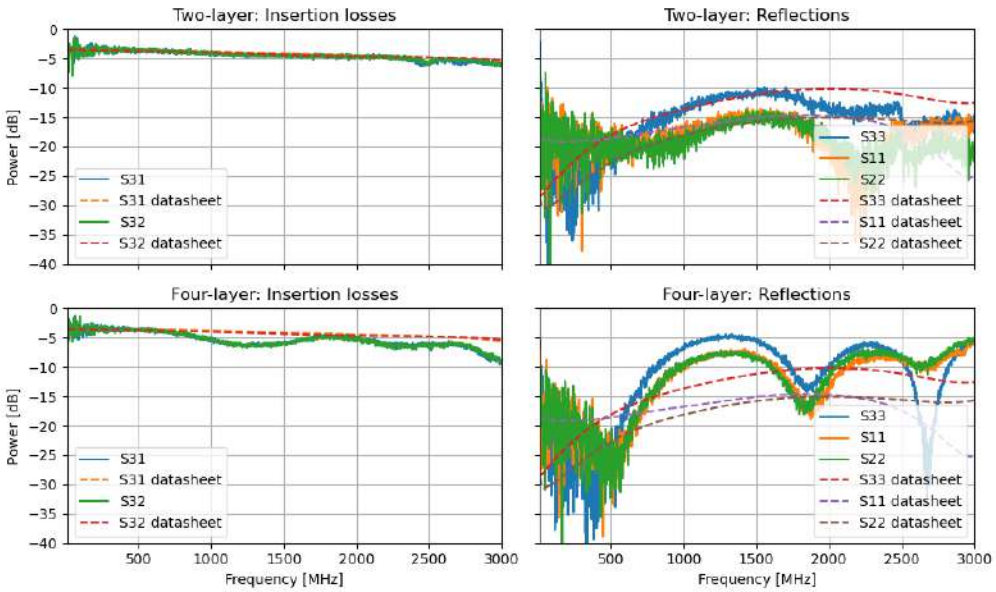

Figure 3.15: Two-way combiners soldered in a two-layer PCB (top plots) and four-layer PCB (bottom plots). The results of the insertion losses and the reflections were measured and compared with the manufacturer specifications. The port where the signals are combined is labeled port 3. Meanwhile, the other ports were labeled as 1 and 2 input ports. The results were obtained using one of the VNA available in the MWL.

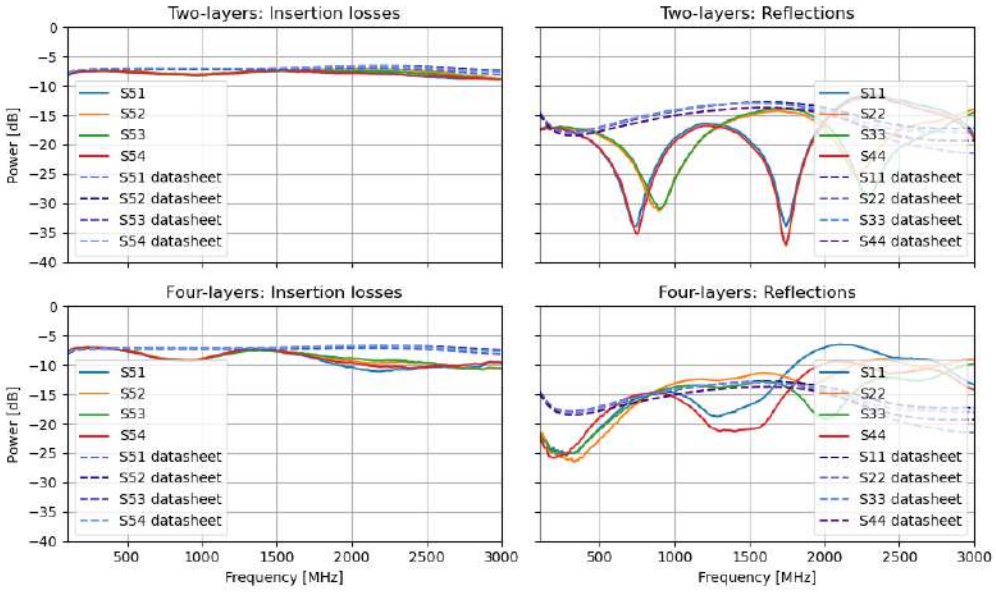

Figure 3.16: Four-way combiners soldered in a two-layer PCB (top plots) and four-layer PCB (bottom plots). The results of the insertion losses and the reflections were measured and compared with the manufacturer specifications. The port where the signals are combined is labeled port 5. Meanwhile, the other ports were labeled as 1, 2, 3, and 4 input ports. The results were obtained using the Siglent VNA available in the MWL.

Chapter 4

FDM Design and Validation

The FDM construction is an iterative process. We started testing the proposed components and verifying whether they fit in the FDM prototype. The next step was to simulate, design, and test each chain separately (isolated) to ensure all frequency channels worked as intended. In the last step, all chains were merged into one board, combining the outputs with power combiners. This chapter presents the design and validation of the separated chains testing PCBs, the single-input FDM, and the differential input FDM. The development and measurements of these boards were made at the UofT, with the support of the University of Toronto Radio Astronomy and InstrumentatioN Lab (UTRAINLab) and Long Wavelength Laboratory (LWLab) teams. The differential FDM was tested on the MWL laboratory, with the help of the AstroLab team.

The separated chains and single-input FDM were labeled as FDM prototypes. The differential FDM, on the other hand, incorporated most of the improvements identified during the testing of individual components and FDM prototypes. Due to these refinements, this model represents the main FDM design and will be the baseline for future iterations. The model can also be used for single output and differential antennas, which are the main proposed antenna models of the CHARTS project.

4.1 FDM simulations

This section presents the simulations of the different FDM prototypes, including individual chain simulations, as well as the final differential FDM design. The simulations were based on the mixer analyses from Chapter 3 and were conducted using the AWR VSS tool.

To validate the performance of each prototype, we first simulated individual frequency chains and the complete single-input FDM system. Since chapter 3 demonstrated that the selected components worked correctly when properly soldered, the same component simulations and parameters were incorporated within the simulations. The primary objectives were to verify the correct operation of each chain, obtaining the conversion losses, RF-IF and LO-IF isolation, and the coupling effects over other chains. Additionally, we examined the

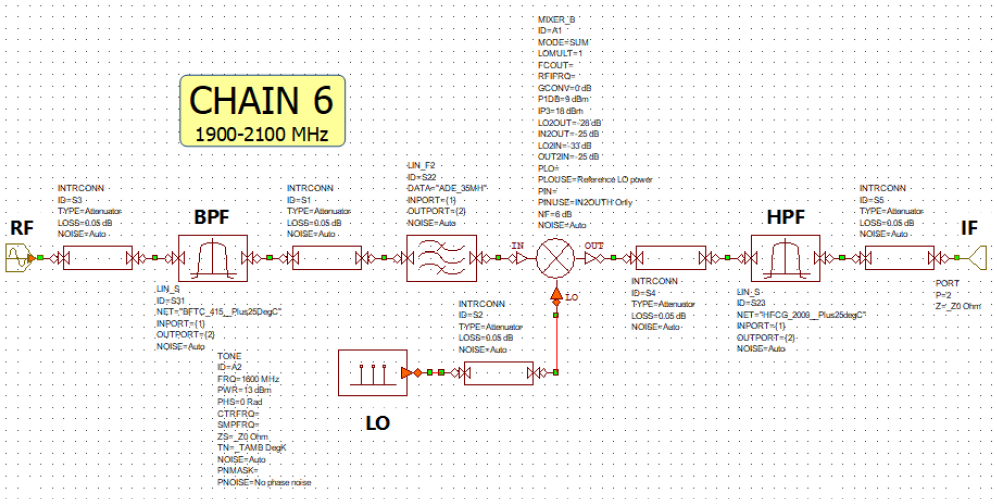

Figure 4.1: Chain 6 simulation schematic made in VSS. The blocks BPF and HPF represent the band-pass and high-pass filters, respectively. The RF, IF, and LO are also marked. This mixer follows the same structure as fig. 3.7, where the losses of the mixer are simulated as a bandpass filter after the mixer block.

behavior of higher-order harmonics to determine their potential impact on the signals. An example of a chain simulation schematic is shown in fig. 4.1.

4.1.1 Single-ended FDM simulation

On the single-input FDM, each chain was combined into a single simulation schematic. A test point tool in VSS was placed just before the power combiner to obtain the spectral power of each individual chain. The power combiner, with its port isolation and insertion loss characteristics, was added after the RF chains. Since these values vary with frequency, an average value was used for the simulations: insertion losses of 3.8 dB and 7.8 dB for the two-way and four-way combiners, respectively. The isolation among chains was 18 dB for the two-way combiner and 20 dB for the four-way combiner. The isolation among ports decreased with frequency while the losses rose, so the actual response of high-frequency chains is expected to be worse than the simulations. The complete single-input FDM simulation schematic is shown in Appendix A, fig. 5.4.

The simulation input changed after the actual measurements of the FDM. Due to the large number of inputs and LOs of the FDM, the available signal generators were insufficient to generate all those input signals. So, it was decided to implement a broadband artificial noise source as the real input of the FDM and later divide that single input into eight noise signals with a power splitter. The noise source was implemented as a chain of amplifiers and filters with the same characteristics as the components used in the previous measurements, listed in table table 4.1. The input power was set to −88.5 dBm to adjust to the actual response of the noise source. The frequency sweep of the input was 100–700 MHz with 301 points. The schematic of the simulated input is shown in fig. 4.2.

The noise source was simulated apart from the FDM simulations. It was incorporated into

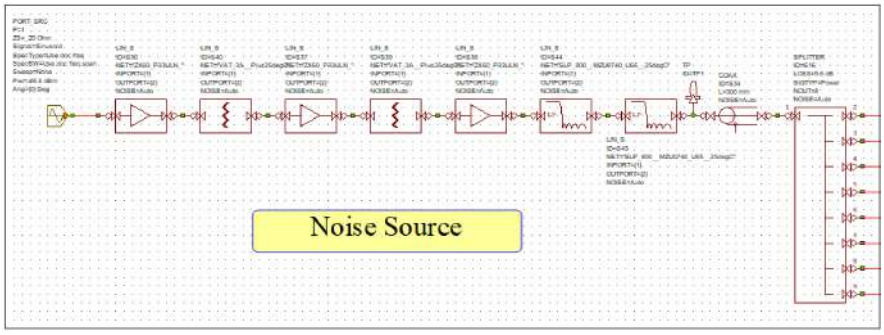

Figure 4.2: Simulated noise source that was made with the parameters of the components used in the actual noise source. The noise source was simulated in VSS to work as an input for more accurate FDM simulations.

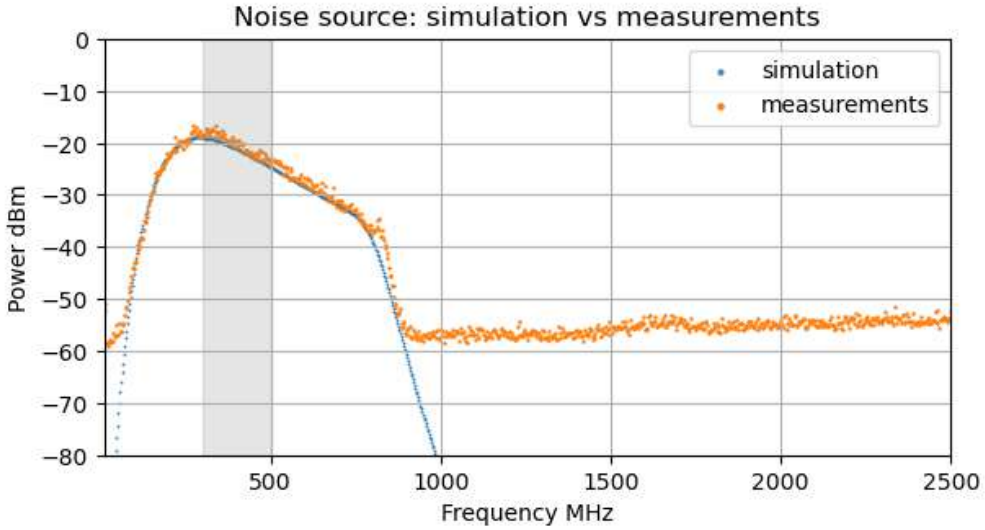

Figure 4.3: Comparison of the real noise source response with the simulated one. Both signals were used as inputs for all FDM chains to validate the correct response of each chain and the final FDM. The gray area represents the input RF frequency 300–500 MHz.

the complete FDM simulation once its behavior closely matched that of the real FDM noise source. A comparison between the actual noise source and simulated noise source responses is shown in fig. 4.3. The responses are not identical, but they are sufficiently similar to be used as an input for the FDM simulations, allowing for a meaningful comparison between actual measurements and the expected response.

The VSS power spectrum simulations work similarly to the mixer simulations. The input signal is tracked throughout the entire RF chain; in the case of FDM, where multiple mixers are included, frequency points increase. This is because additional frequency components appear, including the LO frequency and various IF combinations (up to the fifth harmonic considered).

The power levels of these new frequency components depend on RF-IF and LO-IF isolation, as well as future components that will attenuate the signal. When power combiners are introduced, the simulation also accounts for isolation among chains. As a result, tones

from one chain can couple into another, where they are attenuated by the FDM filters but not entirely eliminated. The multiple frequency transformations and intra-chain couplings increase the total frequency points in the FDM simulation, leading to a final count greater than 301 points. These characteristics make VSS simulations a useful tool for comparison with actual measurements, as they account for all frequency components generated by one chain that may couple into another, as well as higher-order harmonics. Nevertheless, VSS simulations do not consider unwanted reflections, standing waves, or impedance mismatches. This is a limitation, as these effects can significantly impact the performance of the FDM system.

4.1.2 Differential FDM simulation

Similar simulations were made for the differential FDM. In this model, sixteen differential signals from eight differential antennas serve as the RF input. Each of those input signals should be filtered with a bandpass filter before entering the MAX2673 differential mixer. However, in the simulations, only eight RF signals and eight bandpass filters were included. The parameters of the bandpass filter were obtained from the measurements of the insertion losses in the custom bandpass filter of fig. 3.12.

The parameters of the mixer were obtained from the previous measurements of table 3.6 for an LO of $-10\,\mathrm{dBm}$. These values correspond to chain 1 of the mixer, so it is expected that the higher frequency chains will have a lower response. The parameters of the combiners were also obtained from the previous testing boards.

Lastly, to simulate the input of the measurements, an eight-way combiner was included to the input of the FDM to simulate the eight RF signals. The losses of a testing board of commercial baluns were also accounted for in the simulation. The complete simulation is shown in fig. 5.5.

4.2 Design and fabrication

In this section, the design and fabrication of the prototype FDM boards and the differential FDM are presented. The PCB schematics were made in KiCad and fabricated by JLCPCB. The different boards were designed in two different laboratories. The prototype FDMs was developed and soldered in the UTRAINLab, while the differential FDM was soldered in the MWL.

4.2.1 FDM prototypes design

Three designs of FDM prototypes were made at UofT. The first layout was a four-chain FDM, with chains 0 to 3 implemented in a single PCB without a combiner. The second layout was also a four-chain FDM, with chains 4 to 7 implemented in a single PCB and separated outputs. The third one was a single-ended FDM, with all chains implemented in

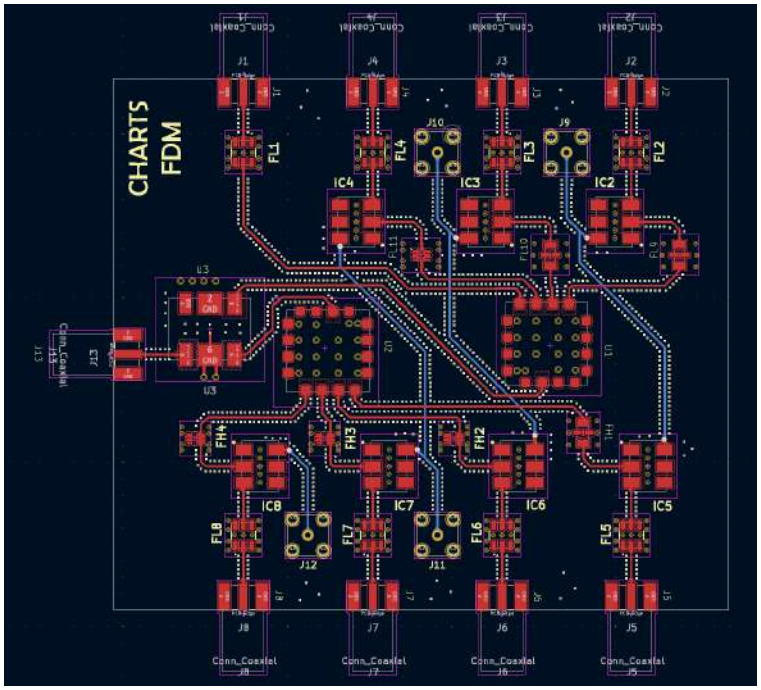

Figure 4.4: Single-ended FDM design made in KiCad with a four layer configuration. The blue lines correspond to the LO frequencies. All the transmission lines were calculated to have 50 Ω impedance at the respective chain central frequency.

a single PCB. The first designs were made to test the response of the chains separately and verify if their response would affect the other chains. The single input FDM was made to test the complete FDM. The PCB schematic of the last single-ended FDM is shown in fig. 4.4.

The transmission lines were selected as GCPW to simplify the connection to the ground, and they were designed to have a 50 Ω impedance at the respective chain central frequency. Multiple vias were added alongside the transmission lines to increase the chain isolation and improve the ground of the PCB. All the designs were made for four-layer PCBs because we wanted to test the response of the components in this type of PCB, and a four-layer PCB increases the number of signals that can be added to the FDM. In the future, the FDM should be able to feed internal amplifiers and the antenna's LNAs, so the addition of more layers can improve the board design.

JLCPB offered a wide variety of materials and stackup configurations for their impedance control PCBs. The used configuration is shown in fig. 4.5. The substrate thickness of this stackup makes the transmission lines narrower than the ones implemented in the LPKF machine. The transmission lines in this configuration have different parameters compared with the LPKF designs; their widths are smaller, which helps to create more compact configurations.

The separated chain FDM prototypes are shown in fig. 4.6. These boards follow the same structure as the simulations. However, the simulations did not consider a proper configuration for the LOs connection. Two types of LO configurations were implemented in the FDM prototypes. The first configuration shown on the left of fig. 4.6 was designed to make the connection of the LOs easier. In this configuration, the paths of the LOs are printed on the

Layer	Material Type	Thickness	
Layer	Copper	0.035mm	
Prepreg	7628*1	0.2104mm	
inner Layer	Copper	0.0152mm	1.1mm (with copper core)
Core>	Core	1.065mm	
inner Layer	Copper	0.0152mm	
Prepreg	7628*1	0.2104mm	
Layer	Copper	0.035mm	

Figure 4.5: JLCPB stackup used in the FDM designs, the substrate used was FR4 with a dielectric constant was 4.4. The thickness of the substrate was 0.2104 mm, a value much smaller than the 1.5 mm available in the laboratory. Figure extracted from JLCPCB (2023b)

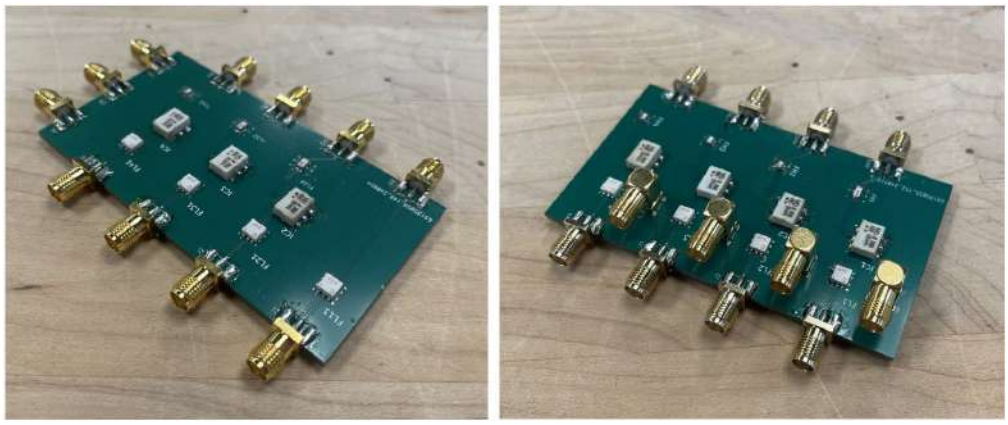

Figure 4.6: Four chain FDM prototypes. The PCBs were made by JLCPCB and soldered in the laboratory. The board on the left was designed to admit the lowest frequency chains (0–3) of the FDM. Meanwhile, the board of the right has the four higher frequency chains (4–7).

bottom layer of the board and directed through vias to the LO port of the mixer. The main problem is that the paths end up being very close; if the isolation among transmission lines is not good enough, the LOs can couple between them.

The second configuration shown on the right of fig. 4.6 was designed to avoid this problem. The LOs transmission lines were also printed in the bottom layer of the PCB, but this time the separation of the transmission lines was bigger. The paths of the LOs in this configuration ended up being of the same physical length.

The final single output FDM prototype is shown in fig. 4.7. This FDM was made to implement all the separate chains into one PCB. The design was made with the same structure as the previous prototypes but with the addition of the power combiners. The chains were located, so the higher frequency chains were placed near the power combiners to reduce the length of the transmission lines. The chains have different frequencies, which means that their electrical paths will be different. If we want to reduce the phase difference between antennas, the physical length of the higher frequency chains should be shorter than the lower frequency chains. This problem can be calibrated once CHARTS backend is constructed, but it was decided anyway to reduce the phase difference inside the FDM.

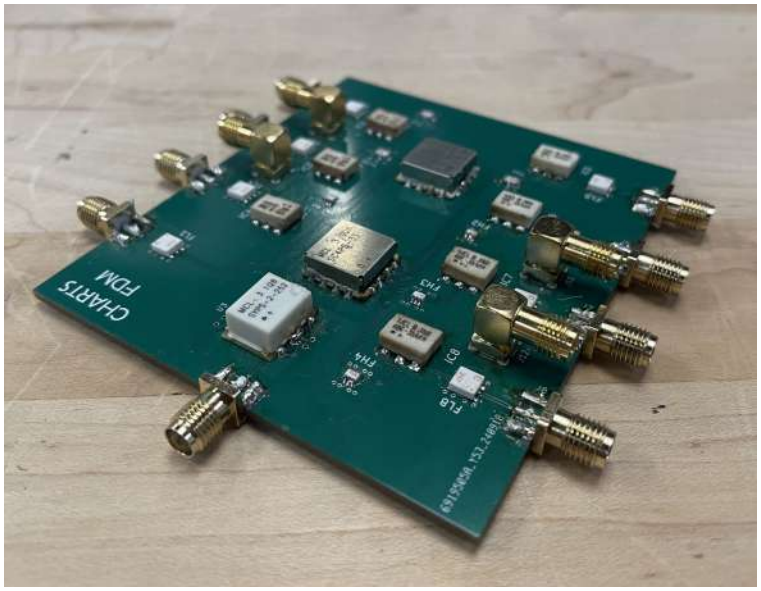

Figure 4.7: Complete FDM prototype. The PCB includes all the chains and commercial components proposed in chapter 3.

4.2.2 Differential FDM design

While the FDM prototypes were being fabricated, the different antenna designs were also being discussed within the CHARTS team. A differential antenna design was one of them, and it was the main reason to follow a differential FDM. Differential circuits had some advantages over single-ended circuits, such as better noise rejection and lower common-mode interference. These characteristics, plus the fact that the UofT team was already working on a differential amplifier design, made the decision to implement a differential FDM. This model does not reject the use of single-ended antennas; some baluns can be added before the FDM to convert the single-ended signal to a differential signal. Making the differential FDM a good option to test the first implementations of CHARTS antennas, differential or single-ended.

The differential model added an improved custom bandpass filter that prototypes did not have and an additional differential mixer, MAX2673. The remaining components, such as the lowpass and highpass filters and combiners, were kept in the design. However, at the time this FDM was being developed, combiners were being studied and their deficiencies. To prevent the bad behaviour of the combiners, two debugging SMA connectors were added between the four-way combiner and the two-way combiner. This way, an external two-way combiner can be added to the FDM to prevent the bad responses of fig. 3.15.

The design of the differential FDM is shown in fig. 4.8. The PCB was sent to be built at JLCPCB, and the components were soldered in the laboratory.

In this model, the transmission line was a microstrip to better implement the custom bandpass filter and differential mixer that was designed with this type of transmission line. The paths of the LOs were made to have the same electrical length between them, something that was not addressed in earlier prototypes. The other problem found on the FDM

Figure 4.8: Differential FDM design and implementation. The PCB was manufactured by JLCPCB and soldered in the MWL laboratory. The lines were designed as microstrips to better adjust to the LC components of the custom bandpass filter and matching network of the mixer. An auxiliary debugging SMA output was added to the design after the four-way combiners. This connection was added to measure the response of the FDM in case the combiners did not work.

prototypes was the lossy designed T-junction that separated the LO paths. In this model, the T-junction was replaced by a two-way Wilkinson splitter, following fig. 2.18. The chains with the same LO were placed near each other to simplify the LO path.

As explained before, the differential input meant that two parallel bandpass filters should be placed on the FDM. These custom parallel filters were placed for every chain before RF port of the mixer. The coupling among the differential signals was a relevant problem of the model, so a parallel custom bandpass filter was designed to study the coupling of these filters. The testing board is shown in fig. 4.9. As tested on previous testing boards, the custom bandpass filter had a good response, but its behavior was dependent on the soldering of the components. The soldering of the LC components was made by JLCPB, with the objective of maintaining a constant response throughout all of them.

In the case of chain 0, which does not have a mixer, a balun was included. The balun used was a commercial component NCS2-771+. It was a low-cost 1 : 2 RF transformer. This component was also used for testing the FDM, so a PCB of eight parallel baluns was designed. The balun board is shown in Appendix A, fig. 5.3.

4.3 Measurement methodology and setup

In this section, the testing methodology and the setup of the different FDM prototypes are shown. The setups changed between the UTRAINLab and Astrolab laboratories because the equipment was different.

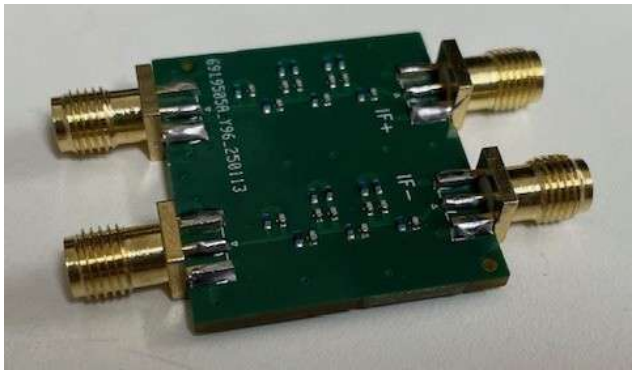

Figure 4.9: Parallel bandpass filters designed on Kicad and fabricated on JLCPCB. The LC components were soldered by JLCPCB to maintain a constant response.

Table 4.1: List of components used in the noise source.

Component	Description	Number
ZX60-P33ULN+	Low noise amplifiers	3
VAT-3+	Attenuators	2
SLP-800	Low pass filters	2
ZCS-8-13-S+	Eight way splitter	1
346B	Noise source	1

4.3.1 Prototype FDM measurement setup

The prototype FDM boards need three elements to work: the eight or four RF inputs, four LOs inputs, and a spectrum analyzer to measure the output. As explained before, the FDM inputs were constructed as a noise source divided into eight noisy signals, and the noise source was implemented with the components listed in table 4.1.

The structure of the noise source follows the same structure shown in fig. 4.2. It starts with a sequence of LNA followed by attenuators. The attenuators were added as a precaution to prevent the amplifiers from saturating. After that, a lowpass filter with a cut-off frequency of 800 MHz was added. The filters were used to narrow down the input signal. This is useful because CHARTS antenna will detect mostly signals in the 300–500 MHz, so we are not interested in higher frequency inputs. Finally, the eight-way combiner was used to simulate eight CHARTS antennas. This component was characterized as it had an average isolation of 21 dB in contiguous ports and 30 dB for separated ports. The losses were almost similar at 9.6 dB; these losses were addressed in the simulations, so the comparisons should be valid.

The first element of the noise source is usually a 50 Ω load at room temperature. Therefore, to increase the power of the signal even more, the 346B noise source was added. This element can amplify the noise floor level, up to a certain amount in this case appropriately 18 dB. The slope present in the signal is produced by the amplifiers; they had higher gains at lower frequencies.

The spectrum analyzer used to read the FDM data was also used to obtain fig. 4.3. This instrument was an Agilent portable VNA. It could work as a VNA and a spectrum analyzer.

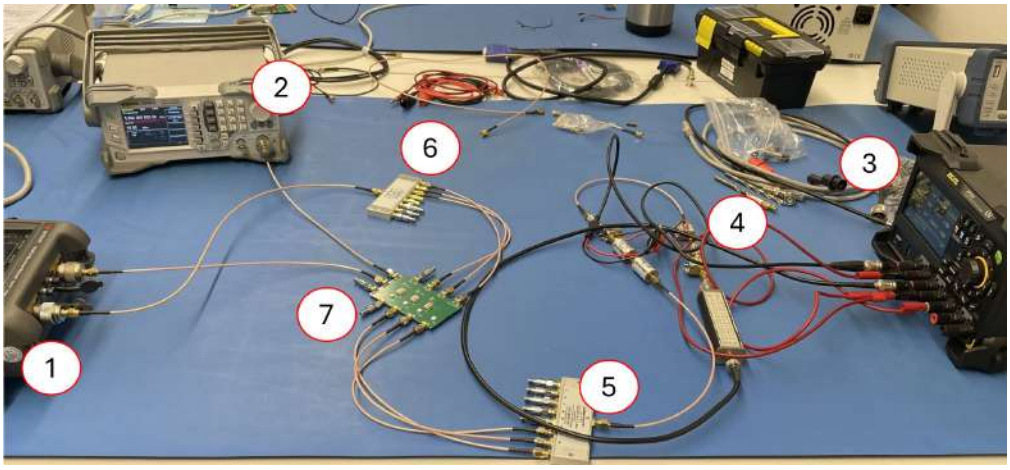

Figure 4.10: FDM measurement setup implemented in the UofT. The components used were labeled as: (1) the portable VNA; this element was set at the spectrum analyzer mode, and it was generating one of the LOs, (2) the signal generator, that produced one of the LOs, (3) the power source that fed the amplifiers of the noise source (4), (5) and (6) are the power splitter/combiners used to measure the low frequency FDM prototype (in case of the high frequencies, and single-ended board only the first combiner was used), finally (7) is the FDM testing PCB. In case more LOs were needed, two RFSoC 4x2 were used.

The spectrum analyzer mode was used to read FDM data by averaging the data. That is why the noise source plot does not seem as noisy as it should be. The same function was used in the measurements of all FDM boards. The instrument could also produce single tones, which were used to generate one of the LOs.

There were three forms to generate LOs: a signal generator, the Agilent portable VNA, and the RFSoC 4x2. All LOs were set at 10 dBm; in the case of the RFSoC LOs, two amplifiers were added to reach the desired power. The setup is shown in fig. 4.10.

4.3.2 Differential FDM setup

The measurements of the differential FDM were made with a Siglent spectrum analyzer in the max hold mode. In this mode, only the maximum value of the signal is captured, permitting the observation of the complete FDM response with an RF frequency sweep as input. The noise source was not used for this measurement. Instead, in the input, the same eight-way combiner was used to create the eight RF signals. After the combiner, the testing PCB of baluns was added to convert the single RF signal to the differential. The RF signal was generated with a signal generator, and the LOs were generated with two RFSoC 4x2. The power and the frequency of the LOs were controlled with the Pynq system. The setup is shown in fig. 4.11.

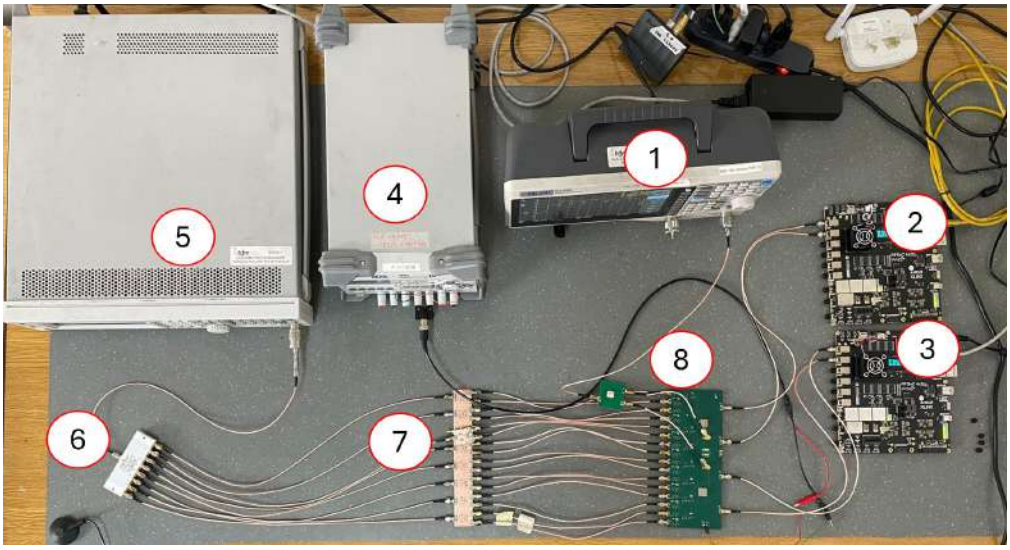

Figure 4.11: FDM measurement setup implemented in the AstroLab laboratory with the help of the MWL equipment. The components used are labeled as: (1) is the Siglent spectrum analyzer that reads the FDM response, (2) and (3) are the RFSoCs that generate the LOs, (4) is the power source that fed the mixers of the differential FDM, (5) is the signal generator that produces the input RF tone, (6) is the power splitter that generates the eight inputs, (7) is the balun testing board that transforms the 50 Ω input to 100 Ω, and (8) is the differential FDM combined with the two-way power combiner testing board.

4.3.3 FDM measurement procedure

For the low-frequencies FDM prototype, two measurements were made: The response of each chain separately and the response of combinations of chains. With the response of each chain, we can obtain the conversion losses of the FDM and compare them to the expected response. The combination of chains was made to observe the coupling effects among chains. The chains were combined with an external eight-way combiner. The measurements were made with the previously described setup. All the unused outputs of the FDM and eight-way combiner were terminated with a 50 Ω load to ensure the correct function of the board and avoid unexpected reflections.

The high frequencies and separated chains FDM were only tested with the first type of measurement. The combination of chains was not possible because the eight-way combiner range was up to 1 GHz. The response of each chain was measured with the same setup as the low frequencies FDM. The response of the FDM was compared with the simulations. The single-ended FDM was tested with the same setup as the separated chains FDM but without the eight-way combiner. The response of the FDM was compared with the complete FDM simulation of fig. 5.4. Additionally, a measurement of the reflections of the FDM output was made with the objective of debugging the strange response of the board. This last measurement gave hints that the combiners were responsible for the low performance of the single-ended FDM. This last measurement was made with the VNA mode.

The differential FDM was characterized using the previously described setup. The first set of measurements evaluated the response of the individual signal chain with an RF sweep signal

of 300–500 MHz. The second set of measurements analyzed the response of the complete FDM using an RF sweep signal from 200–600 MHz. The results for the complete FDM were compared with the full simulation shown in fig. 5.5.

Additional measurements were performed to characterize the balun testing board and the parallel bandpass filter testing board, ensuring the correct operation of the FDM. The effects of the balun testing board on the signal were incorporated into the simulation, allowing for a direct comparison between measurements and simulations. The results from the balun testing board must be corrected to obtain the actual response of the FDM.

4.4 Results and analysis of FDM prototypes

In this section, we present the results of the three designed FDM prototypes. The equipment and types of measurement were previously described. Analyses of the results are made to determine the performance of the FDM and the possible improvements that can be made. These improvements were added in the later differential FDM.

4.4.1 Separated chain FDM

The response of the low frequencies FDM is shown in fig. 4.12. The gray area corresponds to the frequency range of the respective chain. It is observed that the responses in the gray area are similar to the simulations marked in blue. The main difference with the simulations is the presence of the original 300–500 MHz RF signal in the response. This problem was previously detected in the mixer measurements, and it could contaminate chain 0. The addition of high-pass filters on chains 1 to 3 will be necessary to solve this problem unless a mixer with better RF-IF isolation is used.

The difference between the data in fig. 4.12 and the noise source data can be used to estimate the conversion losses of each chain. In this measurement, an eight-way combiner was included to account for the real losses of the FDM. For chains 1 to 3, the data had to be inverted because these chains are flipped after the mixer.

It is important to note that the power difference provides only an approximate estimation of the conversion losses. This is because the power of the noise source, as the name suggests, is not constant, and the same applies to the response of the FDM. The average conversion losses over 200 MHz for each chain are:

- Losses in chain 0: 9.477 dB
- Losses in chain 1: 18.668 dB
- Losses in chain 2: 18.656 dB
- Losses in chain 3: 18.196 dB

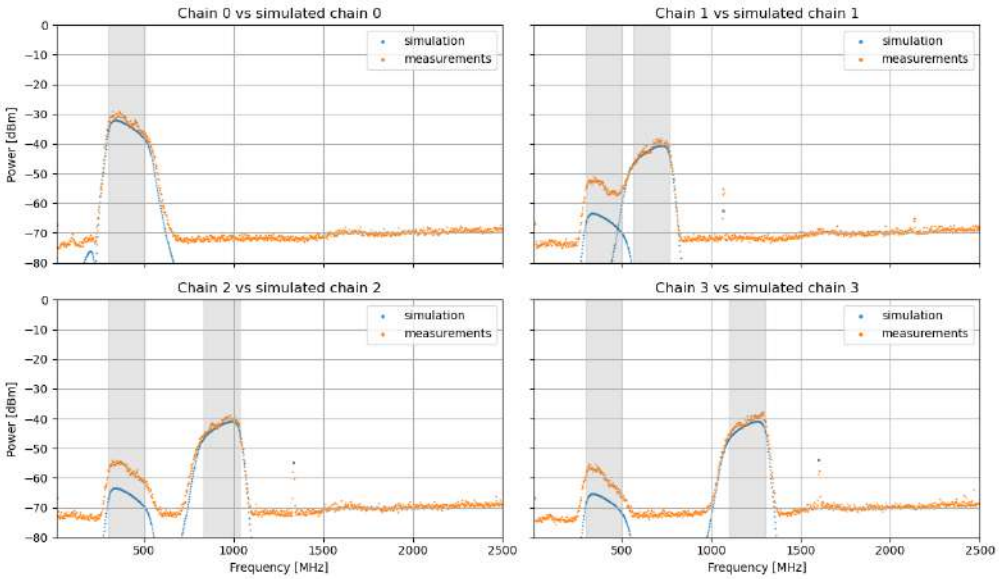

Figure 4.12: Comparisons of measurements and simulations of the response of separated chain FDM. The measurements were made with the noise source of fig. 4.3. The result shows the first four chains of the FDM.

The restriction on the maximum amount of losses in the FDM board was 31.12 dB. In this case, all the low-frequency chains are below that restriction. This means that the digitizer will be able to detect the signal.

In figures 4.13 it is observed that the response of the chains changes when the chains are combined. The combination of chains marked in red has a slightly different response compared to the separated chains. The areas where the separated responses of the chains enter the area of the other chain cause the response of the combined chains to change. This can be observed in the coupling of chain 0 vs chain 1, where the poor RF-IF isolation of chain 1 lowers the power of chain 0. The other effect occurs when part of chain 0 enters the frequency range of chain 1. It is observed that the power increases in that area. This is a problem that was not detected in the simulations, but it has to be addressed in future FDM designs.

It is important to note that the coupling among chains is mostly produced by the signals entering one port of the eight-way combiner and altering the response of the other chain. This is because the eight-way combiner is not a perfect device, and it has a port isolation of 20 dB between adjacent ports. The FDM has a combiner included in the design, so it will suffer the same problems as these measurements.

The coupling effects can increase or decrease the signal depending on the phase. This phase will depend on the LO and the length of the transmission lines. It is recommended to reduce as much as possible the coupling among chains, so the signal integrity is not affected. This coupling can be reduced by filtering the signals. Designing a sharper band-pass filter from 300–500 MHz can reduce the coupling.

The response of the higher frequencies FDM is shown in fig. 4.14. The results show that the behavior of the higher frequency chains deteriorates slightly compared to the simulations,

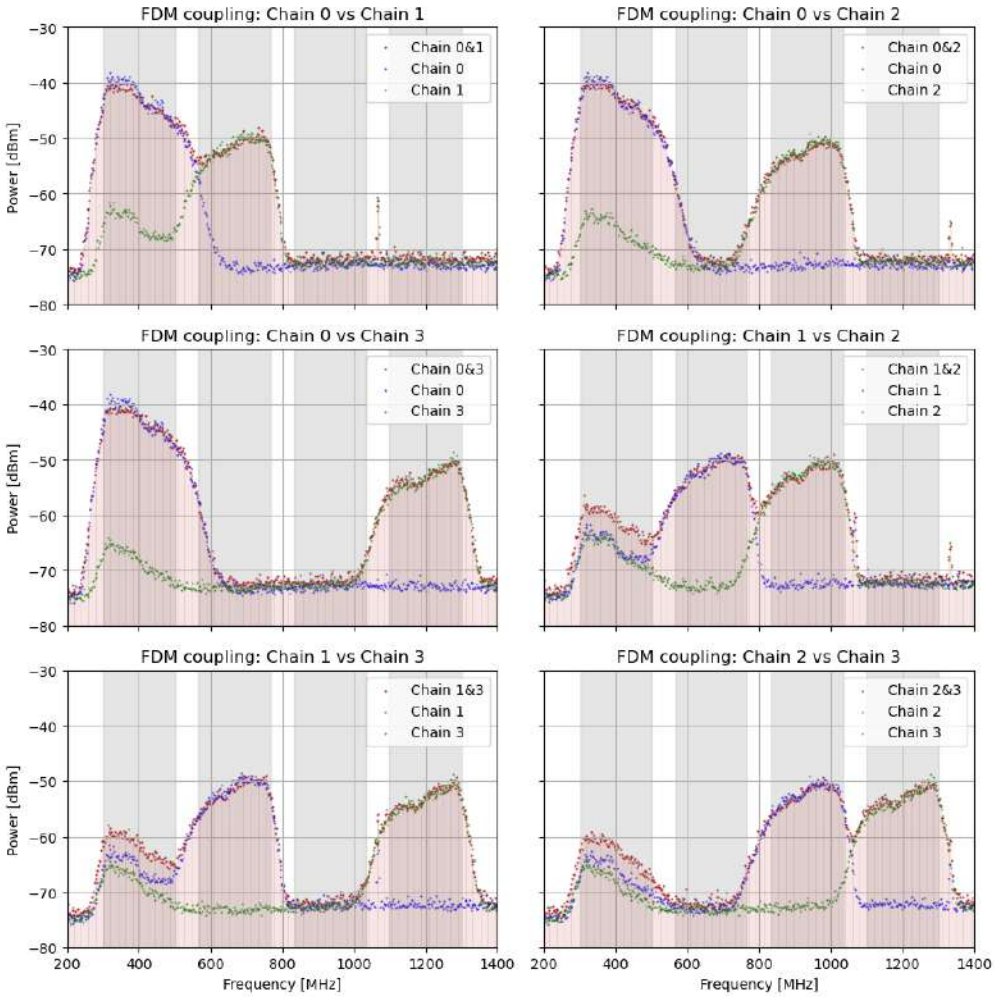

Figure 4.13: Four chain low frequencies FDM measurements, in these plots a comparisons between combining two chains vs the chains one by one is shown. The combination of chains marked in red changes its response when the chains are combined.

but it is still similar to what was expected. The problem of the RF-IF isolations is solved thanks to the addition of high-pass filters. So the previous problem with the coupling to chain 0 is not important in this case. There are a few unwanted spurious signals on chains 4 and 5.

The measurements of the combination of chains were not possible because the eight-way combiner was not able to work at the higher frequencies. But in fig. 4.14 it is observed that the chains do not affect each other. The value of the coupling remains below 20 dB in all high-frequency chains. Which is in accord with the FDM specifications and restrictions.

4.4.2 Single-ended FDM

The complete measurement setup was used to measure the single output FDM. The results are shown in fig. 4.15. The results show that the response of the FDM is similar to the simulations for the low frequencies. However, there is an important problem in the high-

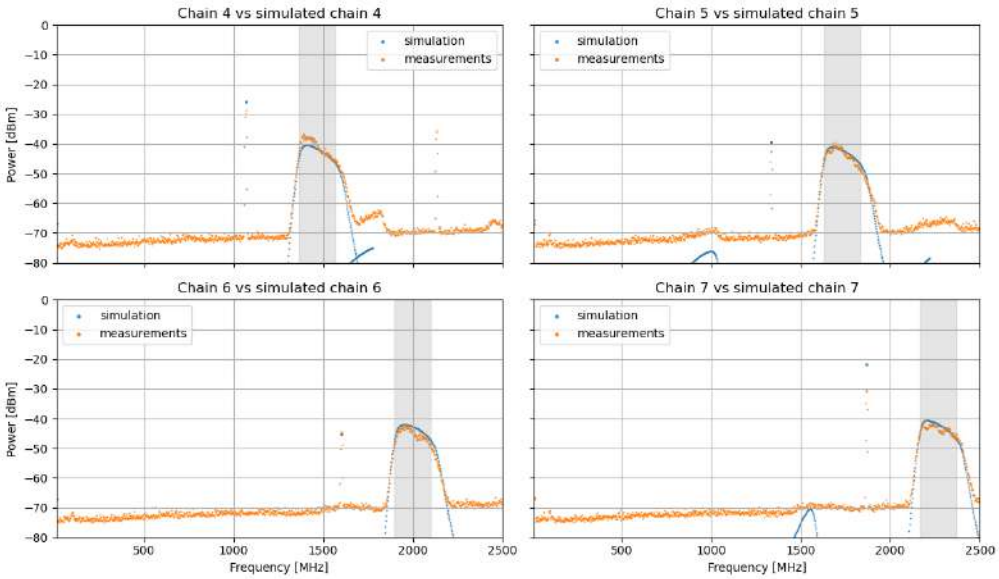

Figure 4.14: Comparisons of measurements and simulations of the response of separated chain FDM. The measurements were made for the last four chains of the FDM.

frequency chains, where the response deteriorates near the noise floor. Although higher losses were expected in the high-frequency bands, the attenuations of the combiners given by the manufacturer do not explain the difference observed in the results. The problems of the four chain low frequencies FDM remain on this board because the same components were used. Mainly because both PCBs were designed at the same time.

4.4.3 Limitations and improvement

The first problem was detected on the BFTC-415 measurements, where the filter was not sharp enough to reduce the coupling among chains. This effect is observed in fig. 4.13, where chain 0 gets mixed with chain 1. This problem should be addressed using the custom bandpass filter. Another problem regarding filtering should be addressed on the lower frequency chains, where it is observed that components of the RF signal could affect chain 0. This problem was also affected by the lower-than-expected RF - IF isolation of the ADE-35MH+ mixer.

The second problem was found after the construction of the final prototype. The combiners were not working properly under a four-layer board configuration. Although this problem was not completely addressed on the differential FDM, it was partially prevented with the debugging output between combiners.

The other problem detected on the board was the asymmetric paths of the LOs. The paths of the LOs were not the same, which can cause phase delays among chains. This has to be improved by adding LO paths of similar electrical length for all LOs. The other problem regarding the LOs has to be with the T-junction that separates the signal to both mixers. The T-junction was not well designed, as seen in fig. 4.16. This configuration can cause reflections and losses in the signal and can provoke the mixers to not be fed with the expected 10 dBm LOs that was set in the signal generator. This T-junction can be redesigned

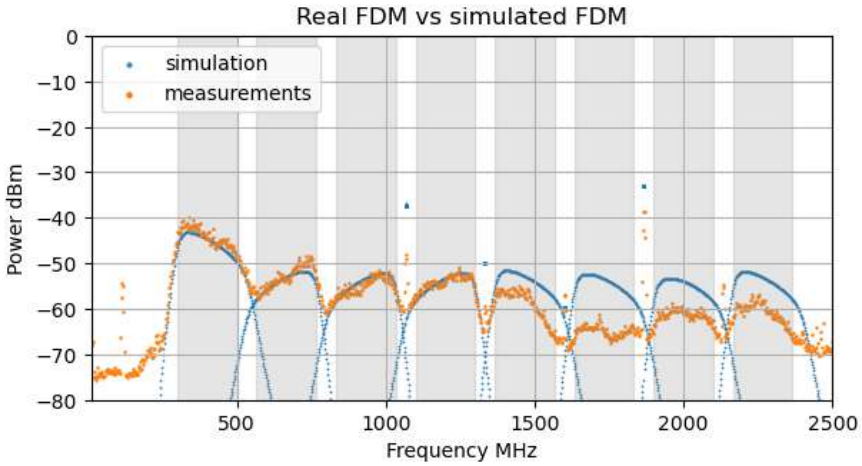

Figure 4.15: Single-ended FDM measurement versus simulations. It is observed that the response of the lower frequency chains is similar to the simulations. However, the response of the higher frequency chains deteriorates. The higher losses were identified as the bad behaviour of the combiner in a four-layer PCB configuration.

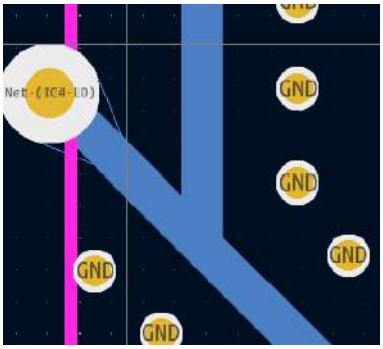

Figure 4.16: T-junction of the single-ended FDM to split the LOs to the mixers. The microstrip power splitter was not well designed because the angle of the T-junction was not 90°. This caused the LOs to be not split properly, and the mixers were not being fed with the expected 10 dBm LOs.

as a two-way Wilkinson power splitter as shown in fig. 2.18.

4.5 Results and analysis of the differential FDM

First, the measurement of the parallel filters is shown in fig. 4.17. These measurements were made with the VNA connecting the input of one of the filters and the output of the other. It is observed that the coupling on the desired 300–500 MHz is below −70 dB. The coupling between filters is much lower than the −25 dB specified on chapter 3, so we can work with those filters, ignoring their minimal cross-talk.

The results of the differential FDM with each chain excited separately are shown in fig. 4.19, where the results are compared with the corresponding AWR simulations. In most

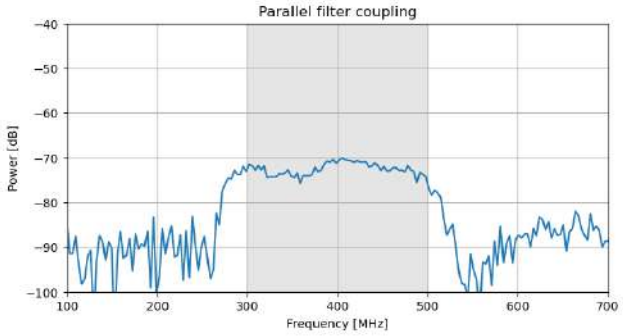

Figure 4.17: Coupling of the parallel custom bandpass filter used in the differential FDM. The measurements were made with the Siglent VNA, connecting the input of one of the filters and the output of the other. The rest of the ports were terminated with a 50 Ω load.

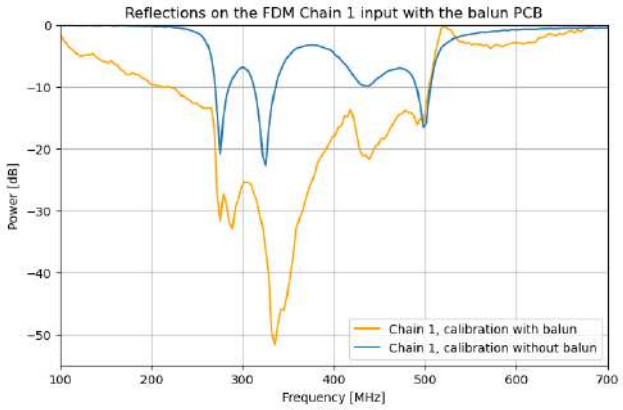

Figure 4.18: Reflections on the chain 1 input with two different calibrations of the VNA. The blue line is the S_{11} when the calibration does not consider the balun PCB reflections. The orange line considers the balun PCB reflections. The measurements show that the balun PCB increases the reflections of the FDM input.

cases, the measured responses show more gain than the simulations. One possibility for this discrepancy is that the simulations used the typical values of the mixers (i.e., conversion gain). As shown in fig. 3.14, the conversion gain of the MAX2673 mixers changes with different RF and LO combinations, and is higher compared with the 8.6 dB gain given by the manufacturer. The measurements also show that the frequency responses of the chains are not flat, with a noticeable drop in power around the center of all chains. Besides the non-constant gain of the mixer, this drop in power can be attributed to the reflections of the bandpass filter and the baluns used in the measurement setup. To check reflections of the FDM, two measurements of the inputs S_{11} were made; the difference between the two measurements was in the calibration of the VNA, one of them considered the baluns in the calibration, and the other did not. The results shown in fig. 4.18 present that the reflections of the FDM get worse when the testing balun board is added to the setup. This can produce a drop in power in the response of each chain.

Other parameters that may have affected the difference between simulation and measurements are the behavior of the combiners. The four-layer four-way combiner data was used for the simulations, which is the same configuration used in the FDM. However, the combiner

integrated with other components may not behave the same way as when it is tested alone. Additionally, VSS simulations did not account for reflections, limiting their comparability with measured results. A complete empirical characterization of mixer gain is recommended for more accurate simulation matching.

The coupling among chains is shown in fig. 4.20. These plots use the same individual chain measurements, highlighting how each chain affects the others (in orange). It is important to notice that there are some external tone signals that are affecting the measurements. They were identified as spurious of the LOs and nearby Wi-Fi sources, particularly around 2.4 GHz. Those signals create extra peaks in the response of the chains, which decreases the signal integrity of them. To avoid this problem, the LO signals should be filtered before entering the FDM. The RFI produced in the 2.4 GHz band can be reduced by isolating the FDM in an RF shielded box.

As stated before, the coupling among chains should be reduced up to 25 dB (compared with the lowest difference between the chain and the coupling). Chains 1, 2, and 3 are the ones that affect the other lower-frequency chains the most. This is because, as with the single-ended FDM, the low-frequency chains only have a low-pass filter. This filter should be replaced with a custom bandpass filter to reduce those couplings. Chain 3 also has high coupling to chain 6, so it should be addressed. On the other hand, the effects of the higher frequency chains are below 25 dB in all cases, so the FDM can keep the high-pass filters of those chains.

The measurements of the complete FDM response are shown in fig. 4.21. The comparison of the complete FDM response versus the simulations is shown in the left figure. Where the difference in gain can be explained by the same reasons as the separated chain measurements. The right figure shows the complete FDM response versus the separated chain measurements. In this plot, it is observed that chain 0 is the most affected by the other chains' coupling. The other chains' responses remain consistent with the individual measurements.

Although the differential FDM shows some irregularities, they may not pose a significant problem as long as the system is well characterized and the behavior remains consistent across all boards. This can be possible if the IF signals are only being affected by higher losses than expected. However, more reflections produced by the soldering can cause the boards to not share their responses. Therefore, professional soldering is recommended to ensure repeatability. The current soldering was performed in laboratories, which may explain some of the problems. It was also detected that some of the testing balun components were not working properly, and changing them between chains changed the response of the FDM. So their effect on the response should be characterized. The balun testing board is not part of the FDM. One last possibility of error inside the FDM board is also related to the combiner. The intersection area between the combiner and the low and high pass filters should be impedance matched to 50 Ω. The use of filters may cause the impedance seen from some ports to be not 50 Ω in specific frequencies. Suppose the seen impedance at a particular frequency becomes an open or short circuit. In that case, the reflections of the combiner will increase, and the expected parameters will not be achieved. This problem can be solved by using an intermediate element adapted to 50 Ω between the filter and combiner. This element can be a matching network or something like an amplifier or attenuator.

4.6 Summary of results

The differential FDM incorporated some improvements over the previous single-ended FDM. The most important improvement was the addition of the custom bandpass filter, which reduced the coupling among close chains. The LO splitter was also corrected to reduce the reflections and to ensure that the proper LO power was delivered to the mixers. Finally, the two-way combiner was bypassed to reduce the losses in the FDM, and an external two-way combiner was used instead.

There were some problems that were not solved in the differential FDM. These problems and possible solutions are listed below:

- **Coupling among low-frequency chains:** The custom bandpass filter helped to reduce the coupling, but the remaining RF signal, and in some cases, the USB band was not completely filtered. To solve this problem, more custom bandpass filters should be designed.
- **Four-way combiner:** The four-way combiner was not working properly under a four-layer board configuration. This can be solved by designing custom Wilkinson combiners with microstrip structure inside the PCB.
- **Unexpected reflections on the input:** The reflections of the bandpass filter inside the FDM get worse when the testing balun board is used. This may produce an increase in the losses of the different chains.
- **Spurious LO signals:** The spurious signals produced by the LOs and nearby Wi-Fi caused some unwanted RFI that was also being frequency converted. This can be solved by filtering the LO signals before entering the FDM. The RFI produced in the 2.4 GHz band can be reduced by isolating the FDM in an RF shielded box.
- **The non-constant gain of the FDM:** The response of the FDM is not flat; there are some explanations for this behavior. One of the possible effects is the non-constant gain of the mixer; this parameter should be properly characterized for all FDM frequency bands. It is also possible that the soldering of the components was not done properly. This can be solved by using professional soldering.
- **Unexpected reflections in the combiner:** The use of different filters right before the combiner may cause the impedance seen from some ports to be not 50 Ω in specific frequencies. This can be solved by using an intermediate element adapted to 50 Ω between the filter and combiner.

On the other hand, the differential FDM successfully reduces the losses in the chains by incorporating the active MAX2673 mixer. The separation of all chains was properly achieved, and the mixers can operate with low-power LO signals, potentially eliminating the need for LO amplification before entering the FDM. The LOs and their harmonics fall outside the chain bands as designed; they do not interfere with other chains. With these characteristics, the FDM can be used for early CHARTS pathfinders, such as CHARTS-8, which is planned to be constructed in Cerro Calán.

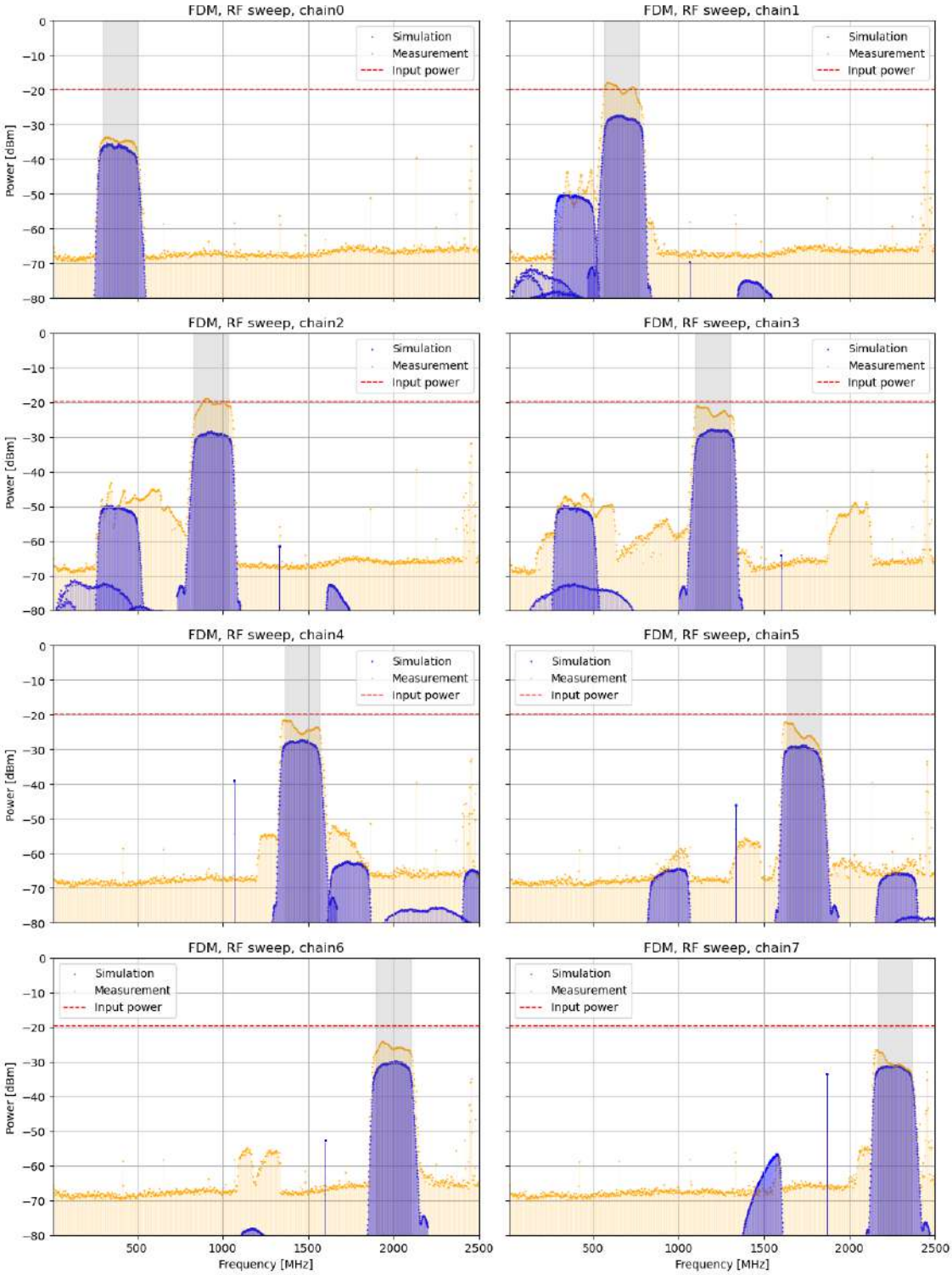

Figure 4.19: Separated chain test on the differential FDM. The vertical axis shows the actual power (in dBm) measured in the spectrum analyzer, over a frequency range of 10–2500 MHz. The results were compared with the AWR simulations, and these simulations were based on the manufacturer's parameters of the mixers and the obtained results of the combiners and the balun testing board. The red line is the input power after the eight-way combiner. The gray area corresponds to the frequency range of the respective chain.

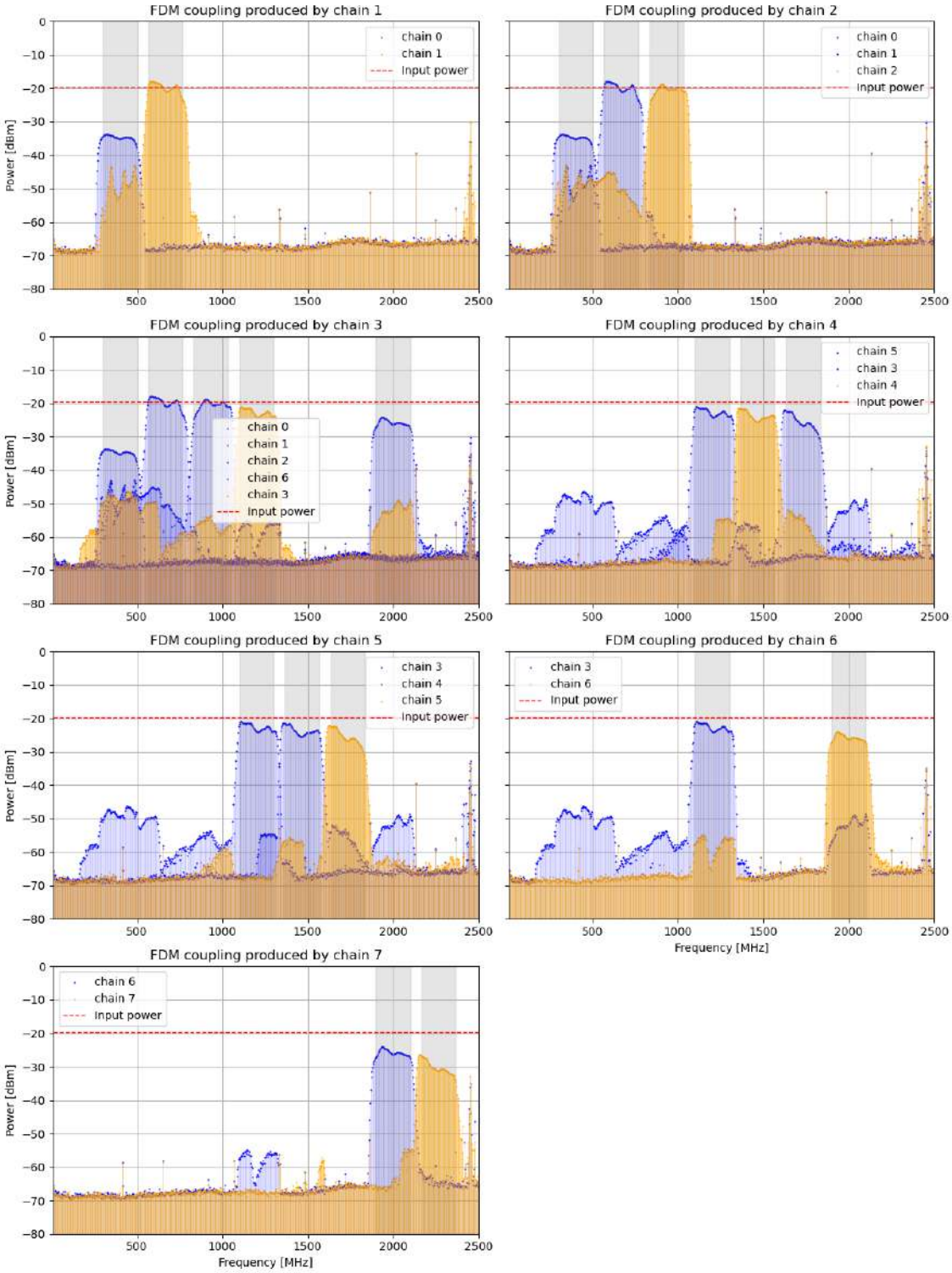

Figure 4.20: Coupling produced by FDM chains. The residual signals were not completely eliminated, and they are contaminating the response of the other chains.

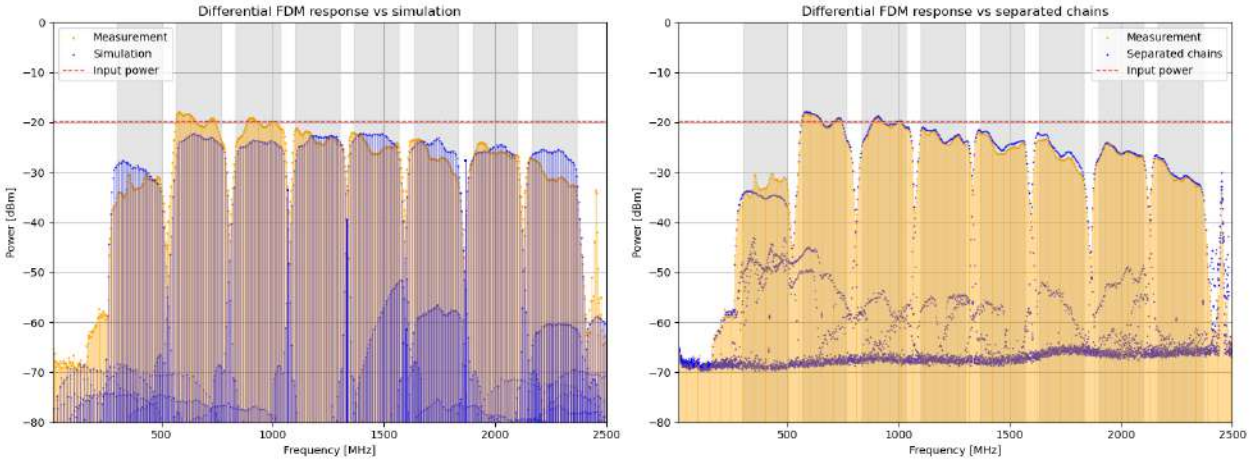

Figure 4.21: Right figure: complete differential FDM response versus simulations. Left figure: complete differential FDM response versus separated chain measurements. The chain with the most changes is chain 0, where it was detected that the coupling from other chains was greater. The other chains are similar to the separated chain measurements, except for chains 5 and 6, which have a slightly different response. The gain of the complete FDM is greater compared to the simulations. This is because the simulations used the typical values of the components, and the measurements were made with the real values of the components.

Chapter 5

Conclusions

The thesis presented here describes the design and implementation of frequency division multiplexing technology, a fundamental piece of hardware for the CHARTS project. As a radio array in its mid-development stages, the CHARTS project has seen the FDM board progress alongside it. The proposed FDM adapts to the latest antenna designs, featuring a modular design that can be used for different types and numbers of antennas. The individual components have been simulated, tested, and incorporated into the complete board. The differential FDM addresses and enhances most of the issues that were present in earlier versions. The development of the FDM is closely tied to the differential design model, which will guide future versions of the board and CHARTS project. While the system is not without flaws, its issues have been identified, and potential solutions have been proposed.

FDM technology enables the multiplexing of signals from eight CHARTS antennas, significantly reducing losses by incorporating differential active mixers. The eight signal chains are successfully separated in the frequency domain by custom bandpass filters and the mixers. This new combination of signals properly utilizes the full sampling rate of the latest RFSoC 4x2 technology, which will be implemented in the CHARTS backend. The system was characterized, and it can be used to test the complete CHARTS frontend structure, including antennas, LNAs, and the RFSoC spectrometer. However, there are still areas for improvement within the FDM, mostly related to the coupling among chains.

5.1 Future Work

The FDM is a work in progress, with some remaining points to improve. The next step in the FDM development is the implementation of new upgrades that will improve the performance of the board. The next step is to implement the board in the CHARTS RF receiver. The FDM should be tested with the CHARTS-8 deployment, and the complete system should be able to work with real data. The installation on the site will give the opportunity to test the FDM with real data and visualize further possible improvements to the entire system.

5.1.1 CHARTS-8

Most of the different parts of the CHARTS project have been tested separately. The next step is to test eight antennas at once, amplify them with the first and second stage LNAs, and then combine them with the FDM. For this first pathfinder installation, the current FDM can be properly used to test the system and identify more areas of improvement. The backend of the system will be tested as well, using the RFSoC 4x2 to read the data, process it, and send the data to the computer.

5.1.2 New FDM design

The new FDM board is being designed to improve the performance of the differential FDM. Its main goal is to reduce the coupling between the RF signals and replace the combiners that were not working correctly. The new design will include custom bandpass filters, a custom eight-way combiner, equalizers, and amplifiers. The new FDM schematic is shown in fig. 5.1.

As previously mentioned, the low-frequency chains need to attenuate the RF signal that was not properly filtered. The addition of custom bandpass filters will help to reduce the RF coupling that is affecting chain 0 in the current FDM board. To reduce the coupling, an amplifier was also added to chain 0 to compensate for the losses of the balun.

The equalizers will be used to flatten the initial RF signal that will have more power on the low frequencies. The first equalizers will be designed to work in the 300–500 MHz range. They should be simulated alongside the custom bandpass filters to see if their addition will affect the reflections of the FDM input. A final equalizer should be added before the FDM output to flatten the response of the FDM that has more losses in the higher frequencies, as shown in fig. 4.21.

The custom eight-way combiner was already designed and constructed by the CHARTS team, and it is shown in fig. 5.2. The measurements of this combiner seem promising, with 20 dB of isolation among outputs. The PCB was made in a four-layer configuration, so it should be easily incorporated into the FDM design. Its response with other components should be simulated and measured before being incorporated into the FDM.

The amplifiers are planned to be commercial LNAs. They will be used to amplify each chain separately. Also, adding the amplifiers between the last bandpass filters and the inputs of the combiners will help reduce the combiners' reflections. These reflections and the combiner's bad behavior could be one reason for the strange response of the current FDM board. The amplifiers will divide the RF network, so the impedance looked from one input port of the combiner will always be 50 Ω.

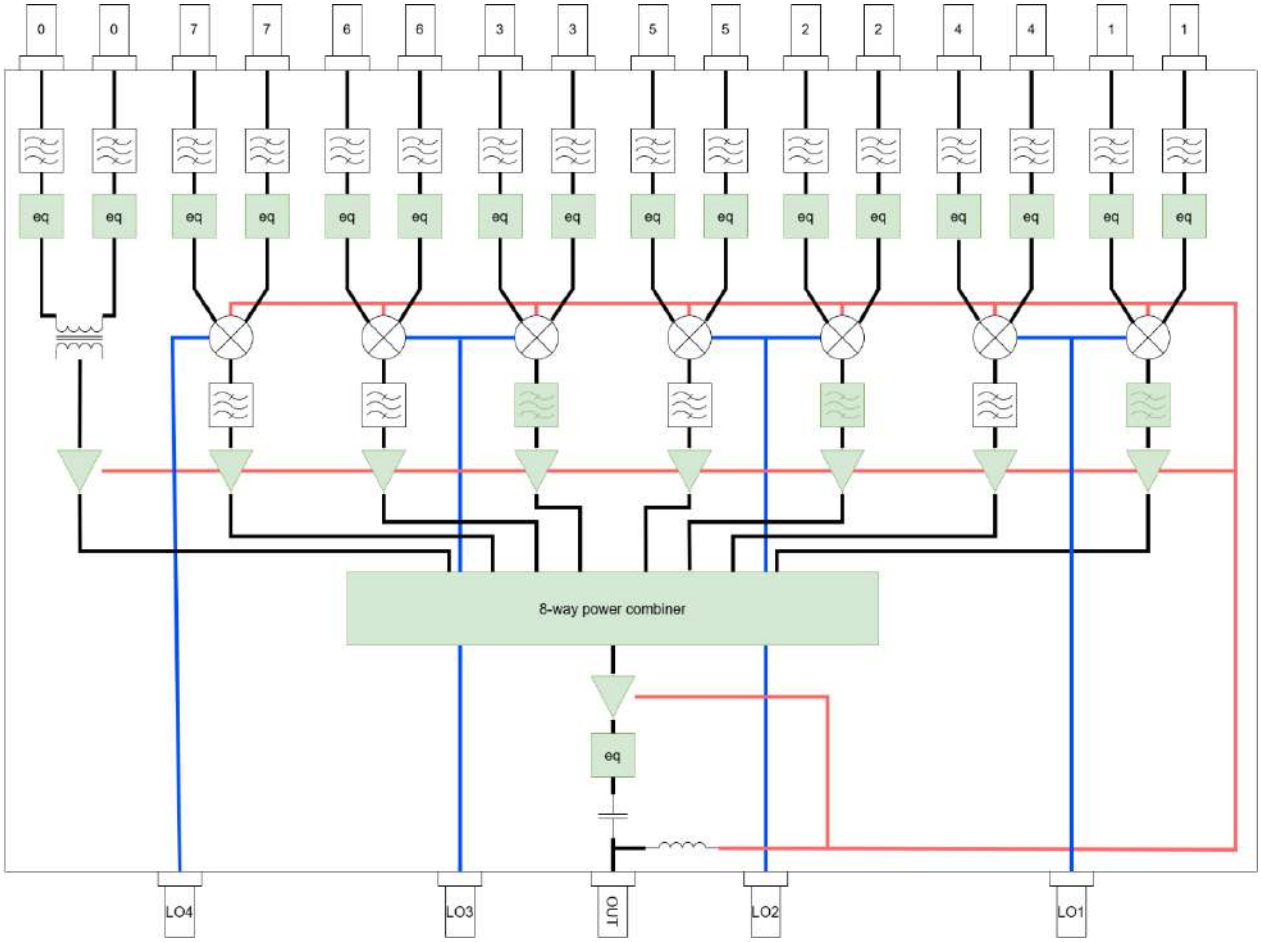

Figure 5.1: New FDM diagram for future iterations. The green blocks are the new components that will be added to the FDM to improve its performance. The new components are: equalizers, custom bandpass filters for chains 1–3, custom eight-way combiners, and more amplifiers. The blue lines correspond to the LO signals, and the red lines are the 3.3 V power lines that will be used to power the internal FDM amplifiers and mixer. The power line should also power the LNA of each antenna.

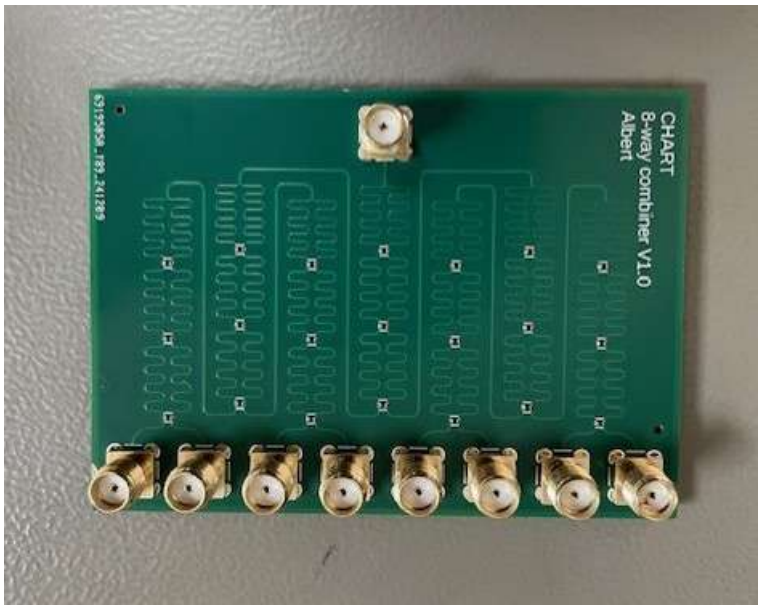

Figure 5.2: New custom eight-way combiner. The combiner was designed in a four-layer PCB by the CHARTS team. Its port isolations are approximately 20 dB for the nearby port, and 30 dB for the other ports.

Bibliography

Andersen, B., Bandura, K., Bhardwaj, M., et al. 2020, Nature, 587, 54–58, doi: 10.1038/s41586-020-2863-y

Bethapudi, S., Spitler, L. G., Main, R. A., Li, D. Z., & Wharton, R. S. 2023, MNRAS, 524, 3303, doi: 10.1093/mnras/stad2009

Carr, J. J. 2002, RF Components and Circuits (Oxford: Newnes), doi: https://doi-org.myaccess.library.utoronto.ca/10.1016/B978-0-7506-4844-8.X5000-2

Cassanelli, T., Leung, C., Rahman, M., et al. 2022, AJ, 163, 65, doi: 10.3847/1538-3881/ac3d2f

CHIME/FRB Collaboration, Amiri, M., Andersen, B. C., et al. 2021, ApJS, 257, 59, doi: 10.3847/1538-4365/ac33ab

Collaboration, C. 2023a, CHIME Experiment. https://chime-experiment.ca/en

—. 2023b, CASPER - Collaboration for Astronomy Signal Processing and Electronics Research. https://casper.berkeley.edu/

Collaboration, F. 2023c, FAST Telescope. https://fast.bao.ac.cn/

Collaboration, U. 2023d, UTMOST - The Molonglo Radio Telescope. https://astronomy.swin.edu.au/research/utmost/

Devices, A. 2023, MAX2660-MAX2673 Datasheet. https://www.analog.com/media/en/technical-documentation/data-sheets/max2660-max2673.pdf

Digital, R. 2023, RFSoC 4x2 Hardware. https://www.realdigital.org/hardware/rfsoc-4x2

Electronics, M. 2023, About Us - Mouser Electronics. https://www.mouser.ca/aboutus/

Fouquet, F. 2020, Friis Formula, 23–35, doi: 10.1002/9781119706656.ch2

JLCPCB. 2023a, JLCPCB - Prototype and Small Batch PCB Production. https://jlcpcb.com/

—. 2023b, Impedance Control PCB Manufacturing - JLCPCB. https://jlcpcb.com/es/impedance

Kester, W. 2009, Analog Devices, Tutorial MT-001. https://www.analog.com/mt-001

Lanman, A. E., Andrew, S., Lazda, M., et al. 2024, The Astronomical Journal, 168, 87, doi: 10.3847/1538-3881/ad5838

Lorimer, D. R., Bailes, M., McLaughlin, M. A., Narkevic, D. J., & Crawford, F. 2007, Science, 318, 777, doi: 10.1126/science.1147532

Lorimer, D. R., & Kramer, M. 2005, Handbook of Pulsar Astronomy (Cambridge: Cambridge University Press)

Manufacturing, M. 2023, Murata - Innovator in Electronics. https://www.murata.com/en-us/

Microwave, M. 2023, LC Filter Design Tool. https://markimicrowave.com/technical-resources/tools/lc-filter-design-tool/

Mini-Circuits. 2023a, RF/Microwave Equalizers: An Essential Ingredient for the Modern System Designer. https://blog.minicircuits.com/rf-microwave-equalizers-an-essential-ingredient-for-the-modern-system-designer/

—. 2023b, Understanding Power Splitters. https://blog.minicircuits.com/understanding-power-splitters/

—. 2023c, About Mini-Circuits - Overview. https://www.minicircuits.com/WebStore/about/overview.html

—. 2023d, BFTC-415+ Datasheet. https://www.minicircuits.com/pdfs/BFTC-415+.pdf

—. 2023e, ADE-35MH+ Datasheet. https://www.minicircuits.com/pdfs/ADE-35MH+.pdf

—. 2023f, LFCN-630+ Datasheet. https://www.minicircuits.com/pdfs/LFCN-630+.pdf

—. 2023g, LFCN-900+ Datasheet. https://www.minicircuits.com/pdfs/LFCN-900+.pdf

—. 2023h, LFCG-1000+ Datasheet. https://www.minicircuits.com/pdfs/LFCG-1000+.pdf

—. 2023i, HFCN-1200+ Datasheet. https://www.minicircuits.com/pdfs/HFCN-1200+.pdf

—. 2023j, HFCG-1760+ Datasheet. https://www.minicircuits.com/pdfs/HFCG-1760+.pdf

—. 2023k, HFCG-2000+ Datasheet. https://www.minicircuits.com/pdfs/HFCG-2000+.pdf

—. 2023l, NCS2-771+ Datasheet. https://www.minicircuits.com/pdfs/NCS2-771+.pdf

—. 2023m, SC4PS-33+ Datasheet. https://www.minicircuits.com/pdfs/SC4PS-33+.pdf

—. 2023n, SYPS-2-252+ Datasheet. https://www.minicircuits.com/pdfs/SYPS-2-252+.pdf

Narasimhamurthy, A. B., & Sourour, M. R. 2010, OFDM Systems for Wireless Communications, Synthesis Lectures on Communications (San Rafael, CA: Morgan & Claypool Publishers), doi: 10.2200/S00231ED1V01Y200910COM007

Petroff, E., Hessels, J. W. T., & Lorimer, D. R. 2019, A&A Rev., 27, 4, doi: 10.1007/s00159-019-0116-6

—. 2022, A&A Rev., 30, 2, doi: 10.1007/s00159-022-00139-w

Pleunis, Z., Michilli, D., Bassa, C. G., et al. 2021, ApJ, 911, L3, doi: 10.3847/2041-8213/abec72

Pozar, D. M. 2012, Microwave Engineering, 4th edn. (Hoboken, NJ: John Wiley & Sons)

Real Digital. 2023, RFSoC 4x2 Reference Manual, revision a5 edn. https://www.realdigital.org/downloads/4b98c421901794107cd1e25e208fe002.pdf

Shannon, C. E. 1949, Proceedings of the IRE, 37, 10

Simons, R. N. 2001, Coplanar Waveguide Circuits, Components, and Systems (New York: John Wiley & Sons, Inc.)

Smith, P. H. 1939, Electronics, 12, 29

Systems, C. D. 2023, RF and Microwave Design Tools. https://www.cadence.com/en_US/home/tools/system-analysis/rf-microwave-design.html

Wilson, T., Rohlfs, K., & Hüttemeister, S. 2009, Tools of Radio Astronomy, 5th edn. (Berlin, Heidelberg: Springer), doi: 10.1007/978-3-540-85122-6

ANNEXES

Annex A Balun testing board

The Balun testing board was designed to test the differential FDM board. The balun used was the NCS2-771+ 1:2 balun, which was the same model used in chain 0. This board will not be used on the on field implementation of the FDM.

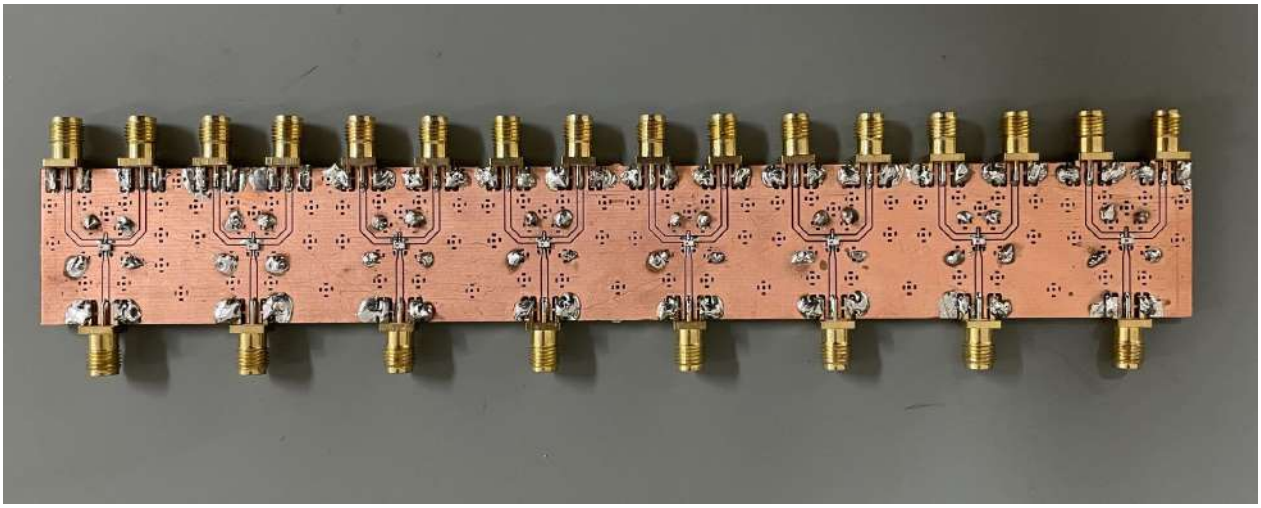

Figure 5.3: Balun testing board used to generate the eight input sinals of the FDM. The board was implemented eight NCS2-771+ 1:2 baluns, which was the same model used in chain 0 to transform the 100 Ω differential signal to 50 Ω.

Annex B Complete FDM simulations

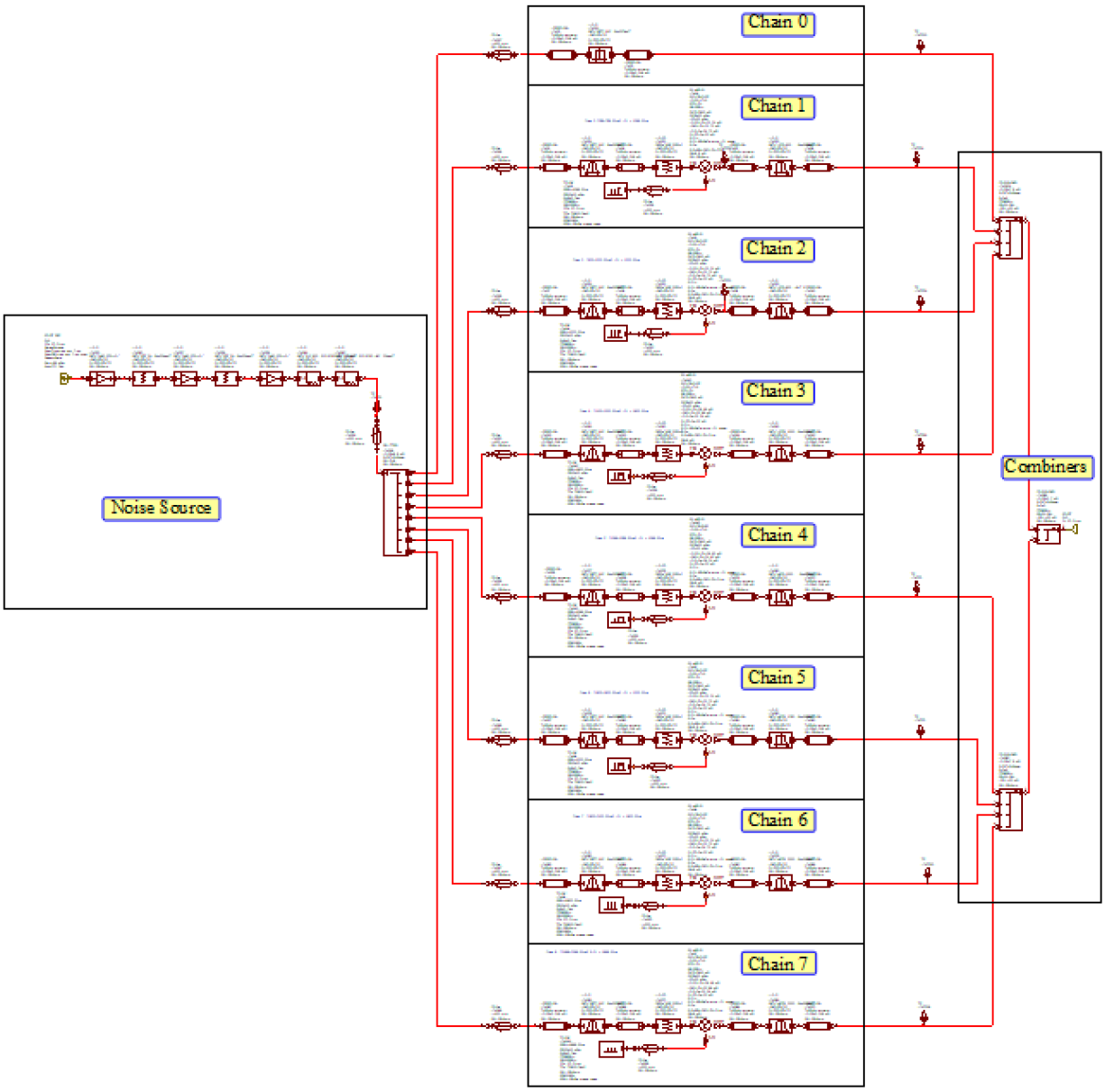

Figure 5.4: Complete simulation of the FDM with commercial components. A noise source was simulated as the FDM input with scattering parameters of the actual components used in the measurements. The simulation considers all chain components and the power combiners, all with the data provided by the manufacturers. Properly simulating the expected behavior of the FDM.

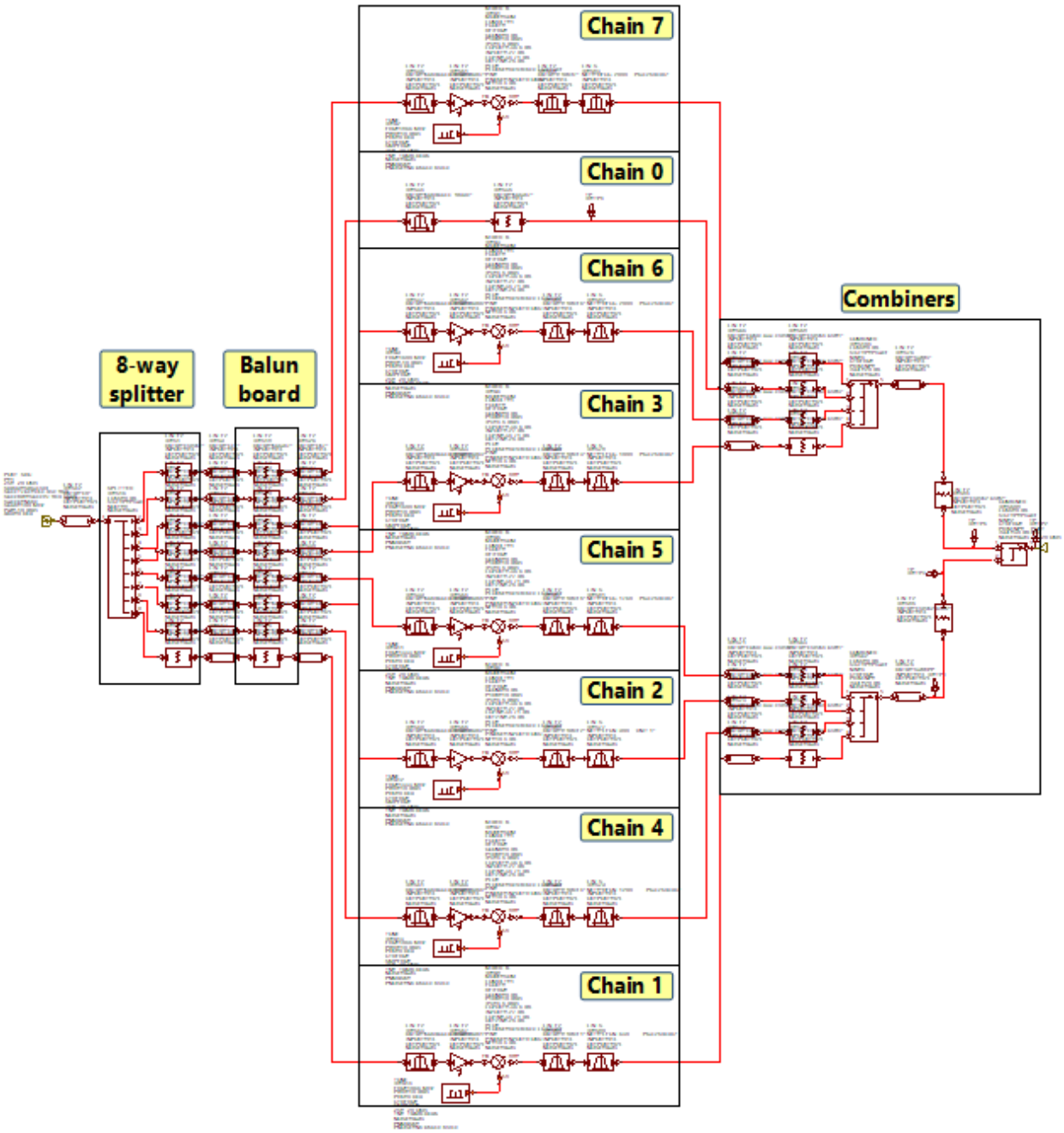

Figure 5.5: Complete simulation of the differential FDM. The input signal was a frequency sweep from 200–600 MHz. The simulation considers all chain components and the power combiners, all the data was obtained from the real testing PCBs measuremetns. An eight way splitter and a balun board were added to the simulations because the real measurements added those components to recreate eight differential input signals.